Ion Implantation and Transmission Microscopy with Nanometer Resolution Using a Deterministic Ion Source

Dissertation

zur Erlangung des akademischen Grades Dr. rer. nat.
des Fachbereichs 08 Physik, Mathematik und Informatik
der Johannes Gutenberg-Universität Mainz

vorgelegt von

Georg Jacob

JOHANNES GUTENBERG
UNIVERSITÄT MAINZ

20. Dezember 2016

Abstract

This work reports on the construction and setup of a single ion source experiment on the basis of a linear Paul trap to the aim of deterministic ion implantation and single ion microscopy. Single $^{40}Ca^{+}$ ions at energies ranging from 0.3 to 6 keV were extracted from the trap at a maximum rate of 3 ions per second. The beam divergence was measured to be 23.7 ± 2.5 µrad, at an energy dispersion of 174 meV, limited by the noise of the extraction voltage. Focussing of the beam with an electrostatic einzel lens to a 1-σ radius of 5.8 ± 1.0 nm was demonstrated, where the minimum two-sample deviation of the beam position in the focal plane has been determined to be 1.5 nm, when integrating over a period of 9 hours.

For the purpose of single ion implantation, molecular nitrogen ions were trapped and sympathetically cooled. Subsequent extraction and implantation of these ions has been carried out and the creation of single nitrogen vacancy color centres in diamond by this method was shown.

For the first time, a single particle microscope was realised, which employs deterministically extracted calcium ions as probe particles for transmission imaging. Even when used in combination with an imperfect detector, this showed a 5 times higher signal-to-noise ratio as compared to microscopy with a conventional particle source, which is subject to Poissonian emission properties. Moreover, it was demonstrated, that the gain in spatial information can be maximised by employing the Bayes experimental design technique, when imaging structures with a parametrisable transmission function. In addition, the precise timing of the extraction event was used to gate the detector and in this way suppress detector dark counts by 6 orders of magnitude.

Furthermore, various future applications of the deterministic single ion source for novel types of microscopy or material doping are discussed.

Kurzfassung

Diese Arbeit behandelt die Konstruktion und den Aufbau einer Einzelionenquelle auf der Grundlage einer linearen Paulfalle, zur deterministischen Implantation und Mikroskopie mit einzelnen Ionen. Es wurden einzelne $^{40}Ca^{+}$ Ionen mit Energien von $0{,}3$ bis 6 keV bei einer maximalen Rate von drei Ionen pro Sekunde aus der Falle extrahiert. Dabei wurde eine Strahldivergenz von $23{,}7 \pm 2.5$ µrad, sowie eine Energiedispersion von 166 meV, begrenzt durch das Rauschen der Extraktionsspannung, gemessen. Der Strahl wurde auf einen 1-σ Radius von $5{,}8$ nm fokussiert, wobei eine minimale Zweiwert-Abweichung der Strahlposition in der Fokusebene von $1{,}5$ nm während einer Messdauer von neun Stunden erzielt werden konnte.

Um molekulare Stickstoffionen zu implantieren wurden diese zunächst gefangen und sympathetisch gekühlt. Mit einer anschließend durchgeführten Extraktion und Implantation dieser Ionen konnten Stickstoff Farbzentren in Diamant erzeugt werden.

Durch Einsetzen dieser Kalzium Ionen als Sonden gelang es zum ersten Mal ein deterministisches Einzelionenmikroskop zu realisieren. Im Vergleich zur Mikroskopie mit einer konventionellen poissonschen Teilchenquelle konnte so, selbst mit einem nicht idealen Detektor, ein fünfmal höheres Signal zu Rausch Verhältnis gemessen werden. Zudem wurde gezeigt, dass durch das Verwenden des *Bayes experimental design* Verfahrens der Informationsgewinn pro Teilchen beim Abbilden von Strukturen mit einer parametrisierbaren Transmissionsfunktion, maximiert werden kann. Zusätzlich wurde der genaue Zeitpunkt des Extraktionsereignisses dazu genutzt die Auslese des Detektors nur in einem bestimmten Zeitfenster zu aktivieren und so die Dunkelzählrate um sechs Größenordnungen zu unterdrücken.

Im Hinblick auf zukünftige Anwendungen werden verschiedene Verbesseungen der deterministischen Einzelionenquelle für den Einsatz in der Mikroskopie und zur Festkörperdotierung diskutiert.

Contents

List of Figures

1. Introduction

Trapping and laser-cooling of atoms enabled substantial advance in fields as diverse as fundamental research [Ket02, Har13, Win13], metrology [Ros08, Lud15] and quantum information processing [Bla08]. The accuracy achieved by these advances, when manipulating the internal and external degrees of freedom, enables an almost total control of the quantum state of the atom. More recently, methods pioneered in this area are increasingly applied to realise ultracold charged particle sources, which show great promise as new tools for numerous applications in microscopy, nanofabrication and metrology.[1]

However, the major motivation for the advancement of these particle sources has been the demand for better sources for microscopy and hence their development is closely related to this issue. Therefore, a brief historical outline of the technical evolution of microscopy is given, before addressing the different, more recent approaches in creating cold beams. This also provides the context for the Paul trap based single ion source used for the experiments of this work and which is introduced subsequently.

1.1. A brief history of microscopy

Invented in the 17th century [VH10], the first microscopes were optical microscopes using light to create a magnified image of an object. These devices quickly found applications in various fields such as biology and medicine. Despite their importance, it took until the end of the 19th century, before Ernst Abbe managed to build an objective which was capable of reaching the physical limit of imaging [Abb73], commonly known as the diffraction limit or the Abbe limit. For typical microscopes this resolution limit is roughly $d \approx \lambda/2$ which is of the order of $0.2\,\mu$m for visible light. Although super-resolution microscopy can apparently surpass this limitation [Hel15], these methods do not break this barrier, but rather they circumvent it by using saturation effects, near field, statistics or deconvolution.

The diffraction limit, indeed, can be much lower when using massive particles which have a substantially shorter wavelength, as is the case with electron microscopes [Kno32, Mül36] or ion microscopes [Mül51, Mül56, Esc75, Orl75], where this difference can account for up to 5 orders of magnitude. The wavelength is given by the de Broglie wavelength $\lambda = h/p$, where h is the Planck constant and p is the momentum. Thus for a given velocity, the heavier the particle, the shorter the wavelength.

Practically, however, even for electrons and small velocities the diffraction is typically

[1] This work exclusively focuses on microscopy and implantation of single ions. Results obtained in other projects, where I also contributed and participated in during this time, therefore is not part of this thesis. This comprises work related to ion crystals and their phase transitions, as well as the proposal for a single atom heat engine (see also Appendix C).

not the limiting factor in terms of spatial resolution. Up to the present, microscopes using massive particles are constrained by imaging errors and the properties of the source. Currently the resolution limit for transmission electron microscopy is in the order of $50\,\mathrm{pm}$, where the limitation is given by imaging errors and a finite source size [Ern09]. For the scanning helium ion microscope [War06] the resolution record is $0.2\,\mathrm{nm}$, which is restricted by mechanical stability and electrical stability of the power supplies [Joy11].

Nowadays electron and ion microscopes have found widespread applications across various scientific [Kru00] and industrial fields [Bas14]. Apart from high resolution imaging, there are growing applications in nanofabrication and metrology [Bas14], which often imply specific requirements or modifications regarding the optics or sources. In the case of nanofabrication, mostly focussed ion beams are employed, where the particles can either be used for ablation or the deposition of material.

1.2. Novel sources for cold beams

Over the last decade, methods from the fields of cold atoms, atom optics and photonics have been inceasingly applied to improve sources in different respects. There have been several successful attempts of ionising and subsequently extracting atoms from laser cooled gases. Pulsed extraction of rubidium [Cla07, Rei09], as well as continuous extraction with subsequent focussing of chromium ions [Han08, Ste10] and lithium ions [Knu11] from a magneto-optical trap has been demonstrated (see Figure 1.1). These approaches are aiming to create high brightness and low velocity beams of cold ions. In the case of lithium, the beam was applied for high resolution, high contrast backscattered ion microscopy [Twe14, McC16]. Because this method allows for relatively low ion energies ($500\,\mathrm{eV}$ to $5\,\mathrm{keV}$), it provides favourable yield and a small interaction volume, when compared to conventional helium or gallium ion microscopes.

The mentioned process of ionisation from cold gases inevitably creates electrons. This enables one to implement a source of cold electrons, which offers low emittance [Tab10], or high coherence electron bunches for ultrafast diffraction imaging [McC11, Eng13].

Yet another way to create ultrafast pulsed electron sources is the photoemission induced by laser pulses [Wil97, Ihe01], where the current can be as low as one electron per pulse [Lob05]. Using a sharp metallic tip as a cathode drastically reduces the emission area and thus the pulse duration to a few femtoseconds [Hom06, Rop07]. A similar approach utilises laser induced plasmonic excitation to emit electrons from a metallic tip, enabling a close source to sample distance [Mül16].

Also the creation of cold ionic caesium sources by transversal cooling and ionisation of a continuous atomic beam has been realised experimentally [Knu13, Vit16]. Applications of this could be secondary ion mass spectroscopy or the nanofabrication via ion beam milling in the sub nanometer regime at currents of higher than $1\,\mathrm{pA}$, both of which take advantage of a higher mass compared to helium sources and an expected higher spatial resolution of down to $1\,\mathrm{nm}$ compared to gallium focussed ion beams, which are currently at about $5\,\mathrm{nm}$ [McC16].

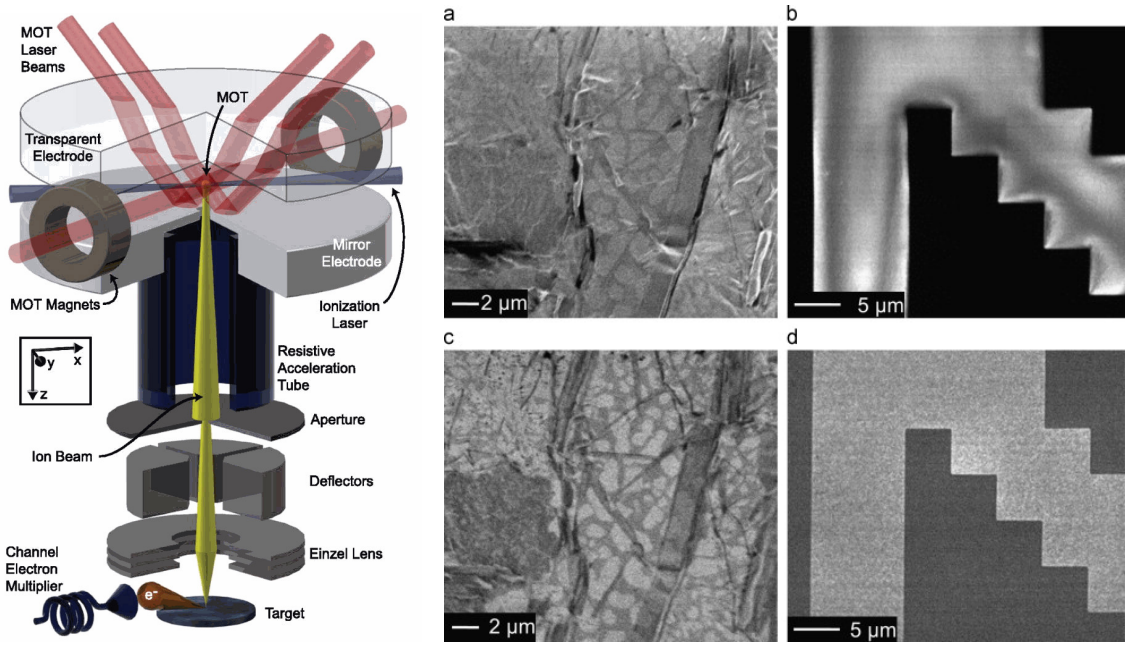

Figure 1.1.: Left hand side: implementation of a lithium ion source based on a magneto-optical trap (MOT). Ions are extracted from the MOT into a conventional FIB column, which is equipped with deflection electrodes, stigmation, and an objective lens (einzel lens). The ions impact the sample where secondary electrons and backscattered ions are created which subsequently are detected with a channel electron multiplier. Image taken from [McC16]. Right hand side: lithium ion microscope images, comparing secondary electron and backscattered ion contrast. The secondary electron image of a lead-tin solder dot (a) is dominated by topographic contrast, while the backscattered ion image contrast (c) is caused by difference in atomic number. The charged oxide appears dark in the secondary electron image of a metal on oxide test pattern (b), while charging causes distortions along the metal-oxide interface. The backscattered ion image (d) has no adverse effects from the charging [Twe14].

Notably, there are also several cold ion source experiments which are taking efforts to improve the energy spread and the phase space distribution in a rubidium ion beam by time-dependent extraction fields [Rei10] or spatially modulated ionisation lasers [Mur14]. Furthermore, it has been shown theoretically, that Rydberg interactions may suppress stochastic Coulomb effects, resulting in an enhancement of the brightness of the ion beam [Mur15].

1.3. Deterministic sources

The unique extent of control over the degrees of freedom of cold atoms opens up the possibility to realise single ion sources, offering deterministic emission properties. To this goal, feedback controlled loading of single atoms in a magneto optical trap [Hil03b, Hil03a] or alternatively in an optical trap [Hen10] with subsequent photoionisation and

extraction has been demonstrated. There are also proposals to employ the Rydberg blockade mechanism to achieve the quasideterministic extraction of single ions or electrons from a laser cooled atom cloud, by photo ionising a single atom from a dipole-blockade configuration [Ate13, Tre16] (see Figure 1.2).

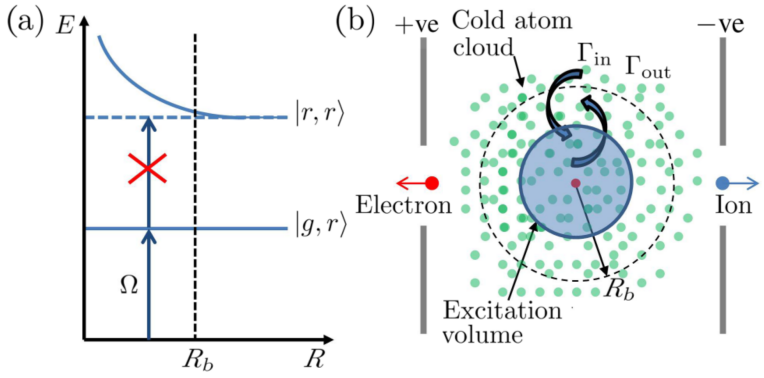

Figure 1.2.: Proposal for a derterministic single ion source based on the Rydberg blockade mechanism. **a)** The principle of the blockade mechanism. The energy level is shifted as a function of the distance from a Rydberg atom. **b)** Schematic of the single ion source based on that principle. Only one ion is created whithin the blockade radius. The image is taken from [Ate13].

The major motivation for the realisation of such single ion sources is the deterministic doping of solid state devices with high lateral resolution. The placement of single atoms with high precision has numerous applications in semiconductor doping [Koe11], as for example the enhancement of semiconductor device performance [Shi05], single-atom transistors [Fue12], or the creation of single-spin devices for quantum information processing [Kan98, Per04b, Don10, Pla12, Vel15]. Other applications are the generation of systems of coupled nitrogen vacancy (NV) colour centres in diamond [Dol13], as well as cerium or praseodymium in yttrium orthosilicate [Kol12]. In case of the semiconductor doping and for the devices based on the coupling of functional impurities by spin-spin interaction the implantation with single atoms must have a lateral precision in the order of 10 nm or better. For the former, this length scale results from the size of the components of the integrated circuits, and for the latter it is a consequence of the desired coupling strength which should be in the order of several 10 kHz [Neu10].

1.4. The Paul trap ion source

In this thesis a deterministic single ion source has been implemented by extracting laser-cooled $^{40}Ca^{+}$ ions from a linear segmented Paul trap [Mei06, Sch09a] (see Fig. 1.3). Aside from being deterministic, the most prominent feature of this approach arises from the ability to cool trapped ions to the motional ground state. According to Liouville's theorem the phase space volume for an ensemble of particles in a conservative potential is preserved [Kuy16]. This means that the source defines the phase space volume occupied

by the particles, which in the case of ground state cooled ions in a Paul trap reaches its ultimate limit, given by the Heisenberg uncertainty principle. This, in principle, permits the extraction of ions with the lowest possible emittance and smallest possible energy dispersion, both of which are favourable for a high resolution focus.

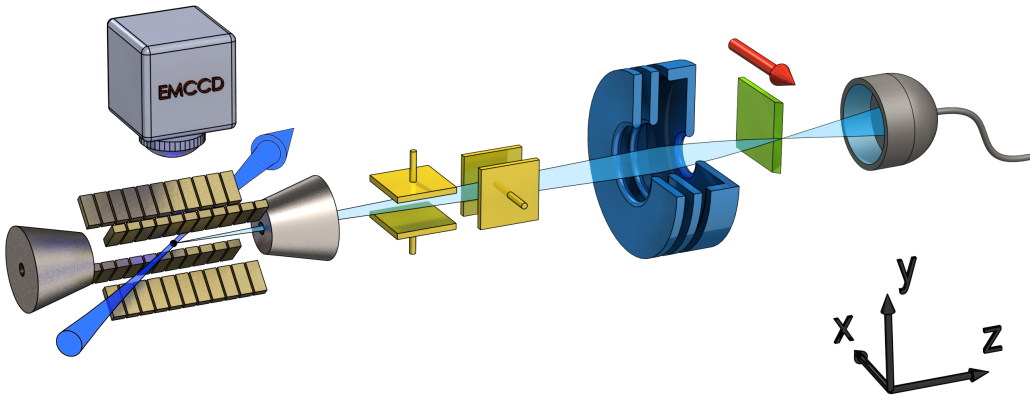

Figure 1.3.: Sketch of the deterministic single ion source experiment. The ion trap consists of segmented electrodes and endcaps (gray). Laser-cooling (blue arrow) and imaging CCD system (from top) are depicted. After cooling, ions are extracted via the endcaps. Deflection electrodes (yellow) and a einzel lens (blue) are placed along the ion extraction pathway (light-blue). In the focal plane a profiling edge or alternatively a transmissive mask or a substrate for implantation (green) is placed on a three-axis nano-translation stage (not shown). Single ion counting is performed with a secondary electron multiplier device down stream.

Another befeficial feature is the possibility to trap and sympathetically cool other elements by the mutual Coulomb interaction with laser cooled ions [Lar86, Kie00]. This allows for realising a universal ion source, highly desirable for the doping of solid state devices. In contrast to methods relying on impact detection [Per04a, Mit05, Hop08], this deterministic ion implantation technique is also appropriable for energies well below 10 keV, and therefore low enough to restrain the straggling of the dopants when impacting [Jam16] to an amount smaller than the required spatial resolution. As a proof of principle of this method, molecular nitrogen ions were trapped, sympathetically cooled, extracted and subsequently implanted into diamond where single NVs have been created.

An additional application is microscopy based on deterministic probing. This offers several advantages over microscopy with conventional particle sources which are subject to Poissonian emission properties. In case the of the latter, the signal-to-noise ratio (SNR) can typically be improved by increasing the exposure, which is a direct consequence of the Poissonian statistics of these sources. However, a high particle flux can be adverse in applications where high irradiation can cause charging [Kim10], contamination or even damage [Pra95] to the sample. On the other hand, probing with a deterministic source requires an exposure of only a single particle to probe for transmission, and thus in principle, could give rise to noiseless imaging. However, the detector still exhibits finite

quantum efficiency, rendering the statistics of the detection signal binomial. Eventually, this still leads to a higher SNR and thus to a inherently higher information gain per particle than would be possible with Poissonian emission properties. Moreover, the latter can be increased even further by employing the Bayes experimental design method, which permits to maximise the information gain for each individual particle probe and thus measuring the dimensions of nanometer sized structures with higher precision while at the same time using fewer probe particles, compared to pixel wise imaging with subsequent fitting. In addition the precise timing of the extraction event allows for gating the detection by the extraction event and in this way suppressing detector dark counts.

The thesis is structured as follows: In chapter 2 the theoretical description of trapping ions in time dependent electric fields is given, which also serves as an introduction to the field of ion trapping. Moreover, it contains the basic theory of light-ion interaction, necessary to understand laser cooling. Thereby, the formulas which are later used to assess the quality of the laser cooling by measuring the ion temperature are derived. Regarding the ion source implementation, the emittance and the brightness are introduced, which are both measures for assessing and comparing particle sources. In addition, a theoretical model of an electrostatic einzel lens, together with a number of specific analytical methods for the evaluation of different experiments is presented in this chapter. A detailed description of the experimental setup, which was designed and developed specifically for the purpose of performing deterministic ion implantation is given in chapter 3. In order to evaluate the performance of the different components of the system, in particular the ion source and the einzel lens, several characterisation measurements were carried out and are discussed in chapter 4. The main results of this thesis are presented in chapter 5 and 6. Chapter 5 contains a proof of principle microscopy with deterministically extracted single ions, where an increase of the SNR by a factor of 5, and a reduction of the detector dark counts by 6 orders of magnitude was shown. In addition, by using the Bayes experimental design method, the size and the position of a circular hole structure was determined. Chapter 6 includes the demonstration of creating NV colour centres in diamond by implantation of single molecular nitrogen ions. In addition to a conclusion, the last chapter 7 is concerned with plans for future improvements and novel applications of the single ion source.

2. Theoretical foundations and methods

In this chapter, first, the experimental building blocks of the single ion-trap source, namely the 2.1 *Paul trap* and 2.2 *Light-ion interaction* are described analytically. This allows for deriving formulas to evaluate experiments related to both parts and also serves as a short introduction to the field of ion trapping. The following section, 2.3 *Ion source*, introduces the emittance and the brightness which are useful measures to describe a particle beam. Section 2.4 *Ion optics* contains an analytical model of an einzel lens, which in this work is used to focus the ions upon extraction from the trap. The formulas derived here are later applied to discuss measurement results regarding the focussing properties of the system consisting of the ion source and the einzel lens. Moreover, this section includes a brief introduction to the numerical methods, which are employed to model the trapping, the extraction and the focussing of ions as well as the subsequent optimisation of related parameters. Section 2.5 *Methods of measurement* introduces a number mathematical methods which are used to analyse beam properties and microscopy in the experimental part of this work.

2.1. Paul trap

The Paul trap or quadrupole ion trap was developed by Wolfang Paul [Pau53, Pau58], for which he received the Nobel price in 1989. It allows one to store charged particles such as ions within dynamic electric fields.

2.1.1. Ion confinement

As a consequence of the Laplace equation, it is not possible to confine a charged particle in all three spatial directions with static electric fields. However, an alternating electric field can be employed to achieve a *dynamical confinement*. This is realised by interchanging the confining and anti-confining directions sufficiently fast, such that the particles inertia prevents it from escaping the trap. On average this generates an effective trapping potential, which according to the Floquet solution results in a harmonic *pseudo potential*. The simplest field geometry which provides such a confinement is an alternating quadrupole field. It can create a confinement in two or three[2] dimensions. A configuration where the quadrupole is trapping the particle in only two dimensions, and where the confinement in the third direction is achieved by a static field, is called a *linear* trap. The simplest electrode

[2] An oscillating circular symmetric quadrupole field provides a confinement in all three dimensions. Typically such a trapping field is realised by applying an oscillatory voltage between a ring and two endcaps terminating the open space within the ring on both sides symmetrically.

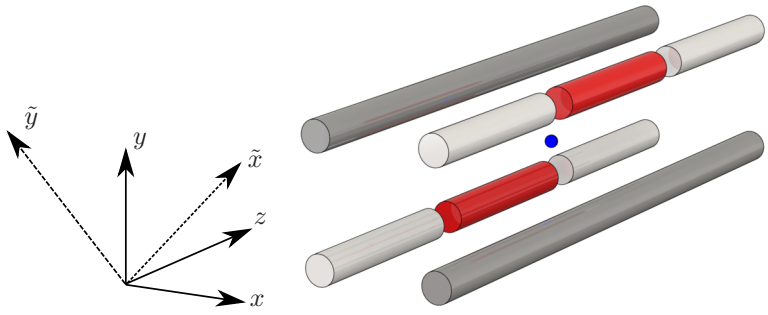

Figure 2.1.: Sketch of a linear segmented Paul trap. The gray rods are RF electrodes, creating a confining pseudo potential in the radial direction ($\tilde{x}$,$\tilde{y}$). The DC electrodes are segmented, where the red segments are on a lower potential than the white ones to generate a trapping potential for the ion (blue) in the axial direction (z).

arrangement for realising this type is to use four parallel electrodes, where an alternating voltage is applied to diagonally opposing electrodes (compare Fig. 2.1). This creates a confining quadrupole field in the plane perpendicular to the electrodes which is referred to as radial direction in the following. The static confining potential perpendicular to this plane is either provided by endcaps or a segmentation of the electrodes, where in both cases a static voltage is applied. The respective direction is referred to as axial.

The potential of a Paul trap in harmonic approximation featuring a static and an oscillating part in its most general form can be written as:

$$\Phi(\mathbf{x},t) = \frac{1}{2}\,U_{\mathrm{dc}} \sum_i \alpha_{\mathrm{dc},i}\, x_i^2 + \frac{1}{2}\,U_{\mathrm{rf}} \cos(\omega_{\mathrm{rf}}\, t) \sum_i \alpha_{\mathrm{rf},i}\, x_i^2, \qquad \text{with} \quad i \in \{\tilde{x},\tilde{y},z\}. \tag{2.1}$$

Here, U_{dc} is the voltage amplitude of the static part, U_{rf} the voltage amplitude of the oscillating part and the coefficients α are describing the potential curvature. With the potential (2.1) being linearly independent in all directions, the equation of motion reads

$$\ddot{x}_i(t) = -\frac{Z\,|q|}{m}\frac{\partial\Phi(\mathbf{x},t)}{\partial x_i} = -\frac{Z\,|q|}{m}\left[U_{\mathrm{dc}}\alpha_{\mathrm{dc},i} + U_{\mathrm{rf}}\alpha_{\mathrm{rf},i}\cos(\omega_{\mathrm{rf}}t)\right] x_i(t). \tag{2.2}$$

Introducing the substitutions

$$\xi = \frac{\omega_{\mathrm{rf}}t}{2}, \quad a_i = \frac{8QU_{\mathrm{dc}}\alpha_{\mathrm{dc},i}}{m\omega_{\mathrm{rf}}^2}, \quad q_i = \frac{4QU_{\mathrm{rf}}\alpha_{\mathrm{rf},i}}{m\omega_{\mathrm{rf}}^2}, \tag{2.3}$$

equation (2.2) can be expressed in the canonical form of the Mathieu differential equation [Pau90]:

$$\frac{\mathrm{d}^2 x_i}{\mathrm{d}\xi^2} + \left[a_i - 2q_i\cos(2\xi)\right] x_i = 0. \tag{2.4}$$

According to the Floquet theorem, stable solutions take the form [Lei03]:

$$x_i(\xi) = Ae^{\mathrm{i}\beta_i\xi} \sum_{N\in\mathbb{Z}} C_{2n} e^{\mathrm{i}2n\xi} + Be^{-\mathrm{i}\beta_i\xi} \sum_{N\in\mathbb{Z}} C_{2n} e^{-\mathrm{i}2n\xi}. \tag{2.5}$$

It can be shown that the coefficients C_{2n} satisfy a recursion relation involving β_i, a_i and q_i by substituting equation (2.5) into equation (2.4). In the case $(|a_i|, q_i) \ll 1$ and with the initial condition $A = B$, this recursion relation can be used to calculate the lowest-order approximation of equation (2.5) by truncating the recursion after C_{2n}:

$$x_i(t) \approx 2AC_0 \cos\left(\beta_i \frac{\omega_{\text{rf}}}{2} t\right) \left[1 - \frac{q_i}{2} \cos(\omega_{\text{rf}} t)\right], \quad \text{with} \quad \beta_i \approx \sqrt{a_i + \frac{q_i^2}{2}}. \tag{2.6}$$

Since the potential has to obey the Laplace equation at any time, the coefficients α have to meet the following conditions:

$$\sum_i \alpha_{\text{dc},i} = 0, \qquad \sum_i \alpha_{\text{rf},i} = 0. \tag{2.7}$$

In the case of the linear trap, which has a static confinement in z-direction and a dynamic confinement in $\tilde{x}$-$\tilde{y}$-direction, they read

$$-\left(\alpha_{\text{dc},\tilde{x}} + \alpha_{\text{dc},\tilde{y}}\right) = \alpha_{\text{dc},z} > 0, \quad \alpha_{\text{rf},z} = 0, \quad \text{and} \quad \alpha_{\text{rf},\tilde{x}} = -\alpha_{\text{rf},\tilde{y}}. \tag{2.8}$$

According to (2.6), the trajectory of the trapped particle in the radial direction consists of a superposition of two harmonic oscillations: the *secular motion* with the frequency

$$\omega_i = \beta_i \frac{\omega_{\text{rf}}}{2} = \sqrt{\frac{2QU_{\text{dc}}\alpha_{\text{dc},i}}{m} + \frac{2Q^2U_{\text{rf}}^2\alpha_{\text{rf},i}^2}{m^2\omega_{\text{rf}}^2}}, \tag{2.9}$$

which corresponds to the oscillation in the pseudo potential

$$\Psi = \frac{1}{2} \sum_i m\omega_i^2 r_i^2, \tag{2.10}$$

and a fast off-resonant forced oscillation with frequency ω_{rf}, caused by the oscillating field of the radio frequency (RF) trap drive, also referred to as *micromotion* [Pau90]. The amplitude of this micromotion is proportional to the displacement from the node of the RF potential, which results from the secular motion. For the description of the light-ion interaction in section 2.2 only the secular part of the potential is considered.

In a real experiment however, an additional displacement from the centre of the quadrupole field can be induced by stray fields or imperfect geometry of the trap, increasing the micromotion. These effects can be largely compensated for by applying static voltages to dedicated electrodes (see also section 4.1.2).

2.2. Light-ion interaction

Interaction of the ion with light fields is the most important experimental tool for conducting experiments with trapped ions. In this work, light-ion interaction is involved in photoionisation, Doppler cooling, fluorescence detection, and sideband spectroscopy which comprises sideband cooling and thermometry.

In regard to the realisation of the single ion trap source, the cooling techniques are particularly crucial for the performance of the device. This is because the most important source property, the emittance, which is a measure for the phase space occupation of the source, is defined by the energy of the ion in the trap. In order to minimise this energy when preparing the wavepacket of the ion for extraction, therefore, laser cooling is decisive - ideally close to the motional grounstate.

Although sideband spectroscopy and cooling of a two-ion crystal is a promising perspective for further experiments in the context of an ion source based on a Paul trap, such experiments are not within the scope of this work. Therefore, the following theoretical description of light-ion interaction is limited to the single ion case.

2.2.1. Theory model and resolved motional sidebands

An analytical model of the light-ion interaction - necessary for describing the resolved sideband cooling and thermometry - requires the quantum mechanical description of an ion in a harmonic potential, taking into account the coupling of the internal electronic degrees of freedom with the external motional states. This coupling is mediated by the interaction with a single mode laser field. For the internal electronic states it is sufficient to consider a two-level system, as the coupling fields are assumed to be close to resonance for these levels and the Rabi frequencies are considered to be much smaller than the detuning with respect to off resonant transitions [Lei03]. In order to transfer the Hamiltonian into the Dirac picture it is split into an interaction free part $\hat{H}_0$ and a part containing the interaction $\hat{H}_{\text{int}}$ [Roo00, Lei03]:

$$\hat{H} = \hat{H}_0 + \hat{H}_{\text{int}}. \tag{2.11}$$

$\hat{H}_0$ consists of two parts:

$$\hat{H}_0 = \frac{\hbar}{2}\nu\hat{\sigma}_z + \hbar\omega\left(\hat{a}^\dagger\hat{a} + \frac{1}{2}\right). \tag{2.12}$$

The first term is the energy of the two internal states separated by $\hbar\nu$, where $\hat{\sigma}_z = |e\rangle\langle e| - |g\rangle\langle g|$ is the Pauli operator, determining the difference in population density between the excited state $|e\rangle$ and the ground state $|g\rangle$. The second term describes the energy of the ion in the external harmonic potential with trap frequency ω. The operator $\hat{a}^\dagger\hat{a}$ measures the number of motional quanta n in the energy eigenstate $|n\rangle$ of the harmonic oscillator, with $\hat{a}^\dagger$ and $\hat{a}$ being the creation and annihilation operators of the motional quanta, respectively. The interaction Hamiltonian describes the interaction between laser field and ion:

$$\hat{H}_{\text{int}} = \frac{\hbar}{2}\Omega_0\left(\hat{\sigma}_+ + \hat{\sigma}_-\right)\left(e^{i(k\hat{q}\cos\theta - \nu_{\text{L}}t + \varphi)} + e^{-i(k\hat{q}\cos\theta - \nu_{\text{L}}t + \varphi)}\right), \tag{2.13}$$

where $\hat{\sigma}_+ = |e\rangle\langle g|$ and $\hat{\sigma}_- = |g\rangle\langle e|$ are the raising and lowering operators of the atomic transition, k is the wave number, ν_{L} is the frequency of the laser and θ is the angle between oscillation and k-vector of the light. Introducing the *Lamb-Dicke parameter* $\eta = k\cos(\theta)\sqrt{\hbar/(2m\omega)}$, which relates the wave packet size of the lowest harmonic oscillator state to the wavelength of the atomic transition, the position operator can be written as $\hat{q} = \eta/k \cdot (\hat{a} + \hat{a}^\dagger)$. Without loss of generality, we assume $\theta = 0$ for the further calculations.

Transferred to the interaction picture and applying the rotating wave approximation[3], this Hamiltonian reads

$$\begin{aligned}\hat{H}_{\text{int}}^{I} &= e^{\frac{i}{\hbar}\hat{H}_0 t}\hat{H}_{\text{int}}e^{-\frac{i}{\hbar}\hat{H}_0 t} \\ &= \frac{\hbar}{2}\Omega_0\left(\hat{\sigma}_+ e^{i\left(\eta\left(\hat{a}^\dagger e^{-i\omega t}+\hat{a}e^{i\omega t}\right)-\Delta t+\varphi\right)} + \hat{\sigma}_- e^{-i\left(\eta\left(\hat{a}^\dagger e^{-i\omega t}+\hat{a}e^{i\omega t}\right)-\Delta t+\varphi\right)}\right),\end{aligned} \tag{2.14}$$

where $\Delta = \nu - \nu_{\text{L}}$ is the detuning of the laser from the atomic resonance. Also the relations $e^{i\omega\hat{a}^\dagger\hat{a}t}\hat{a}e^{-i\omega\hat{a}^\dagger\hat{a}t} = \hat{a}e^{-i\omega t}$ and $e^{i\frac{1}{2}\nu\hat{\sigma}_z t}\hat{\sigma}_+ e^{-i\frac{1}{2}\nu\hat{\sigma}_z t} = \hat{\sigma}_+ e^{i\nu t}$ were used. This Hamiltonian describes the coupling of the states $|g,n\rangle$ and $|e,n\pm l\rangle$ via the laser field. In the rest frame of the ion, the light field of the laser appears to be modulated with the trap frequency ω. As a result, sidebands separated from the resonance of the transition (carrier) by multiples of ω are created in the excitation spectrum. Thus, the motional state of the ion can be changed by tuning the laser frequency to the sidebands. The dynamics of this system can be better illustrated by expanding the exponential function in terms of η, this yields

$$\hat{H}_{\text{int}}^{I} \approx \frac{\hbar}{2}\Omega_0\hat{\sigma}_+ e^{-i\Delta t+\varphi}\left(1 + i\eta\left(\hat{a}^\dagger e^{-i\omega t} + \hat{a}e^{i\omega t}\right) + \mathcal{O}(\eta^2)\right) + \text{H.c.}. \tag{2.15}$$

Three important cases can be distinguished, with respect to the laser frequency:

- In the case where the laser is tuned to resonance ($\Delta = 0$), the Hamiltonian is reduced to

$$\hat{H}_{\text{int}}^{I} \approx \frac{\hbar}{2}\Omega_0\left(1 - \frac{\eta^2}{2}\left(2\hat{a}^\dagger\hat{a}+1\right)\right)\left(\hat{\sigma}_+ e^{i\varphi} + \hat{\sigma}_- e^{-i\varphi}\right) = \hat{H}_{\text{res}}^{I}, \tag{2.16}$$

  which in first order solely couples the states $|g,n\rangle$ and $|e,n\rangle$, *i.e.* driving Rabi oscillations on the carrier transition.

- If the laser is tuned to the red sideband ($\Delta = -\omega$), the Hamiltonian is dominated by terms including $\hat{a}\hat{\sigma}_+$ and $\hat{a}^\dagger\hat{\sigma}_-$:

$$\hat{H}_{\text{int}}^{I} \approx \frac{\hbar}{2}\Omega_0\eta\left(\hat{a}\hat{\sigma}_+ e^{i\phi} + \hat{a}^\dagger\hat{\sigma}_- e^{-i\phi}\right) = \hat{H}_{\text{rsb}}^{I}. \tag{2.17}$$

  This Hamiltonian is called the *Jaynes-Cummings* operator. It couples the states $|g,n\rangle$ and $|e,n-1\rangle$. This means, the internal transition is excited and one motional quanta is removed at the same time.

- If the laser is tuned to the blue sideband ($\Delta = \omega$), the original Hamiltonian is dominated by terms including $\hat{a}^\dagger\hat{\sigma}_+$ and $\hat{a}\hat{\sigma}_-$. It therefore reads

$$\hat{H}_{\text{int}}^{I} \approx \frac{\hbar}{2}\Omega_0\eta\left(\hat{a}^\dagger\hat{\sigma}_+ e^{i\phi} + \hat{a}\hat{\sigma}_- e^{-i\phi}\right) = \hat{H}_{\text{bsb}}^{I}. \tag{2.18}$$

  It couples the states $|g,n\rangle$ and $|e,n+1\rangle$, implying,s the internal transition is excited and one motional quanta is added simultaneously.

Figure 2.2 contains an illustration of these three cases.

[3] Fast oscillating parts of the Hamiltonian, describing non energy conserving virtual transitions, which in the Schrödinger equation lead to terms such as $1/\nu$, $1/\omega$ and similar, are neglected in this approximation.

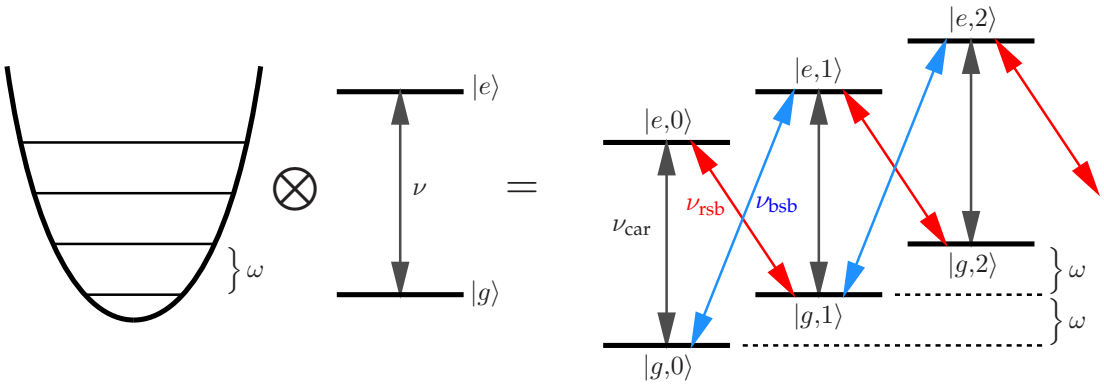

Figure 2.2.: Schematic diagram of the product Hilbert space of a harmonic oscillator with frequency spacing of ω and a two-level system. The right hand side illustrates how the different transitions can be addressed by choosing the laser frequency accordingly. The red sideband corresponds to $\nu_{\mathrm{L}} = \nu_{\mathrm{rsb}}$, the blue sideband to $\nu_{\mathrm{L}} = \nu_{\mathrm{bsb}}$ and the carrier transition to $\nu_{\mathrm{L}} = \nu = \nu_{\mathrm{car}}$. Note that the level $|g,0\rangle$ does not couple to the red sideband, and $|e,0\rangle$ does not couple to the blue sideband.

In addition, the carrier Rabi frequency Ω_0 is modified by the transition matrix elements $M_{n,n+l}$, when driving the different transitions between $|g,n\rangle$ and $|e,n \pm l\rangle$:

$$\Omega_{n,n+l} = M_{n,n+l}\,\Omega_0. \tag{2.19}$$

The elements are thereby given by

$$M_{n,n+l} = \langle n+l|\, e^{ik\hat{q}}\, |n\rangle = e^{-\eta^2/2}\eta^{|l|}\mathcal{L}_q^{|l|}(\eta^2)\left(\frac{q!}{(q+|l|)!}\right)^{1/2}, \tag{2.20}$$

where $q = \min\{n, n+l\}$ and $\mathcal{L}_q^{|l|}(x)$ are the corresponding Laguerre polynomials.

So far the finite absorption width of the transition was neglected. Taking into account a natural linewidth of Γ, two extreme cases can be considered:

$\omega \gg \Gamma$ **:** In the case where the trap frequency ω is much higher than the decay rate of the transition Γ, the linewidth of the transition is smaller than the spacing of the sidebands, such that they can be resolved and addressed by deliberately tuning the laser to the respective frequency. According to equation 2.15 and the following special cases, this leads to an oscillation of the population between the states coupled by this Hamiltonian. This can be used to prepare an arbitrary superposition of these states by applying a laser pulse with a respective pulse area Ωt, provided that the system was in a defined known state (initialising the real system in such a state will be described in 2.2.4). For example, a pulse of the area $\Omega\, t = \pi$ is called a π-pulse and can be applied to transfer the entire population between two orthogonal states, whereas a pulse with area $\Omega\, t = \pi/2$ is termed a $\pi/2$-pulse and can be used to prepare an equal superposition of two orthogonal states. In the same way, tuning the laser to the red and blue sidebands provides means to additionally manipulate

the motional degree of freedom. In the present work, this regime applies to the $4^2S_{1/2}$ to $3^2D_{5/2}$ quadrupole transition of $^{40}Ca^+$ at 729 nm, which will be applied for sideband cooling and thermometry (see 2.2.6).

$\omega \ll \Gamma$ **:** If the trap frequency ω is much lower than the decay rate of the transition Γ, the linewidth of the transition is larger than the spacing of the sidebands. This means that the ion scatters many photons during one oscillation period and spontaneous emission has to be taken into account. This, however, interrupts the coherent evolution described above and the recoil of the emitted photons is causing momentum kicks.[4] In this regime, a detuned light field can provide a velocity dependent force mediated by the Doppler effect. Using this to create a retarding force is termed Doppler cooling (compare section 2.2.3). With the typical trap frequencies in the order of 1 MHz used in the experiments discussed later, this regime holds for the $4^2S_{1/2}$ to $4^2P_{1/2}$ dipole transition of $^{40}Ca^+$ used for Doppler cooling and fluorescence detection.

2.2.2. The level structure of $^{40}Ca^+$

The atom species, which in this work is used for all experiments involving light-ion interaction is ^{40}Ca. It is the most abundant isotope of calcium and has no nuclear spin. Singly charged $^{40}Ca^+$ features a hydrogen like level structure (see Fig. 2.3). It has two

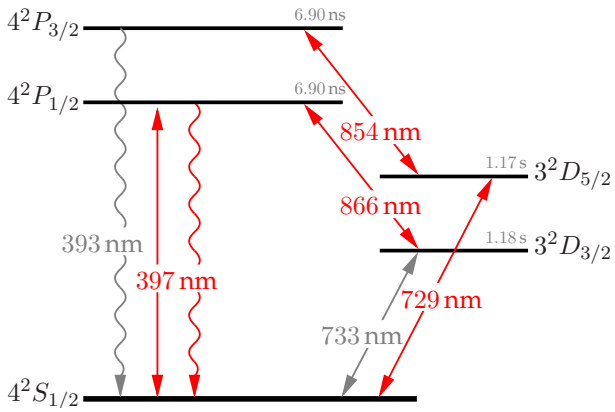

Figure 2.3.: Term diagram of ionised calcium, showing the relevant energy levels without the Zeeman substructure. Important transitions along with the corresponding wavelengths and respective decay times [Kre05, Het15] are depicted as arrows. Transitions which in the experiments are driven by lasers are shown in red.

distinct properties which render calcium favourable for ion trap experiments, and of which this work is making use of in practical terms. Firstly, it features a short lived dipole transition which can be driven in a closed cycle, suitable for Doppler cooling and fluorescence detection. Secondly, $^{40}Ca^+$ has a long lived quadrupole transition, which can be used for resolved sideband spectroscopy.

[4] A detailed modelling of this dynamics requires using the master equation formalism [Ste86, Cir92].

The $4^2P_{1/2}$ excited state has a relatively short lifetime of 6.90 ns [Het15]. It is connected to the $4^2S_{1/2}$ ground state via a dipole transition, which is used for the fluorescence detection, imaging of the ion and Doppler cooling (for a more detailed description see 2.2.3).

The metastable $3^2D_{3/2}$ and $3^2D_{5/2}$ levels are connected to the ground state via quadrupole transitions, featuring lifetimes of 1.17 s and 1.18 s, respectively [Kre05]. Accordingly, the natural linewidths are in the order of 1 Hz, making them ideal for resolved sideband spectroscopy. However, this property can have adverse effects, when driving the dipole transition. With a branching ratio of about 1:10 the $4^2P_{1/2}$ state can decay into the $3^2D_{3/2}$ metastable state. Moreover, in the experiment the $4^1P_{3/2}$ state can be off-resonantly excited by the laser at 397 nm and decay into the $3^2D_{5/2}$ state with a small probability. For this reasons, both metastable states are connected to the P states via 866 nm and 854 nm lasers, when driving the cooling transition.

2.2.3. Doppler cooling

Doppler cooling [Hän75, Win75, Win78, Neu78] is a technique to cool atoms by using laser light in order to generate a velocity dependent force. It is based on the momentum transfer when scattering photons. While an absorption always is accompanied by a momentum kick in the propagation direction of the photons, the momentum transfer as a result of spontaneous emission is isotropically distributed and therefore cancels out to zero when averaging over many scattering events. As a consequence, resonantly scattered photons yield a net force in the propagation direction of the light. This effect can be harnessed for the cooling of atoms by red detuning the light from resonance. Considering the Doppler effect, in this case photons are resonantly scattered only if the atom moves towards the light, and in this way creating a decelerating force. To preserve the orientation between velocity and deceleration, the period of an oscillation in the trap potential has to be long compared to one cooling cycle consisting of absorption and spontaneous emission (compare 2.2.1). This configuration effectively realises a velocity dependent force which is cooling the atom.

As long as the ions are spatially confined by the Paul trap, one laser beam direction is sufficient for cooling, provided that its k-vector has a projection in each direction of the trap axes. The cooling rate, is proportional to the decay rate. This means the lifetime of the cooling transition should be as short as possible. Additionally, a high scattering rate is favourable for fluorescence detection of the ion. The decay rate of the $4^2S_{1/2}$ to $4^2P_{1/2}$ transition of $^{40}Ca^+$ is high enough for both purposes.

In average the momentum transfer due to photon emission is zero, but because of the stochastic nature of the process this leads to a random walk in phase space, counteracting the cooling. The cooling rate shrinks as the ion is getting colder until it equals the heating rate introduced by the spontaneous emission. This equilibrium state is called the Doppler limit. A derivation of this limit based on this semi classical picture, using a simplified two-level system, can be found in [Ste86] and [Lei03]. For calcium ions this limit is in the order of 0.5 mK. However, this calculations are neglecting influences such as the micromotion, the Zeeman splitting and heating due to electrical field noise, making it

difficult to experimentally reach this limit. A derivation including additional heating due to micromotion is given in [Cir94].

2.2.4. Optical pumping and state initialisation

Population is accumulated in one of the two Zeeman sub-levels of the $4^2S_{1/2}$ state in order to initialise the system in a pure state, *e.g.* to prepare it for experiments involving coherent manipulation of the $4^2S_{1/2}$ to $3^2D_{5/2}$ transition. This can be accomplished in two different ways.

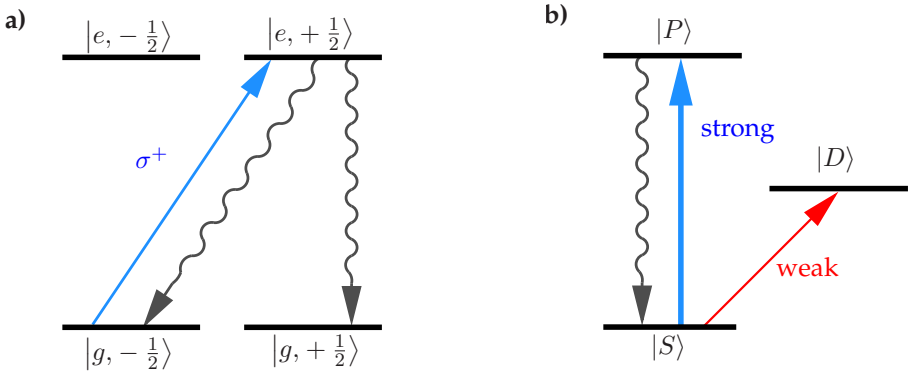

Figure 2.4.: State initialisation and determination. **a)** The $4^2S_{1/2}$ to $4^2P_{1/2}$ transition is driven with polarised light, to initialise the popuation in one of the Zeeman sublevels. As an example, the variant with σ^+ polarised light is shown, where only excitations from the $m = -\frac{1}{2}$ ground state take place. After a few scattering events, this transfers the population to the $m = +\frac{1}{2}$ state. **b)** Determination of the population distribution of a superposition between $|S\rangle$ and $|D\rangle$. Driving the stronger coupled $|S\rangle$ to $|P\rangle$ transition projects the state either in $|S\rangle$ or $|D\rangle$, rendering the system fluorescing or dark, respectively. The exact population distribution can be determined statistically by repetition of this experiment.

One option is to excite the $4^2S_{1/2}$ to $4^2P_{1/2}$ transition with circularly polarised light directed parallel to the B-field vector. Depending on the handedness of the polarised light, it will only excite from one sublevel, whereas the other remains unaffected by this laser, effectively becoming a "dark" state. After a few scattering events, this process leads to a shift of the entire population to the dark state (compare Fig. 2.4 a)).

The other option is to use the $4^2S_{1/2}$ to $3^2D_{5/2}$ transition in a similar way, namely by coherently coupling the $m = -\frac{1}{2}$ groundstate to the $m = +\frac{3}{2}$ exited state via π-pulses of the respective frequency. This renders the $m = +\frac{1}{2}$ unaffected and after a few cycles the population will accumulate in this state. In this scheme, the excited state is additionally coupled to the fast decaying $4^2P_{1/2}$ level to accelerate the process.

2.2.5. State detection

Many measurement protocols regarding resolved sideband spectroscopy require determination of electronic state population [Roo00]. For the experiments reported here this concerns any superposition between the weakly coupled $4^2S_{1/2}$ and the $3^2D_{5/2}$ states. Such a state can be projected and subsequently read out by collecting the fluorescence light while driving the strong $4^2S_{1/2}$ to $4^2P_{1/2}$ transition (compare Fig. 2.4 b)). No light will be scattered if the ion is in the "dark" $3^2D_{5/2}$ state, whereas fluorescence can be observed if it was in the $4^2S_{1/2}$ state. Thus, a states occupation can be determined by repetitively preparing, projecting and reading out the state.

2.2.6. Sideband cooling

As a perquisite for resolved-sideband cooling of a mode, the trap frequency ω in the respective direction has to be higher than the absorption width Γ of the transition. This enables to resolve the sidebands and to tune the laser to the frequency of the first red sideband (compare 2.2.1). Each excitation on this transition reduces the number of motional quanta by one (see Fig. 2.5 a)).

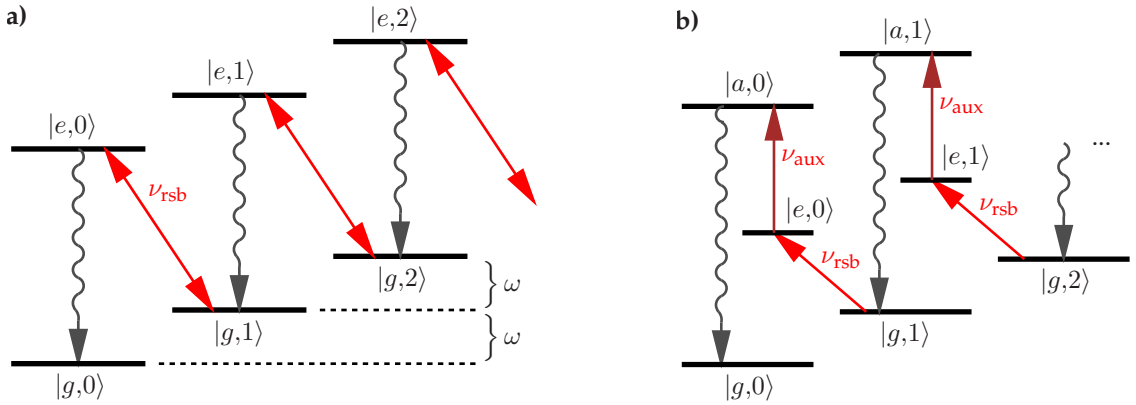

Figure 2.5.: Sideband cooling: **a)** Each excitation to the excited state $|e\rangle$ reduces the number of vibrational quanta by one whereas spontaneous emission does not change the motional state. **b)** The lifetime of the excited state can be shortened artificially by coupling it to an auxiliary level $|a\rangle$ which is decaying at a faster rate than the original state.

In contrast, the subsequent spontaneous emission preserves the motional state population, as in the Lamb-Dicke regime most of the spontaneous emission events occur on the carrier transition [Roo00].[5] To reach this regime, a Doppler cooling stage has to precede the sideband cooling. In this work, the sideband cooling is accomplished by applying π-pulses, rather than continuously driving the cooling transition (compare Fig. 2.5). Additionally,

[5] Outside the Lamb-Dicke regime red and the blue sideband transitions become likely, causing diffusion of the motional state population [Lei03].

the lifetime of the upper level is artificially shortened by coupling it to a faster decaying state using an additional laser. In this way, the rate of spontaneous emission following each excitation is elevated, eventually increasing the cooling rate (see Fig. 2.5 b)). For the calcium ion used here, the cooling transition is the $4^2S_{1/2}$ to $3^2D_{5/2}$ transition and the auxiliary level is the $4^1P_{3/2}$ state.

2.2.7. Thermometry

A vibrational mode in a thermal state of temperature T is fully characterised by its mean phonon number $\bar{n}$. The Rabi frequency of a transition depends on the motional state n (compare 2.2.1). Hence, the Rabi oscillation of the excitation probability of a mode in a thermal state

$$p_{|e\rangle}^{(\bar{n})}(t) = \sum_n \langle e,n|\, \hat{U}(t)\hat{\rho}_{\text{th}}\hat{U}^\dagger(t)\, |e,n\rangle = \sum_n p_n^{(\bar{n})} \sin^2\left(\frac{1}{2}\Omega_{n,n+l}t\right), \tag{2.21}$$

is a superposition of the oscillations of the respective number states, weighted by the thermal occupation probability

$$p_n^{(\bar{n})} = \langle n|\, \hat{\rho}_{\text{th}}\, |n\rangle = \frac{\bar{n}^n}{(\bar{n}+1)^{n+1}}. \tag{2.22}$$

The time evolution operator is given by $\hat{U}_{\text{res}}(t) = e^{-\frac{i}{\hbar}\hat{H}_{\text{int}}^I t}$. For the Rabi frequencies, $l = 0$ corresponds to the carrier, $l = -1$ to the first red sideband and $l = 1$ to the first blue sideband. Depending on $\bar{n}$, the dephasing of the different Rabi oscillation components of this distribution leads to a characteristic damping of the oscillation. The Rabi oscillations on the carrier and those on the first red and blue sidebands linearly depend on Ω_0, the Rabi frequency of the transition of the free ion. Hence, the mean phonon number $\bar{n}$ can be extracted without explicitly knowing Ω_0 by simultaneously fitting these three Rabi oscillations, taking into account a thermal distribution of the motional quanta.

Since phonons obey Bose-Einstein statistics, the mean occupation of a mode with temperature T in thermal equilibrium is given by [Sch11]

$$\bar{n} = \frac{1}{e^{\frac{\hbar\omega}{k_{\text{B}}T}} - 1}, \tag{2.23}$$

where k_{B} is the Boltzmann constant and ω the trap frequency. Accordingly, the temperature can be calculated from the mean phonon number by

$$T = \frac{\hbar\omega}{k_{\text{B}} \ln\left(\frac{\bar{n}+1}{\bar{n}}\right)}. \tag{2.24}$$

The 1-σ size of the thermal wavepacket can be determined from [Knü12]

$$\sigma_{\text{th}} = \sqrt{\frac{\hbar}{2m\omega}\left(2\bar{n}+1\right)} = \sqrt{\frac{\hbar}{2m\omega}\coth\left(\frac{\hbar\omega}{2k_{\text{B}}T}\right)}. \tag{2.25}$$

With regards to the implementation of an ion source by extracting ions from the trap, this means, the source size can be decreased by raising the trap frequency, which however, comes at the cost of a higher transversal momentum, eventually increasing the beam divergence. The ideal combination of source size and beam divergence depends on the application. In general a lens can always reverse the divergence and demagnify the source size, but practically apertures, lens errors and voltage limits set a limit to this. Hence, in the next section the emittance, a more general measure for characterising and comparing ion sources is presented. It is based on the phase space volume occupied by the beam and thus comprises both, the source size and the beam divergence.

2.3. Ion source

In this work, a deterministic ion source is realised by extracting single ions from the Paul trap by means of electric fields. Throughout literature, the two most significant figures of merit to characterise ion sources are the emittance and the brightness. This section is devoted to introduce and explain both. However, for the deterministic ion trap-source, the emittance is of greater interrest. The reason for this is that typically brightness is used as a measure for how good one can trade current density for probe size. This is not possible with a deterministic source, at least not if the deterministic property should be retained. The following derivation is based on [McC16].

2.3.1. Emittance

According to the Liouville theorem the phase space volume of an ensemble of particles in a conservative potential is conserved [Wie15]. A quantity which is connected to this volume is the emittance. Fig. 2.6 shows the spatial evolution of the emittance. For a beam

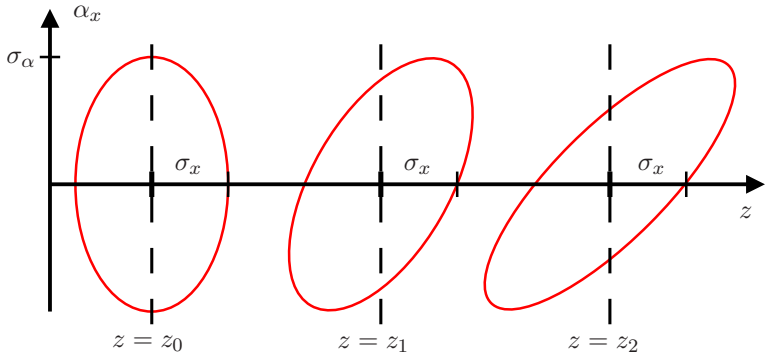

Figure 2.6.: Spatial evolution of the emittance, depicted as the area within the red ellipse. The example shows the emittance of the x component of a divergent beam along z, where the transversal direction x is drawn to the same axis (z). At the source ($z = z_0$) the angular distribution and the spatial distribution are uncorrelated. Along the beam, the angular distribution σ_α does not change while the beam spreads in x direction depending on the angle α_x, but the emittance remains constant.

consisting of an ensemble of trajectories with positions x and angles α_x with respect to the optical axis, the emittance in one spatial direction is defined as

$$\epsilon'_x = \left(\langle x^2 \rangle \langle \alpha_x^2 \rangle - \langle x\alpha_x \rangle^2 \right)^{1/2}. \tag{2.26}$$

This quantity is dependent on the longitudinal energy U, therefore a normalised emittance can be calculated with

$$\epsilon_x = \epsilon'_x \sqrt{U} = \left(\langle x^2 \rangle \langle \alpha_x^2 \rangle - \langle x\alpha_x \rangle^2 \right)^{1/2} \sqrt{U}. \tag{2.27}$$

If the position is completely uncorrelated with the angle, as it is the case for most particle sources, the relation simplifies to

$$\epsilon_x = \left(\langle x^2 \rangle \langle \alpha_x^2 \rangle \right)^{1/2} \sqrt{U}. \tag{2.28}$$

The ion-trap source can be assumed to be Gauss distributed. In this case $\langle x \rangle = \sigma_x$ applies, with σ_x being the standard deviation. Also the radial energy is dominated by the thermal energy an thus $\langle \alpha_x \rangle \sqrt{U} = \sqrt{k_\mathrm{B} T/2}$ holds, where k_B is the Boltzmann constant, T is the temperature of the source and the factor $1/2$ is a result of the equipartition theorem. Hence, the emittance can be written

$$\epsilon_x = \sigma_x \sqrt{k_\mathrm{B} T/2}. \tag{2.29}$$

However, this relation does not hold in the zero temperature limit, because the Heisenberg uncertainty principle prevents the (thermal) energy from becoming zero. In the case of the ion-trap source, the energy is that of a harmonic oscillator, which is $E = \hbar\omega \left(\bar{n} + 1/2\right)$ for one mode. Using equation (2.25) the emittance can now be calculated with

$$\epsilon_x(\bar{n}) = \sigma_x \sqrt{E/2} = \frac{\hbar}{\sqrt{2m}} \left(\bar{n} + \frac{1}{2} \right). \tag{2.30}$$

Here, $\bar{n}$ can be expressed in temperature T with equation (2.23), yielding

$$\epsilon_x(T) = \frac{\hbar}{\sqrt{2m}} \left(\frac{1}{e^{\frac{\hbar\omega}{k_\mathrm{B} T}} - 1} + \frac{1}{2} \right). \tag{2.31}$$

The ground state emittance is thus given by

$$\epsilon_{x,\mathrm{gs}} = \lim_{T \to 0} \epsilon_x(T) = \frac{\hbar}{2\sqrt{2m}}. \tag{2.32}$$

This quantity represents a general limit to the emittance which is independent from the trap frequency. This can also be considered as a consequence of the Heisenberg uncertainty principle. For calcium this limit is $3.61 \cdot 10^{-13}\,\mathrm{m\,rad}\sqrt{\mathrm{eV}}$. Section 7.2 contains a comparison with state of the art ion sources.

2.3.2. Brightness

Although, the emittance is a measure for how small a beam of a source can potentially be focused, it provides no information about the current or its current density. In contrast, the normalised brightness is defined as the the current density $J = \partial I/\partial A$, per solid angle Ω, per beam energy U

$$B(x,y) = \frac{1}{U}\frac{\partial^2 I}{\partial A \partial \Omega} = \frac{1}{U}\frac{\partial J(x,y)}{\partial \Omega}. \tag{2.33}$$

Sources are often compared in terms of their peak normalised brightness B_{peak}. This quantity can also be expressed as a function of the total current I_0 and the emittance

$$B_{\text{peak}} = \frac{I_0}{4\pi^2 \epsilon_x \epsilon_y}. \tag{2.34}$$

As already mentioned previously, for a deterministic source, the brightness is of minor concern than it is for stochastic sources. Moreover, as in this work, prove of principle applications of a deterministic source are presented, where the focus is not on repetition rate, a comparison in terms of brightness seems to be of little relevance. However, with regard to a future improvements of the repetition rate it can be instructive to discuss the potential in terms of brightness.

2.4. Ion optics

Several of the experiments presented in this work are employing an electrostatic einzel lens to focus a beam of ions. In this section an analytical framework is presented which permits an interpretation of these experiments, taking lens errors into account.

2.4.1. Foundations

Analog to optics, the trajectories of charged particles within a lens can be described geometrically. According to [Dem09] the distance r_2 of a trajectory to the optical axis at any point S_2 behind the principal plane of an ideal lens is given by:

$$r_2 = \left(1 - \frac{S_2}{f}\right) r_1 + \left(S_1 + S_2 - \frac{S_1 S_2}{f}\right) \alpha, \tag{2.35}$$

where f is the focal length, S_1 is the distance to the source, r_1 the distance of the source to the optical axis and α is the angle of the incident beam (see Fig. 2.7). Given a source with a spatial distribution $\rho_r(r_1)$, an angular distribution $\rho_\alpha(\alpha)$ and assuming both distributions are uncorrelated, the 1-σ radius at S_2 can be calculated with

$$\Delta r_2 = \sqrt{\langle r_2^2 \rangle - \langle r_2 \rangle^2} = \sqrt{\langle r_2^2 \rangle} = \left(\int_{-a}^{a} \int_{-\infty}^{\infty} \rho_r(r_1)\, \rho_\alpha(\alpha)\, r_2^2(r_1,\alpha)\, \mathrm{d}r_1 \mathrm{d}\alpha \right)^{\frac{1}{2}}, \tag{2.36}$$

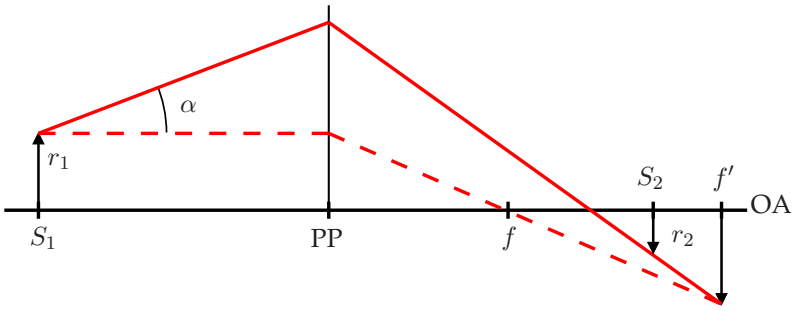

Figure 2.7.: Beam paths of a thin lens: a parallel beam (dashed red line), leaving the source at S_1 is crossing the optical axis (OA) at the focal length f behind the principal plane (PP). A beam which is leaving the source from the same point at a distance r_1 from the OA and under the angle α (red line), has a distance r_2 from the OA at a point S_2 and intersects the parallel beam in the focal plane f'.

where $\langle r_2 \rangle^2 = 0$ was used taking into account a beam symmetric around the optical axis. Assuming ρ_r and ρ_α being Gauss distributed,

$$\rho_r(r_1) = \frac{1}{\sigma_r \sqrt{2\pi}} e^{-\frac{1}{2}\left(\frac{r_1}{\sigma_r}\right)^2}, \tag{2.37}$$

$$\rho_\alpha(\alpha) = \frac{1}{\sigma_\alpha \sqrt{2\pi}} e^{-\frac{1}{2}\left(\frac{\alpha}{\sigma_\alpha}\right)^2}, \tag{2.38}$$

equation (2.36) can be solved analytically yielding

$$\Delta r_2 = \sqrt{\left(1 - \frac{S_2}{f}\right)^2 \sigma_r^2 + \left(S_1 + S_2 - \frac{S_1 S_2}{f}\right)^2 \sigma_\alpha^2}, \tag{2.39}$$

when taking into account $\sigma_\alpha \ll a$. This allows for determining the 1-σ source size σ_r, the 1-σ beam divergence of the source σ_α and the focal length f, by measuring the beam radius at different positions around the beam focus and fitting equation (2.39) to this data. Calculating the minimum of equation (2.39) result in

$$\Delta r_{2,\min} = \frac{f \sigma_r \sigma_\alpha}{\sqrt{(f - S_1)^2 \sigma_\alpha^2 + \sigma_r^2}}. \tag{2.40}$$

2.4.2. Aberration

The aberration of a lens is the deviation from an ideal lens as described by the paraxial approximation. There are two classes of aberrations, monochromatic and chromatic aberrations. Monochromatic aberrations result from geometrical imperfections of the focussing field and even appear for monochromatic particle ensembles. Chromatic aberrations are caused by dispersion, *i.e.* the focussing is dependent on the energy of the particle.

Among the monochromatic aberrations only the spherical aberration is of particular interest for this experiment. Off-axis astigmatism only can occur as a result of a mechanical tilt of the beam with respect to the principal plane of the lens, as in the present experiment, scanning of the beam with respect to the sample in the focal plane is accomplished by moving the sample rather than changing the incident angle of the beam. During the experiments, small deviations of the focal lengths for the two different directions of the focal plane were observed. The amount of these differences was in the order of the depth of focus. However, these deviations were not always present and were also not stable among different days of occurrence. This means that they could not be attributed to a constant tilt of the lens, and therefore off-axis astigmatism as a result of a constant mechanical tilt can be ruled out. The same applies for on-axis astigmatism, as for example would result from a lens being not rotationally symmetric. In addition, the lack of experimental means to change the incident angle of the ion beam in a controlled way, prevents from evaluating systematic investigations of the quantitative extent of this error and is therefore not subject of this thesis. Similar considerations apply for for the coma.

Spherical aberration

In the presence of spherical aberration the focal length f of an incident beam is shifted towards the lens by Δf, depending on its distance to the optical axis $x = r_1 + S_1\alpha$ (compare Fig. 2.8). Since spherical aberration is symmetric around the optical axis, odd powers of x

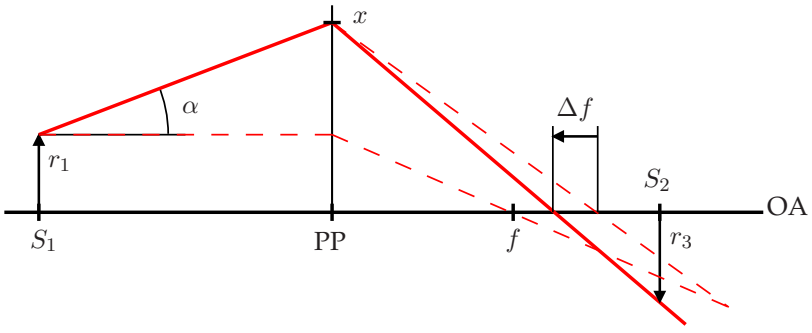

Figure 2.8.: Chromatic aberration shifts the point where the beam (red thick line) crosses the optical axis (OA) by Δf towards the lens compared to the case without chromatic aberration.

vanish and Δf can be written as

$$\Delta f = c_2 x^2 + \mathcal{O}(x^4), \tag{2.41}$$

where c_2 is a constant. Substituting f with $f - \Delta f$ in equation (2.35) and subsequently calculating the series expansion with respect to α yields

$$r_3 = \left(S_1 + S_2 - \frac{S_1 S_2}{f}\right)\alpha + \frac{c_2 S_1^3 S_2}{f^2}\alpha^3 + \mathcal{O}(\alpha^4). \tag{2.42}$$

Here r_1 was set to zero as we are only interested in trajectories coming from a point on the optical axis. This equation can be used to measure the aberration coefficient c_2 by

changing the incident angle α and measuring the corresponding r_3 at a known distance S_2.

Taking spherical aberration into account and assuming the beam divergence being Gauss distributed with a sigma of σ_α, where again $\sigma_\alpha \ll a$, the 1-σ radius at S_2 now can be calculated with

$$\Delta r_3 = \sqrt{\langle r_2^2 \rangle - \langle r_2 \rangle^2} = \sqrt{\langle r_2^2 \rangle} = \left(\int_{-a}^{a} \rho_\alpha(\alpha)\, r_3^2(\alpha)\, \mathrm{d}\alpha \right)^{\frac{1}{2}}. \tag{2.43}$$

The minimum of Δr_3 at $S_{2,\mathrm{min}}$ can be calculated by solving $\frac{\partial \Delta r_3}{\partial S_2} = 0$ with respect to S_2. Inserting $S_{2,\mathrm{min}}$ into equation (2.43) gives the minimum radius $\Delta r_{3,\mathrm{min}}$. Evaluating the series expansion of $S_{2,\mathrm{min}}$ and $\Delta r_{3,\mathrm{min}}$ with respect to σ_α yields

$$S_{2,\mathrm{min}} \approx -\frac{f\, S_1}{f - S_1} - \frac{3 c_2 S_1^4}{(f - S_1)^2} \sigma_\alpha^2. \tag{2.44}$$

$$\Delta r_{3,\mathrm{min}} \approx \sqrt{6} \frac{c_2\, S_1^4}{f(f - S_1)} \sigma_\alpha^3. \tag{2.45}$$

The first term in equation (2.44) is the focal length of an ideal lens. The second term is the shift of the beam focus due to spherical aberration. This minimal beam radius in in the presence of spherical aberration often is referred to as *disk of least confusion* [Ege05]. Throughout literature, the most common definition of the spherical aberration is

$$\Delta r_{3,\mathrm{min}} = C_\mathrm{s} {\sigma_\alpha}_\mathrm{i}^3, \tag{2.46}$$

where ${\sigma_\alpha}_\mathrm{i} = \sigma_\alpha / M$ is the sigma spread of the beam angle at the focus and $M = S_2/S_1$ is the magnification of the lens. When equating coefficients with equation (2.45), C_s is thus given by

$$C_\mathrm{s} = \sqrt{6} \frac{c_2\, S_1^4}{f(f - S_1)} \cdot M^3. \tag{2.47}$$

Chromatic aberration

Chromatic aberration arises from the fact that the focal length of an electrostatic lens depends on the kinetic energy of the focussed particles. According to [Ege05] this can be expressed by the relation $f = cE$, where E is the kinetic energy of the particles and c is a constant of proportionality, independent of E. Thus, a change in energy ΔE results in a change of the focal length

$$\Delta f = \frac{f}{E} \Delta E. \tag{2.48}$$

In the same way as for the spherical aberration in equation (2.35), f is substituted with $f - \Delta f$ and the series expansion is calculated with respect to ΔE. This results to

$$r_3 = \left(S_1 + S_2 - \frac{S_1 S_2}{f} \right) \alpha + \frac{S_1 S_2 \alpha}{fE} \Delta E + \mathcal{O}(\Delta E^2), \tag{2.49}$$

where r_1 was set to zero, such that only rays coming from the optical axis are considered. The resulting aberration is therefore referred to as *axial chromatic aberration*. The 1-σ radius Δr_3 of a beam emerging from a source with a normally distributed divergence with sigma σ_α can be calculated using (2.37). Evaluating the series expansion of the minimal radius $\Delta r_{3,\text{min}}$ with respect to $\sigma_{\Delta E}$ in first approximation yields

$$\Delta r_{3,\text{min}} \approx \frac{-S_1^2 \sigma_\alpha}{(f - S_1)E} \sigma_{\Delta E} = \frac{-S_1^2 M \sigma_\alpha}{fE} \sigma_{\Delta E}, \tag{2.50}$$

where $M = S_2/S_1$ is the magnification. The coefficient of chromatic aberration C_C has historically been defined as $\Delta r = -MC_\text{C}\alpha\frac{\Delta E}{E}$ [Hed00]. Comparing both equations results to $C_\text{C} = S_1^2/f$. This coefficient is called the *coefficient of axial chromatic aberration*, to distinguish it from the chromatic aberration caused by a beam shifted parallel to the optical axis. The latter is the case, if α rather than r_1 is set to zero in equation (2.49). The corresponding aberration is called *lateral chromatic aberration*. Assuming the source radius r_1 being distributed normally with sigma σ_r, the first order approximation with respect to $\sigma_{\Delta E}$ of the minimum radius, calculated using equation (2.37), is given by

$$\Delta r_{3,\text{min}} \approx \frac{\sigma_r}{E} \sigma_{\Delta E}. \tag{2.51}$$

The corresponding coefficient C_D is defined as $\Delta r = -MC_\text{D} r_1 \frac{\Delta E}{E}$, which yields $C_\text{D} = 1/M$.

2.4.3. Numerical methods

The purpose of this section is to give a brief overview of the foundations of the numerical simulation methods used later in this work. These methods are applied to model fields of a linear Paul trap with realistic geometry, where the trapping of an ion from a beam, the storage of this ion as well as its extraction is simulated. A similar simulation has been performed for the ion lens, which is used to focus the ions extracted from the trap.

In a first step, time dependent and true to scale electrical fields originating from any given geometry of conducting surfaces are calculated. This procedure is based on the boundary element method (BEM) which is combined with a fast multipole method (FMM) to speed up the matrix multiplications [She07]. In a second step the time dependent trajectories of charged particles within these fields can be simulated with a spatial resolution down to the nanometer scale. This is accomplished using the Verlet integration method.

The following derivation is based on [She07], where also further details can be found. A more application-oriented discussion in a broader context can be found in [Sin10]. The first goal is to determine the potential in the vicinity of an electrode with a given surface potential. As there are no free charges outside the surfaces of the electrodes, the problem satisfies the Laplace equation:

$$\triangle \phi = 0. \tag{2.52}$$

In order to solve this equation for the problem above, Stokes' theorem can be used:

$$\int_V G(x,x') \; \triangle_{x'} \; \phi(x') - \phi(x') \; \triangle_{x'} \; G(x,x') \, \mathrm{d}V' = \int_S G(x,x') \, \frac{\partial \phi(x')}{\partial n} - \phi(x') \, \frac{\partial G(x,x')}{\partial n} \, \mathrm{d}S'. \tag{2.53}$$

From $G(x,x') = \frac{1}{4\pi} \frac{1}{|x-x'|}$ follows $\triangle_{x'} G(x,x') = -4\pi \, \delta(x - x')$. Substituting this as well as the Laplace equation in equation (2.53) yields:

$$\phi(x) = \frac{1}{4\pi} \int_S G(x,x') \, \frac{\partial \phi(x')}{\partial n} - \phi(x') \, \frac{\partial G(x,x')}{\partial n} \, \mathrm{d}S'. \tag{2.54}$$

The surface of the electrode is now divided into small elements ΔS_j with constant values. This yields:

$$\sum_{j=1}^{N} f_{ij} \phi_j = \sum_{j=1}^{N} g_{ij} q_j, \qquad \text{for} \quad i = 1, \ldots, N, \tag{2.55}$$

where

$$g_{ij} = \int_{\Delta S_j} G(x_i,x') \, \mathrm{d}S'. \tag{2.56}$$

and

$$f_{ij} = \delta_{ij} + \int_{\Delta S_j} \frac{\partial G(x_i,x')}{\partial n} \, \mathrm{d}S'. \tag{2.57}$$

Rearranging equation (2.55), by writing all unknown boundary elements into a vector λ yields a linear system of equations:

$$A\lambda = b. \tag{2.58}$$

Here, b is known and A is a coefficient matrix whose calculation requires $\mathcal{O}(N^2)$ steps. Using the FFM, the computational cost can be reduced to $\mathcal{O}(N)$ steps, which is critical for the practicality of the procedure.

The basic principle of this method is to split up the contributions of a point to the potential into a part in the close vicinity, where the charge distribution is evaluated conventionally, and a part in the far range, where the potential is calculated via the multipole expansion. To this goal the space of interest is divided into cubes of a given size. The close vicinity of a cube is defined as all cubes which directly touch this cube. A hierarchical structure is defined by combining eight cubes to a cube of twice the edge length of a cube. Charges combined by a cube are referred to as clusters. Clusters which are not in the close vicinity are called well-separated.

The following algorithm can be divided into several steps. Starting with the smallest cube level, a multipole expansion is performed around the centre of the cube, including all charges within the cube. Ascending in the hierarchy, for each bigger cube a multipole expansion is performed around the centre. This is accomplished by adding up all contributions from the multipole expansions of the smaller cubes included in the bigger one, by relocating them into the centre of this bigger cube.

In the next step, descending in the hierarchy, all charges which are not included in the current cluster, *i.e.* the field originating from all well-separated clusters, are added in each refinement step. For each following step of the iteration, the result of the current

calculation is relocated into the centre of the next lower level in the hierarchy. Thus, when reaching the lowest level, the highest resolution of the local expansion of the far-field is achieved. Finally the respective contribution of the potential from the close vicinity has to be added.

The Verlet method which is used to calculate the ion trajectories, is a numerical method to integrate the equation of motion. With this method, the error in position made per time step t is $\mathcal{O}(\Delta t^4)$.At the same time, the intermediate step of calculating the velocity is not required, as it would be the case with the Euler method. The derivation follows from the Taylor expansion in both directions of time:

$$x(t+\Delta t) = x(t) + v(t)\Delta t + \frac{a(t)}{2}\Delta t^2 + \frac{\dot{a}(t)}{6}\Delta t^3 + \mathcal{O}(\Delta t^4) \tag{2.59}$$

and

$$x(t-\Delta t) = x(t) - v(t)\Delta t + \frac{a(t)}{2}\Delta t^2 - \frac{\dot{a}(t)}{6}\Delta t^3 + \mathcal{O}(\Delta t^4). \tag{2.60}$$

Adding both equations, yields

$$x(t+\Delta t) = 2x(t) + x(t-\Delta t) + a(t)\Delta t^2 + \mathcal{O}(\Delta t^4) \tag{2.61}$$

If the velocity is also required, it has to be calculated separately:

$$V(t) = \frac{x(t+\Delta t) - x(t-\Delta t)}{2\Delta t} + \mathcal{O}(\Delta t^2) \tag{2.62}$$

However, here the error is $\mathcal{O}(\Delta t^2)$. Therefore, in the simulation a modified version of the Verlet algorithm is used:

$$x(t+\Delta t) = x(t) + v(t)\Delta t + \frac{a(t)}{2}\Delta t^2 +, \tag{2.63}$$

$$v(t+\frac{\Delta t}{2}) = v(t) + \frac{a(t)}{2}\Delta t, \tag{2.64}$$

$$a(t+\Delta t) = -\frac{1}{m} \bigtriangledown V(r(t+\Delta t)), \tag{2.65}$$

$$v(t+\Delta t) = v(t+\frac{\Delta t}{2}) + \frac{a(t+\Delta t)}{2}\Delta t. \tag{2.66}$$

This method is also called *leapfrog integration* or *velocity Verlet*. Notably this method is equivalent to the *semi-implicit Euler-method*.

2.5. Methods of measurement

2.5.1. Focus measurement

An easy and reliable way to measure the radius r and the position x_0 of a particle beam, is to use a profiling edge, which is stepped into the beam while recording the transmission signal. The probability of detecting an ion depends on the coverage of the beam profile which is a function of the edge position and the profile of the beam in the radial plane.

It can be derived by convolving a two-dimensional step function $h(x - x')$ at position x', representing the edge, with the probability density distribution of the beam profile $f(x,y)$. This yields

$$p(x,y) = (h * f)(x') = \int f(x',y)h(x - x')\,dx'. \tag{2.67}$$

Without loss of generality the edge $h(x - x')$ was chosen to have the step in x-direction and thus must be movable in this direction. This also implies that the edge is spatially invariant in y-direction. The probability as a function of the position x independent of y is obtained by marginalising over y

$$p(x) = \int p(x,y)\,dy. \tag{2.68}$$

Assuming a rotationally symmetric Gaussian beam profile, the y integration can be evaluated first and the probability density distribution amounts to

$$p(x) = \int \frac{a}{\sigma\sqrt{2\pi}}\, e^{-\frac{1}{2}\left(\frac{x'-x_0}{\sigma}\right)^2} h(x - x')\,dx' = \frac{a}{2}\,\mathrm{erfc}\left[\frac{x - x_0}{\sigma\sqrt{2}}\right], \tag{2.69}$$

where $a \in [0,1]$ accounts for the finite detector efficiency. Equation (2.69) now describes the probability $p(x)$ of detecting an ion from a beam with a Gaussian profile, at position x_0 and 1-σ radius $r = \sigma$, when it is covered by a profiling edge with position x, while having a detection efficiency of a.

2.5.2. Two-sample deviation

The two-sample deviation or Allan deviation was originally invented by David W. Allan to evaluate the frequency stability of clocks or oscillators [San99]. It permits to characterise different noise processes and systematic errors which can prevent the convergence of estimators such as the standard deviation. This concept can also be applied to other measurement parameters with a constant mean value. The two-sample deviation is defined as the mean value of the differences between consecutive measurements of a parameter x as a function of the sample size n. It therefore reads

$$\sigma(n) = \sqrt{\frac{1}{2(N-1)} \sum_{i=0}^{N-1} \left(\bar{x}_{i+1}(n) - \bar{x}_i(n)\right)^2}, \tag{2.70}$$

where $\bar{x}_i(n)$ is the mean value for the i-th measurement, having a sample size of n. When measuring frequency this sample size is defined by the integration time. In this work the two-sample deviation is used to evaluate the stability of the parameters beam position and beam radius. Thereby, x is a single measurement of one of these parameters and the $\bar{x}_i(n)$ are then calculated by averaging over n consecutive single measurements.

2.5.3. Bayes experimental design

In the context of single ion microscopy, the Bayesian experimental design method [Lin56, Gue07, Pez07, Bra12] can be harnessed to maximise the gain of information for each probe event. By employing this technique, it is possible to measure parameters of structures that can be modelled by a parametrised transmission function determined from prior knowledge of the geometry. In this section, first, the method is introduced theoretically, and then it is explained by applying it for the case of the profiling edge measurement.

Algorithm

In the Bayesian approach to parameter estimation, the knowledge about the value of a parameter θ, given by pre-existing information, is expressed by the *prior* probability distribution function (PDF) $p(\theta)$. Information from the outcome y of a new measurement is subsequently incorporated using the Bayes update rule, yielding a *posterior* PDF:

$$p(\theta|y,\xi) = \frac{p(y|\theta,\xi)p(\theta)}{p(y|\xi)}. \tag{2.71}$$

Here, the right hand side is the product of the prior PDF and the statistical model of the measurement $p(y|\theta,\xi)$, which is the probability to observe an outcome y, given the parameter values θ and design parameters ξ. Thereby, ξ contains the free control parameters of the experiment. Normalisation is provided by dividing by the marginal probability of observing y, which is $p(y|\xi) = \int p(y|\theta,\xi)p(\theta)d\theta$.

The Bayes experimental design method consists in maximising the information gain per measurement by the appropriate choice of the design parameters. The information gain of a measurement with outcome y and control parameters ξ is expressed by the *utility* $U(y,\xi)$, which is the difference in Shannon entropies of the posterior and prior PDFs:

$$U(y,\xi) = \int \ln(p(\theta|y,\xi))p(\theta|y,\xi)d\theta - \int \ln(p(\theta))p(\theta)d\theta.$$

Averaging the utility over the measurement outcomes yields a quantity independent of the hitherto unknown observation

$$U(\xi) = \int U(y,\xi)p(y|\xi)dy, \tag{2.72}$$

which can be optimised with respect to ξ. Carrying out the measurement with the obtained control parameters ξ thus ensures optimal information gain.

For the case of the profiling edge measurement, the design parameter is the profiling edge position, while the parameters to be determined are the beam position x_0, its radius σ and the detector efficiency a, *i.e.* $\theta = (x_0,\sigma,a)$. The outcome of the measurement is binary $y = \{0,1\}$, as it is given by the detector signal which is $y = 1$ an ion is detected and $y = 0$ when no ion is detected. The measurement is modelled by

$$p(y|\theta,\xi) = \begin{cases} \frac{a}{2}\,\mathrm{erfc}\left[\frac{\xi - x_0}{\sigma\sqrt{2}}\right] & \text{if } y = 1 \\ 1 - \frac{a}{2}\,\mathrm{erfc}\left[\frac{\xi - x_0}{\sigma\sqrt{2}}\right] & \text{if } y = 0 \end{cases},$$

which in this case is a convolution of the transmission function of the structure to be imaged which is the profiling edge and a Gaussian beam profile (see section 2.5.1).

Implementation

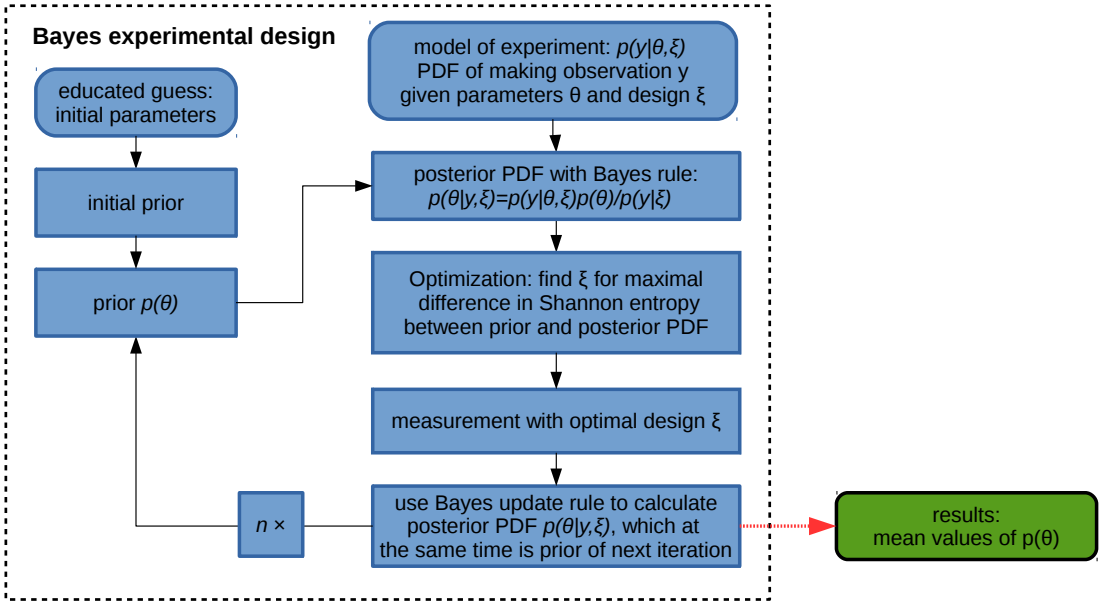

Figure 2.9.: A flowchart of the Bayes experimental design protocol.

Experimentally the sequence is implemented as follows. First, the initial prior is chosen. This is a multidimensional joint PDF, where each dimension represents one measurement parameter and therefore has the same dimensionality as the number of measurement parameters j. Its marginals can be uniform or an educated guess ,*e.g.*, a Gaussian distribution. It is implemented numerically, being a j-dimensional grid of equidistant, weighted and normalised sampling points. For updating the prior to perform the utility calculation (2.72), the Bayes update (2.71) is evaluated individually for each sampling point. The maximising algorithm is realised by calculating the utility for an interval divided into equidistant values of the design parameter and recursively repeating this calculation for a smaller interval around the maximum. Five recursions were found to be sufficient to reach the required accuracy without incurring excessive computational expense. Here, the integrals are replaced by sums over all sampling points. Using the measurement outcome of the real experiment performed at the calculated optimal design parameter value, the Bayesian update (2.71) is applied to calculate the actual posterior PDF, which assumes the role of the prior PDF for the next iteration. The measurement values and their 1-σ confidence interval can be extracted from calculating the mean value and the standard deviation of the marginals of the associated parameter, respectively. The procedure is repeated until an accuracy goal is reached (compare Fig. 2.9). In addition, the implementation provides a zoom function which can reset the limits in one dimension of the PDF

while keeping the number of sampling points, if its standard deviation grows to large or to small compared to the original limits. The values of the redistributed sampling points are set to resemble the PDF before the zoom.

3. Experimental setup of the single ion source

The apparatus which is used for all experiments discussed in this thesis, was predominantly designed for the purpose of single ion implantation and was entirely built in the course of this work. Although there are some characteristics in the construction owing to this application, many of the building blocks can be found similarly in other ion trap experiments. This permits one to rely on established techniques and in combination with using modular components, retaining the flexibility required in a scientific environment. Hence, this experiment not only allowed for experimentation related or complementary to implantation, such as the single ion microscopy, but also enabled rather different experiments as for example the measurement of the Kibble-Zurek effect in ion crystals [Ulm13]. In addition, slightly modified versions of the trap designed here are applied in two other projects, namely an experiment for the creation of Rydberg ions [Fel15] and an experiment for determining the gravitational behaviour of antimatter [Hil14, Ind14, Wol16]. Largely similar trap chips will be used in a new setup for single ion microscopy and sensing, which is currently under development in our group.

The chapter is structured along the functional components of the experimental apparatus. The central building block of the setup is the Paul trap, around which the remaining part of the apparatus is built. Its particular construction is described in the first section 3.1 *Paul trap*. This section also addresses the loading of ion species other than calcium by means of an ion gun. The second section 3.2 *Implantation and microscopy infrastructure* focuses on the detection of ions and the translation of microscopy samples and implantation targets. The electronics to operate the experiment are described in section 3.3 *Electronic setup*. 3.4 *Vacuum setup* comprises a description of the vacuum vessel which is hosting the actual experiments and the infrastructure to sustain the vacuum. The last section 3.5 *Optical setup* describes the laser and imaging system required to operate the trap.

3.1. Paul trap

Since the invention of Paul traps [Pau53], their design has undergone an extensive development in order to match the different requirements for their various and widespread applications. The segmentation of electrodes and the miniaturisation are among the most signficant.

Compared to the trap described here, the single most important difference to typical traps (compare section 2.1.1) which are used for common applications such as metrology or quantum information processing, is the ability to extract ions from the trap, and in this

way realising an ion source. This directly leads to the following concrete requirements for the design of the trap:

- The trap has to be suited for ion extraction.
  - The trap geometry needs to provide a free aperture where ions can leave the trap.
  - The device should enable a narrow velocity distribution and a low emittance. This requires correspondingly high trap frequencies in order to advance laser cooling.
  - The ions should leave the trap with a small and symmetric beam divergence, in order to avoid spherical aberration when focussing. This necessitates an appropriate symmetric electrode structure.
  - The extraction energy should achieve up to 10 keV, which makes dedicated, well insulated electrodes favourable.
- The trap is supposed to permit preparation of a predefined number of ions and loading of other species.
  - The ion number can be reduced by shaping the potential using a segmented trap.
  - There should be the possibility to ionise and load other ion species than calcium.
- The trap geometry should enable laser access and imaging.
  - The open aperture between the electrodes should be in the order of $500\,\mu m$, to allow for laser access without excessively irradiating the electrodes in order to avoid stray light and charging.
  - The cooling laser must have a projection on all principal axes of the trap.
  - The geometry should allow for a close placement of the microscope objective used for imaging of the ions.
  - For micromotion minimisation, it is favourable to have an additional cooling laser whose radial projection is not parallel to the original Doppler laser.[6]
- The required trap frequencies, the desired confinable charge to mass ratios and the limitations owing to the voltage supplies as well as the constraints set by a reasonable trap geometry, lead to the following requirements for the trapping voltages.
  - The trap drive should allow for an amplitude of up to $1000\,V_{pp}$ at a frequency of $10 - 50\,MHz$, whereas the static trapping voltages should reach up to $50\,V$.
  - To allow for fast transport and splitting of ion crystals, the static voltages should be changeable within the timescale of the trap frequency. This also sets the limits for a low pass filtering of these voltages.

[6] This statement assumes the absence of axial micromotion. For the details of micromotion minimisation, please refer to 4.1.2.

- Insulating and non-shielded surfaces near the trapping potential have to be avoided, because they are susceptible for electrical charging.
- The trap must provide the ability to compensate for stray fields. This can be implemented by dedicated electrodes.
- There has to be the possibility to deflect the resulting ion beam in a predictable and controlled way.
- For a favourable Zeeman splitting of the involved levels, a magnetic field in the order of $10\,\mathrm{Gauss}$ at the position of the ion should be applicable. In this regime the Zeeman energy splitting is larger than the energy of the phonons, to ensure the separation of the spectra of the different Zeeman levels and their sidebands. At the same time it has to be smaller than the splitting by the trap drive.

Some of these requirements were introduced as a result of findings and experiences from a previous realisation of a single ion source based on a Paul trap [Sch09a, Sch10b, Sch10a]. In particular this applies to adverse effects from stray fields and to problems with the deflection of the ion beam. The former were an effect of patch charges on insulating surfaces close to the trapping region. They mostly were created by the UV ionisation laser light at $375\,\mathrm{nm}$ and as a result caused drifts of the compensation voltage and the extraction pathway. The latter was a consequence of using the electrodes of the linear segmented Paul trap for beam deflection. This shifted the beam out of the centre of the oscillating radial quadrupole field, which effectively resulted in excess micromotion.

3.1.1. Trap design

Different geometries of linear Paul traps were simulated numerically (compare 2.4.3) in order to compare them with respect to a number of properties, including energy dispersion and emittance. The details about this simulations can be found in the diploma thesis of A. Kehlberger [Keh11]. The considered geometries comprise various configurations of linear segmented traps, all compared with and without additional endcaps for ion extraction. These configurations are

- A cross shaped arrangement of the segmented electrodes, being radially symmetric around the axial direction of the trap, where the diagonally opposing pairs are either supplied with direct current (DC) or RF. This has the advantage of offering relatively symmetric fields when extracting with an endcap and having moderate structural complexity. A drawback is the modulation of the axial energy by axial components of the RF fields when extracting with endcaps.
- A cross shaped arrangement with additional rail like RF electrodes in front of the segmented DC electrode structure. This configuration is the most symmetric. However it is difficult to realise and has relatively shallow axial potentials due to the shielding of the DC electrodes by the RF electrodes.

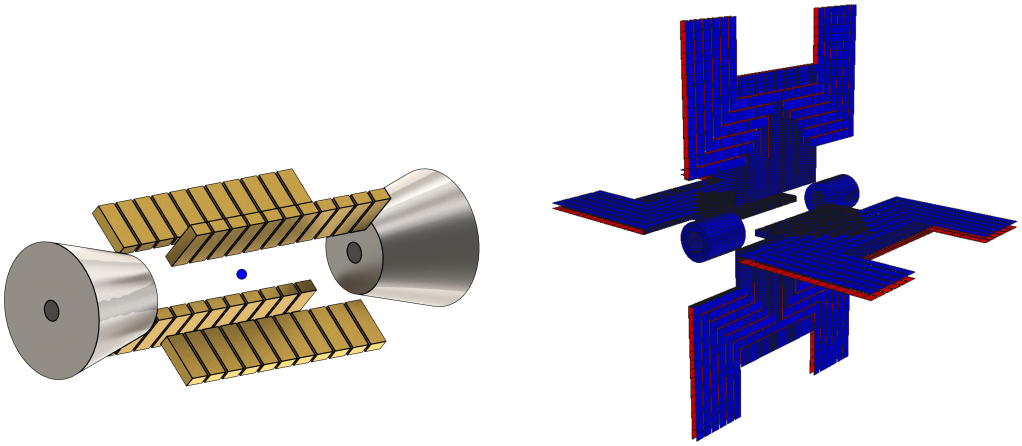

Figure 3.1.: Trap design. **a)** Sketch of the X-shaped spatial arrangement of the segmented electrodes and the endcaps which are used for ion extraction. **b)** Image of the trap model used in the numerical simulations. The DC and the RF electrodes are identical on the front and on the backside of each chip. All chips have additional compensation electrodes which have the same length as the trap [Keh11].

- A layer trap, where two planar layers, each with a slot framed by RF and DC segments, are stacked on top of each other with a insulating spacer in between, similar to [Sch09b]. The alignment and the assembly of this trap is simple, but compared to the others, it is the trap with the most asymmetric trapping and extraction potentials, resulting in a distorted beam.

The comparison placed a particular emphasis on two attributes. Firstly, the characteristics with respect to the trapping potential, in particular the potential depths in radial and axial direction at given voltages as well as the driving frequency. These are all properties important for effective laser cooling. Secondly, the characteristics of the ion extraction, namely energy dispersion, symmetry and emittance of the resulting ion beam. Preference was given to the first option, a linear segmented trap featuring a symmetric X-shaped arrangement of the electrodes with two additional endcaps providing high voltage extraction by means of a hole in the centre (compare Fig. 3.1 a)). Each of the two diagonally opposing pairs are either supplied with solely static voltages or with the oscillating RF voltage for creating the radial confinement, hereafter referred to as DC electrodes and RF electrodes, respectively.

The numerical simulation was used to further optimise the chosen geometry in terms of trap frequencies and emittance when varying the segment width and distance between opposing electrodes [Keh11]. Moreover, the distance of the endcaps to the trap segments was optimised with respect to the emittance. The chosen values and other important dimensions of the trap are shown in Fig. 3.2.

Both the RF and the DC electrode pairs are made from microfabricated alumina chips with a thickness of 125 µm. The actual electrode structure consists of a gold coating, which is functionally structured by laser cutting (compare Fig. 3.3). Details about the fabrication

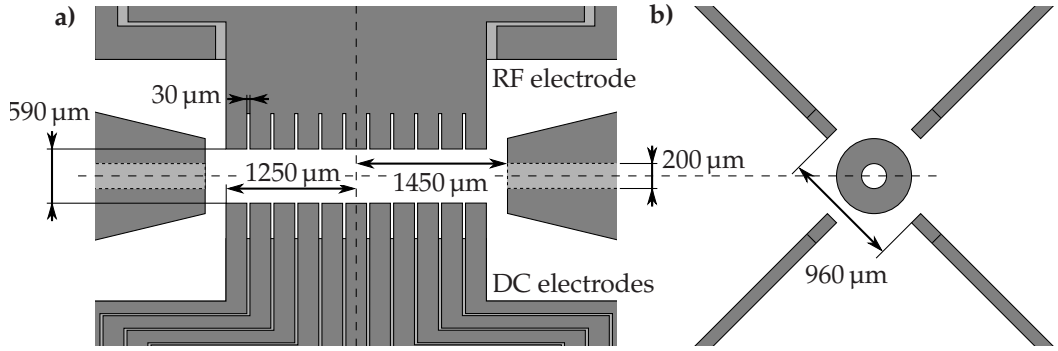

Figure 3.2.: True to scale image of the trap geometry denoting important distances. **a)** The chips with the electrode structure are seen under $45°$ from the side. The chip at the top is supplied with the RF voltage, whereas the chip at the bottom features 11 separate DC electrodes. Axially the trap volume is terminated by endcaps on both sides. They can be supplied with a high voltage for extracting the ions and feature a $200\,\mu m$ aperture where ions can leave the trap. **b)** Cut through the centre of the trap in the radial plane.

process can be found in [Sch09b] and [Keh11]. The DC electrodes are subdivided into 11 segments in order to create the confining electrostatic potential along the axial direction. In addition they feature a finger shaped structure to shield the insulating parts between the electrodes from the ion trap. The chips of the RF electrodes consist of one interconnected electrode surface while having the same finger shaped structure in order to preserve the symmetry of the fields along the trap axis. All four chips have additional electrodes for micromotion minimisation on both sides.

The chips are mounted to a titanium holder, which together with the edges of the endcaps impose constraints to precisely align them with respect to each other and to the axial direction of the trap (see Fig. 3.4). A design drawing of the this holder can be found in Appendix A. The cylindrically symmetric endcaps are aligned coaxially by means of an uninterrupted borehole and are insulated electrically from the holder with ceramic sleeves[7].

The trap electrodes are electrically connected via ball bonded gold wires to a separate ceramic printed circuit board, mounted behind each chip (see Fig. 3.5). This board hosts an in vacuum RC-type low pass filter[8] for each of the DC electrodes and the compensation electrodes, whereas the RF electrodes are looped through without filters. All filtered electrodes are connected to a 51-pin micro-D vacuum feedthrough[9] by copper wires.

[7] Ceramic bushings, *JBC6-10*, MISUMI Europa GmbH, Schwalbach, Germany.

[8] The resistive part is given by the line resistance, whereas the capacitive part is provided by a 10 nF SMD-capacitor (CAP CER 0.01UF 25V X8R 10% 0402 TDK Corporation), shortcutting high frequency components to mass.

[9] 51-pin Micro D MIL-DTL 83513, *W-MDTL8-51-FM-CE-SSG*, VACOM Vakuum Komponenten & Messtechnik, Jena, Germany.

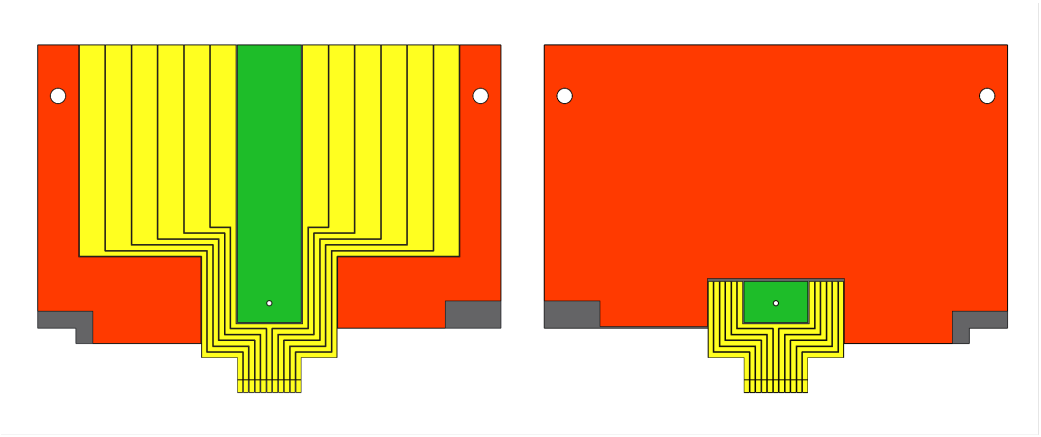

Figure 3.3.: True to scale image of the top (left) and bottom side (right) of the electrode structure on the DC chips. First the finger shaped structure of the electrodes facing the trap is cut from a larger substrate by laser milling (lower sides on the image). In a second step the surface of the substrate is completely gold coated on the top and bottom sides including all side faces of the waver via evaporation. The next step consists in laser-cutting the electrode structure *i.e.* the trenches between the electrodes. Finally the chip is separated by laser cutting it from the original substrate. The area coloured in red depicts the electrodes connected to ground. The ground electrode in the right picture also provides the support to the titanium holder. The gray areas are the insulating parts which align the chips to the endcaps. The yellow areas are the DC electrodes. The green electrodes are the compensation electrodes, where the electrode on the bottom side is connected via the hole in the centre. All electrodes are electrically connected at the upper edge on the top side.

The two RF electrodes are connected to the same pin on a separate feedthrough[10] via a Y-shaped wire with legs of symmetric length. Each endcap is directly connected with a Kapton insulated coaxial cable to a high voltage vacuum feedtrough, featuring a SHV connector on the outside. All feedthroughs are located on a DN63CF flange, which also supports the trap. The trap together with the holder is mounted to this flange by means of another mount (see also Fig. 3.13 blue part), which is designed to permit optical access and high mechanical stability, while at the same time fitting through the open aperture of a DN63CF flange. A calcium oven is attached to this holder, creating an atomic beam which is passing the trapping volume from below. However, in the course of the initial ion extraction experiments this oven has proven to produce excessive heat influx, causing thermal expansion of the trap holder and as a result fluctuations and drifts of the ion beam direction. To avoid this problem, a second calcium oven was mounted directly to one of the DN16CF flanges of the vacuum chamber (compare 3.4.1), irradiating the trap from the side.

[10] 8-pin current feedthrough, *W-HV1-8-CE-CU081*, VACOM Vakuum Komponenten & Messtechnik, Jena, Germany.

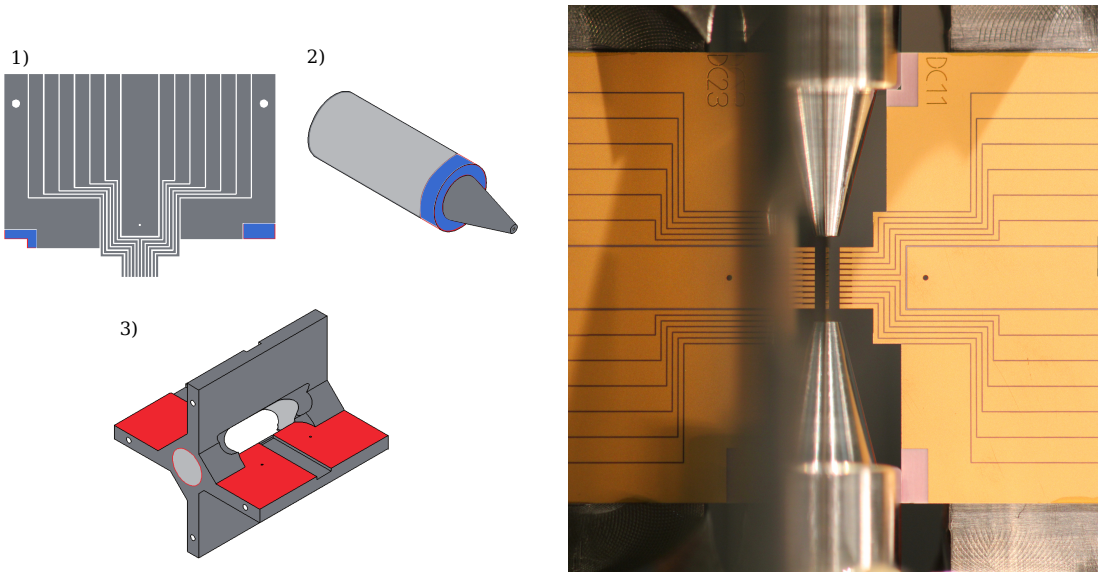

Figure 3.4.: Trap alignment and assembly. **a)** Functional principle of the trap alignment. The surfaces (red) of the titanium holder (3) supporting the electrode chips (1) have to be coplanar, and parallel to the borehole (light gray) of the endcaps (2). This borehole is performed uninterrupted in order to guarantee a coaxial alignment of both endcaps. The chips are aligned in two dimensions by the surfaces of the holder and the endcaps, whereas along the axial direction this is given by the edge of one endcap (blue). **b)** Photography of the chips aligned to the endcaps and glued to the titanium holder.

3.2. Implantation and microscopy infrastructure

This section is dedicated to the parts of the setup which apart from the source are crucial for ion microscopy and implantation. This comprises the deflection electrodes, the ion lens, the piezo translation stage and the ion detector.

3.2.1. Deflection electrodes

Manipulation of the beam direction can be used for two independent purposes: to align the beam to the experiment in order to correct for mechanical errors, or to scan the focussed beam in the focal plane. Conceptionally, this can be described by a simple transformation matrix, which in principle allows for changing position and angle of the beam independently. However, in a real experiment there are limitations, which prevent from applying those manipulations separately[11]. Placing deflection electrodes at a given position along the beam, between source and lens, act as a combination of changing the

[11] In principle, two pairs of spatially separated deflection electrodes, can provide for changing the position and the angle independently, but with a translation in between. In the experiment, this constellation was not considered to be necessary, because it would come at the expense of additional components, which not only would increase complexity, but also are likely to introduce additional electrical field noise. Since these problems are all technical, rather than physical, a future experiment could benefit from the flexibility gained by a pair of additional deflection electrodes.

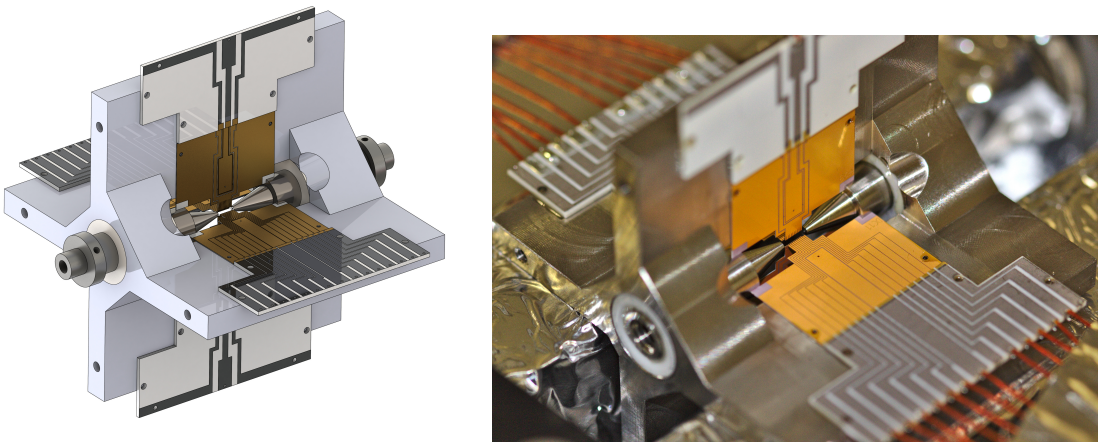

Figure 3.5.: Trap holder. **a)** Image of the trap on the titanium holder as rendered from CAD data. It shows the placement of the filter boards behind each electrode chip. **b)** Photography of the trap during assembly.

emission angle (when deflecting close to the source) and changing the incident angle of the lens (when deflecting at the lens). The first case can be used to align the beam to the centre of the electrostatic einzel lens *i.e.* correcting for a displacement between emission direction of the source and the lens-axis. The second case is shifting the source position virtually. This can be used to correct for a tilt of the lens or scanning its focus in the lateral position.

In the experiment at hand, the lens tilt is considered to be negligible, because scanning of the beam focus with respect to a sample is accomplished by moving the sample. Hence, a pair of deflection electrodes for each transversal direction, placed close to the source are sufficient to align the beam to the lens, while at the same time preventing the incident angle from changing too much (see also 4.3.1).

The setup features two separately placed pairs of deflection electrodes for the vertical x and horizontal y direction, located at a distance of 46.3 mm and 67.3 mm from the centre of the trap, respectively (compare Fig. 3.13). The individual electrodes are electrically supplied via coaxially shielded cables which are connected to a 4-pin vacuum feedtrough.

3.2.2. Electrostatic einzel lens

An electrostatic einzel lens is used for focussing of the ion beam. It is placed 338.4 mm[12] from the centre of the trap and is constructed from three rotationally symmetric electrodes, with an open aperture of 4 mm and a total length of 9.95 mm (see Fig. 3.6 a)). The two outer electrodes are grounded, whereas the electrode in the centre can be supplied with high voltage via a coaxially shielded copper cable which is connected to a high voltage vacuum feedthrough with a SHV plug on the atmosphere side. The geometry parame-

[12] The distance is measured to the end of the last electrode of the lens featuring a flat surface, which makes it suitable for a reference point.

ters of the lens, namely the thickness of the electrodes and the distance in between are optimised to minimise spherical aberration by electrostatic field simulations [Sin10]. This simulations also allowed to determine the principal plane of the lens, by intersecting parallel trajectories of the incoming ions with the convergent trajectories of the outgoing ions. With this method the distance of the principal plane to the end of the third electrode was determined to be 6.2 mm.

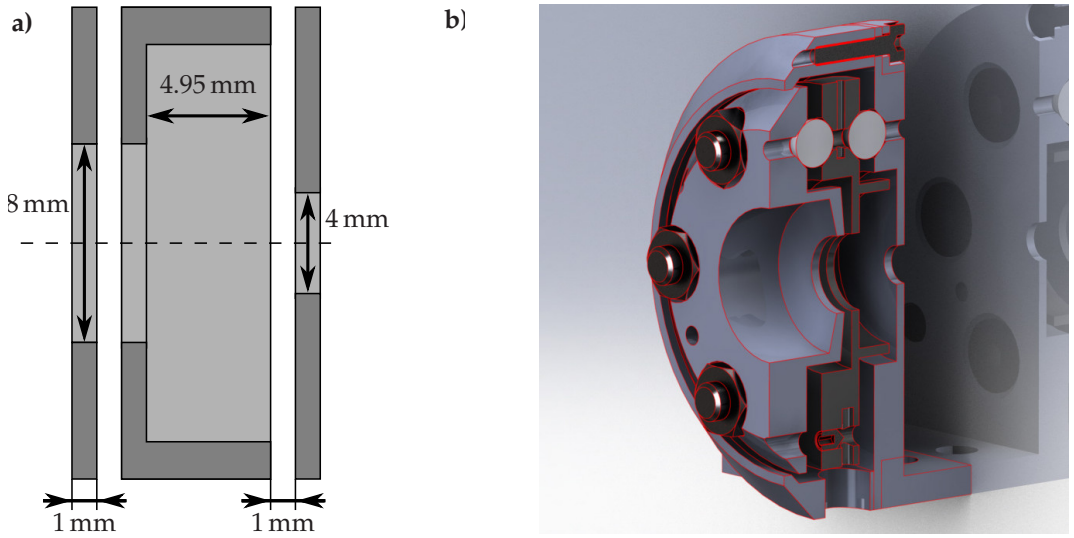

Figure 3.6.: Einzel lens. **a)** Important dimensions of the electrodes of the einzel lens. **b)** Cut through the three electrodes of the einzel lens along the symmetry axis. Starting with the third electrode, the assembly is performed on a lathe machine. The other electrodes are successively mounted with threaded rods (black), where they are insulated and aligned parallel with respect to each other by three ceramic spheres (white). With each mounting of an electrode, its aperture is finalised with the lathe, to ensure exact centring to the rotational symmetry axis. The outer electrodes (light gray) are grounded, whereas the centre electrode (dark gray) is supplied with a high voltage via a coaxially shielded cable, which is fixed with a grub screw at the bottom.

The mechanical design of the lens focuses on symmetry and shielding of non-conducting surfaces from the beam path [Moo09]. To this goal, the circular electrodes are stacked along their symmetry axis where each electrode is mounted by three support points given by ceramic spheres. The centre part of the electrodes is shifted along the symmetry axis to shield the ceramic mounting from the beam. A cut along the symmetry axis of the lens is shown in Fig. 3.6 b). A detailed design drawing can be found in Appendix B.

3.2.3. Piezo translation stage

The experiment is equipped with a three axis piezo translation stage[13] which is placed behind the lens. It allows one to move an experimentation platform with respect to the

[13] Positioner, *SLC-1720-S-UHV / SLC-24120-S-UHV*, SmarAct GmbH, Oldenburg, Germany.

beam (83 mm in x as well as 12 mm in y and in z direction). The positioners allow for an absolute positioning accuracy of ± 1 µm and scanning with a precision of down to ± 1 nm, depending on the step size. The platform comprises a holder for mounting the sample substrates used for microscopy or implantation and two profiling edges, one for each direction in the plane perpendicular to the beam.

3.2.4. Ion detection

For initial experiments, an on-axis electron multiplier tube (EMT) detector[14] was used, that is suitable for the detection of ions with energies of > 1 keV. This detector has a quantum efficiency of about 73 %. All experiments presented in this work, were performed using a different EMT detector with an off-axis design for energies below 1 kV[15]. To access higher energies the detector was tilted, effectively narrowing the entrance aperture, but yielding a detection efficiency of 96 %. The entrance aperture is located on the symmetry axis of the lens at a distance of 428 mm from the centre of the trap. The operating voltage typically is 2.8 kV. The detection signal is read out with a 4 GHz, 4-channel digital oscilloscope[16] which can be triggered to the ion extraction. Subsequently the recorded signal is forwarded to the experimental control computer where the detection events are automatically counted.

3.3. Electronic setup

In this section, all parts of the electronic infrastructure needed in order to operate the experiment as well as their interconnection are presented. A block diagram of the entire electronic setup is shown in Fig. 3.7.

3.3.1. Generation of static trapping voltages

The voltages for the DC electrodes and the deflection electrodes are provided by a dedicated low noise arbitrary waveform generator[17] which was developed in our group for the purpose of fast ion transport in segmented Paul traps [Zie12, Wal12]. The device is implemented as a rack mountable PCB-board featuring 12 channels. A block diagram of the entire device is shown in Fig. 3.8. Each channel is driven by an 16-bit digital to analog converter (DAC) featuring ± 10 V output voltage with a resolution of 0.3 mV. The device supports parallel operation of up to 4 of these boards, where all boards are controlled by a Field Programmable Gate Array (FPGA) providing the digital control signals for the DACs. The FPGA can be programmed by a personal computer via raw Ethernet protocol, allowing for the storage and execution of predefined voltage sequences. The experiment at hand uses two 12-channel boards, where one is used for supplying opposing pairs of DC electrodes and the other is driving the deflection electrodes. In addition, the voltages

[14] Electron multiplier tube AF150, *14150*, ETP electron multipliers, Ermington, NSW, Australia.
[15] Electron multiplier tube AF553, *14553*, ETP electron multipliers, Ermington, NSW, Australia.
[16] Agilent infiniium, *54832D MSO*, Agilent Technologies, Böblingen, Germany.
[17] DCSC-Analog Card, Op40 V5, Heinz Lenk.

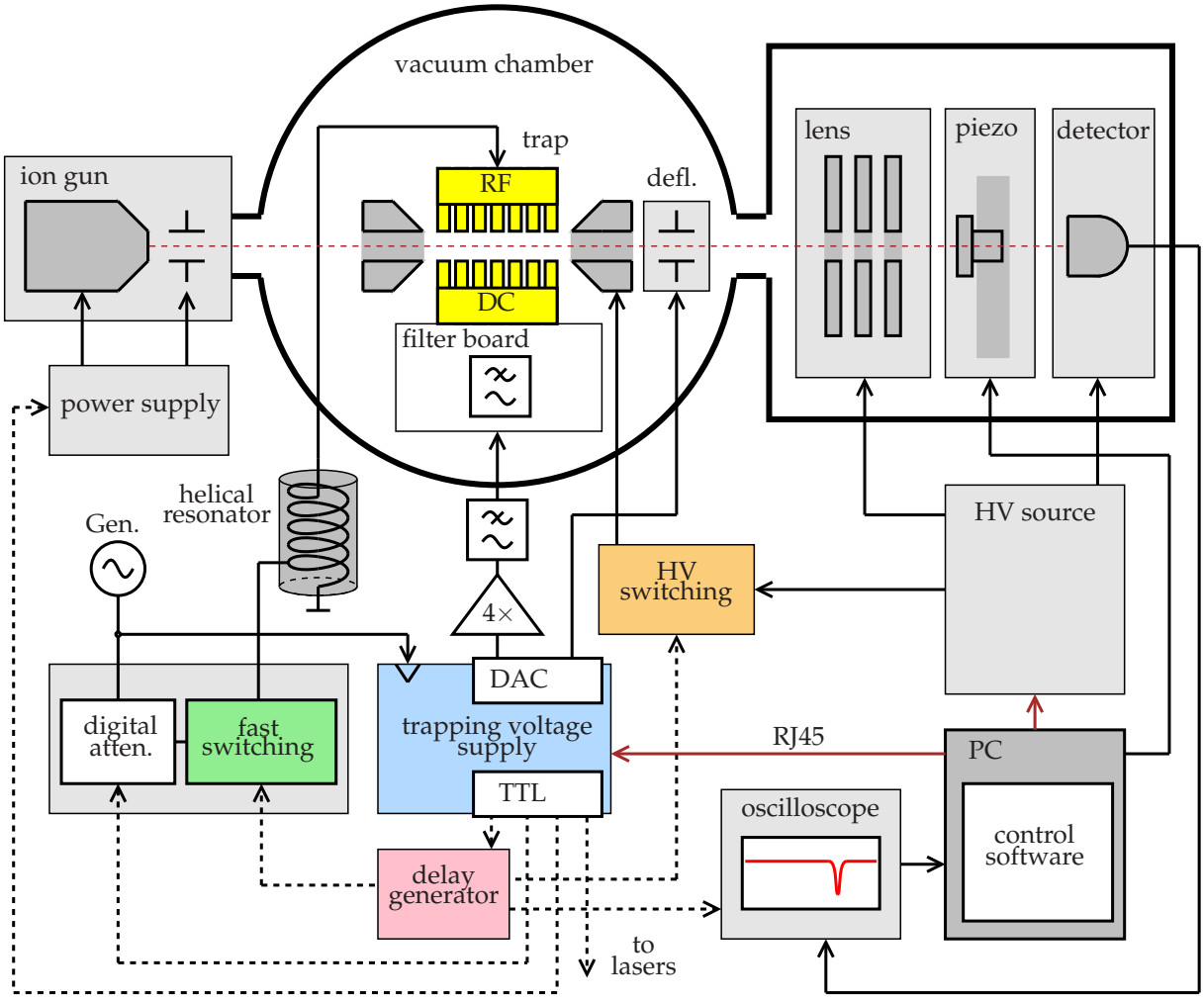

Figure 3.7.: Block diagram providing a synopsis of the electronic setup including important experimental components and the devices for their supply and control as well as the wiring.

for the trap are amplified to $\pm 40\,\mathrm{V}$, in order to permit higher axial trap frequencies. A CLC low-pass filter is placed between this amplifier and the vacuum feedthrough. To trigger and control other devices within a sequence, the FPGA features 28 TTL outputs. It also features two TTL input channels which can be used for time-depended triggering or realising conditional execution of sequences.

A mains and RF trigger allows for concurrently synchronising experiments to the $50\,\mathrm{Hz}$ of the power line and the signal of the radio frequency trap drive. It can be connected to one of the TTL input channels of the FPGA.

Typical voltages used for micromotion minimisation are in the order of $\left|U_{\mathrm{comp}}\right| < 150\,\mathrm{V}$, and are provided by a commercial high voltage supply[18].

[18] Bipolar 8-channel HV-module, *EB080-05105SHV*, ISEG Spezialelektronik GmbH, Rossendorf, Germany.

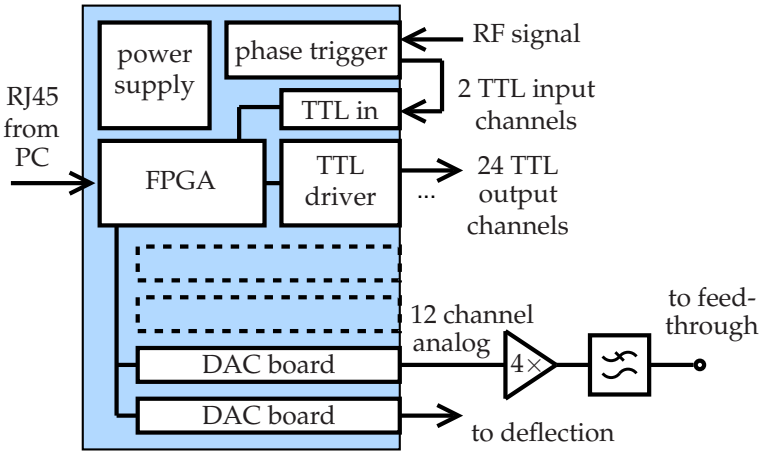

Figure 3.8.: block diagram of the supply for the static trapping voltages and TTL signals. The analog signals for the trap electrodes are amplified by a factor of 4 and filtered.

3.3.2. Radio frequency trapping voltages

A dedicated circuit is used to switch and attenuate the RF signal for the radial confinement of the ions (see Fig. 3.9). The signal at a frequency of around 23 MHz is produced by a

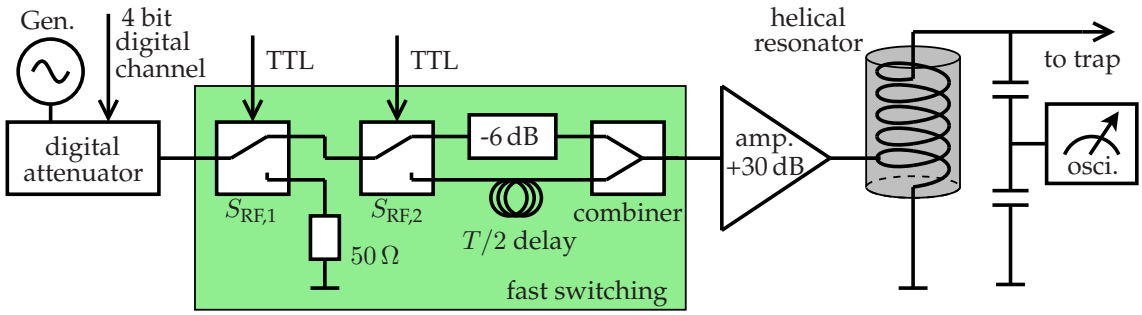

Figure 3.9.: Schematics of the circuit for the generation, attenuation, switching and amplification of the RF signal. A capacitive divider (right hand side) with 1:130 is used to measure and monitor the amplitude of the signal after the amplification.

signal generator[19]. Its amplitude can be controlled with a 4-bit digital attenuator in steps of 1 dB, allowing for adjusting the radial confinement of the trap. For fast switching off of the trap drive amplitude, the RF signal can be delayed by $T/2$ by virtue of a switchable delay line ($S_{RF,2}$). This leads to a superposition of the decaying original signal and the rising phase shifted signal, with destructive interference when both amplitudes reach the same value. At this point the signal is switched off completely ($S_{RF,1}$), leaving the amplitude at zero. Additionally, the amplitude of the phase shifted signal is 6 dB higher than the original to speed up the damping, as a result, achieving switching times in the order of 250 ns (compare 4.2.1).

[19] 80 kHz - 1040 MHz signal generator *2019A*, Marconi Instruments Ltd., London, United Kingdom.

Both, switching and attenuation are carried out at relatively low powers in the order of -3 dBm before increasing the power with an additional water cooled[20] 30 dB amplifier[21] to the required level.

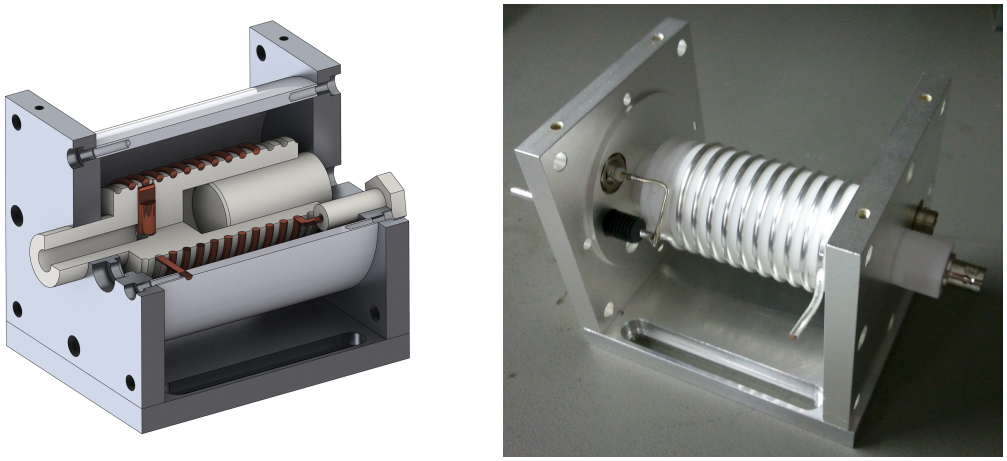

Figure 3.10.: Helical resonator. **a)** Cut through the helical resonator as rendered from CAD data. The supply of the RF signal is provided by a sliding contact pressing from inside the coil. Additionally, this allows for changing the tap point on the coil by turning the Teflon core (white). **b)** Photography of the helical resonator during assembly. The outer shielding is removed.

A helical resonator [Mac59] is employed, in order to match the 50 Ohm output impedance of the amplifier to the impedance of the trap and to reach the amplitudes necessary for radial trap frequencies of $1 - 3$ MHz. Compared to the common design used in the group, special emphasis is put on the stability of the output frequency and amplitude, rather than on a high quality factor. For this reason the shielding is closed by metal plates on both sides, lowering the quality factor but reducing the susceptibility to interference of the resonator field from outside. The coil is supported by a Teflon core, improving the mechanical stability. A helical groove on the surface of the core is guiding the coil and additionally allows for adjusting the tap point by turning the core. A cut of the resonator is shown in Fig. 3.10.

3.3.3. Electronics for ion extraction

Ions are extracted from the trap by applying a negative high voltage to one of the endcaps by means of a fast high voltage switch $S_{\text{ext},1}$[22] with rise time in the order of 100 ns and a jitter of less than 1 ns. When the ion is inside the endcap the voltage is switched back to zero, allowing the ion to leave the endcap on the other side. This voltage is limited to 3 kV to avoid flashover. The maximum energy can be increased up to the double value

[20] The water temperature is stabilised to ± 0.1 K.
[21] High power amplifier, *ZHL-5W-1*, Mini Circuits, Brooklyn, NY, USA.
[22] High voltage transistor switch, *HTS 151-03-GSM*, Behlke Power Electronics GmbH, Kronberg im Taunus, Germany.

by switching the extraction voltage to a positive value when the ion is in the endcap. For this configuration two high voltage switches connected in series are required. Because the switching has to be precisely timed, a pico second delay generator[23] is used to trigger the switching via TTL signal.

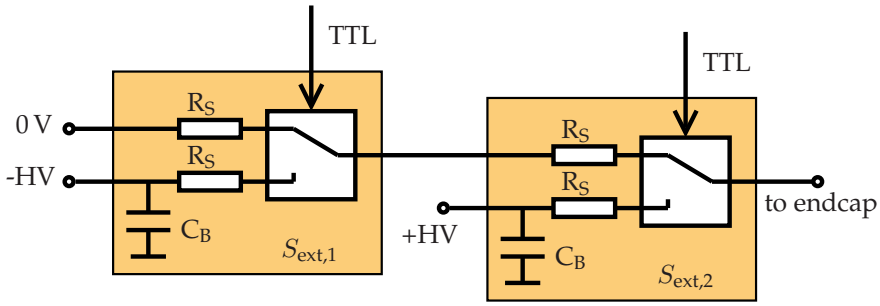

Figure 3.11.: Schematics of the circuit for switching the high voltages (HV) for the ion extraction. The HV is buffered with a $C_B = 100\,\text{nF}$ capacitor in order to attain fast rising times.

The radio frequency trap drive not only modulates the ion motion in radial, but also in axial direction (compare section 2.1.1). The reason for this are axial components of the RF field. Hence, this motion is referred to as axial micromotion. During extraction the ion approaches the endcap where the amplitude of the axial RF field is dramatically increased and as a result the kinetic energy of the ion is strongly modulated.

To reduce this influence, the radio frequency amplitude is switched off during extraction (compare 3.3.2). This switching is also triggered by the delay generator. Since this process is not instantaneous (about $250\,\text{ns}$) the modulation cannot be completely suppressed. Hence, the extraction process, including switching of the extraction voltage and switching of the RF drive, is triggered to the phase of the RF drive, ensuring the same field for each extraction event. The phase-triggering is accomplished with a device which was developed in our group specifically for this purpose[24]. Additionally, the extraction process is triggered to the phase of the mains to exclude potentially adverse influences from power line fields.

3.4. Vacuum setup

Ion trap experiments require a vacuum pressure of better than $10^{-9}\,\text{mbar}$ to reduce background gas collisions with the trapped ions. To access this regime the materials inside the vacuum vessel must have low outgasing rates and withstand temperatures of up to 200° C to permit baking the system over several days in order to evaporate residuals which are non volatile at room temperature. For this reason the vacuum chamber is made from stainless steel and high temperature compatible copper gaskets are used for the sealing of flanges. The vacuum system is located on an air-suspended optical table and is divided

[23] 4 channel digital delay generator, *DG535*, Stanford Research Systems Inc., Sunnyvale, CA, USA.
[24] RF-sync/delay, Op40 V2, Heinz Lenk.

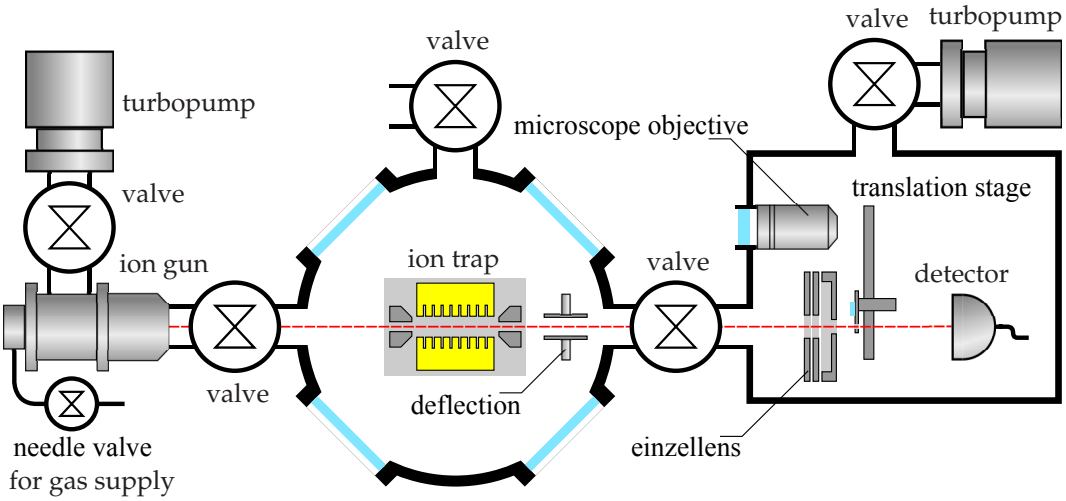

Figure 3.12.: Spatial arrangement of the vacuum chambers, valves and important experimental components within the vacuum. Gate valves enable to separate the volume of the trap chamber from the ion gun as well as from the detection chamber. The ion gun, the deflection and the focussing units are aligned to the trap axis (red dashed line).

into the trap chamber (3.4.1) containing the Paul trap (for details see3.1), *i.e.* the ion source, and the detection chamber (3.4.3) which is hosting sample substrates for microscopy or implantation, as well as an ion detector. The two chambers are separated by a gate valve[25] to be able to work on one chamber without breaking the vacuum of the other. Especially the detection chamber is frequently vented in order to exchange the samples. Fig. 3.12 depicts the spatial arrangement of the different chambers and the valves to separate them.

3.4.1. Trap chamber

The trap chamber is a commercially available non-magnetic stainless steel sphere[26] with an inner diameter of 165.1 mm (see Fig. 3.13). It features several access ports of different size, comprising a total of 6×DN63CF, 8×DN40CF and 12×DN16CF flanges. Optical access for the lasers and the imaging system is guaranteed by several replaceable fused silica windows[27] (5×DN63CF and 4×DN40CF) which are mounted to the access ports. They are anti reflection coated[28] at the wavelenghts 390 nm - 450 nm and 700 nm - 900 nm, for the purpose of out-coupling the laser light. Two of them are extended length viewports[29], where the window is mounted on a tube facing towards the inside of the chamber. This enables one to mount high numerical aperture optics close to the of the trap.

[25] All-metal gate valve, *48124-CE01*, VAT Deutschland GmbH, Grasbrunn, Germany.
[26] 4.50" Spherical Cube, *MCF450-SphCube-E6C8A12*, Kimball Physics Inc., Wilton, NH, USA.
[27] Fused Silica Zero Length Viewport, *HOVPZ64Q-LN*, *HOVPZ38Q-LN*, Hositrad Vacuum Technology, Hoevelaken, Netherlands.
[28] AR coating, *X/UIMCP4*, Hans Tafelmaier Dünnschicht-Technik GmbH, Rosenheim, Germany.
[29] Fused Silica Extended Length Viewport, *HOVPR64/32Q70WAR*, 70 mm length, inner diameter 47.5 mm, outer diameter 50.8 mm, Hositrad Vacuum Technology, Hoevelaken, Netherlands.

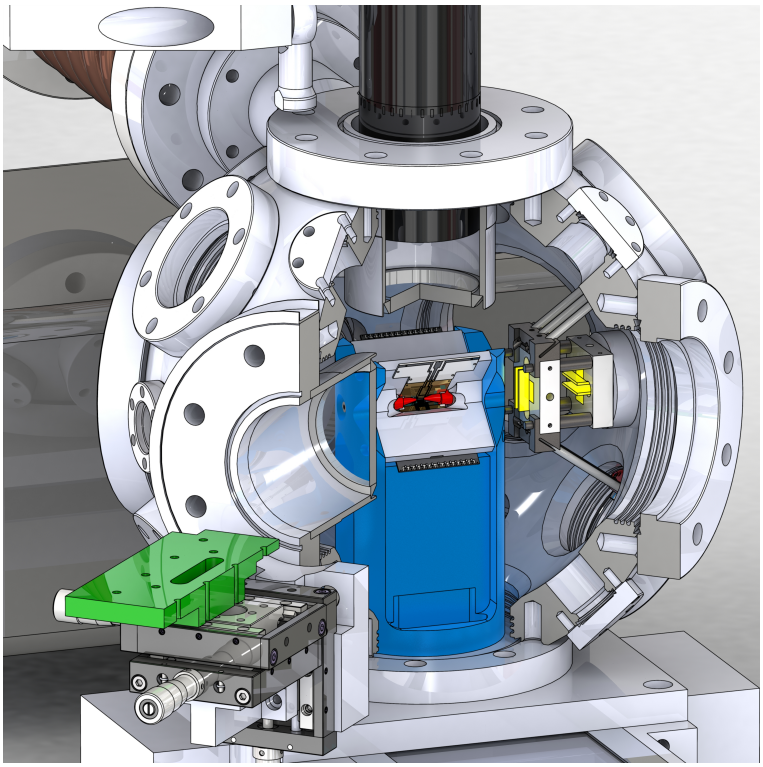

Figure 3.13.: Cut through the trap chamber with important parts being highlighted: The endcaps (red) as well as the deflection electrodes (yellow) are shown. The trap inside the holder is attached to the bottom flange via a special mount (blue). A platform for mounting optomechanics, is attached to one DN60CF flange via a three axis translation stage (green). The microscope objective for imaging ions is shown at the top (black). It is located inside a extended length viewport, allowing for higher numerical aperture.

The trap is located in the centre of the spherical vacuum chamber. It is mounted on the bottom flange by means of a holder which is designed to provide mechanical stability and optical access at the same time. The bottom flange is equipped with all electrical feedthroughs required for the operation of the trap. This comprises a 51-pin micro-D connector[30] supplying the segmented DC electrodes of the Paul trap, two 20 kV SHV-connectors[31] providing the feedthrough for the extraction voltage and an additional 8-pin feedthrough[32] for the trap drive as well as the oven which is mounted to the trap holder. In this way, the trap can be dismounted from the vacuum chamber without disconnecting the electrical supply cables. Special electrodes for beam deflection are connected via a separate

[30] 51-pin Micro D MIL-DTL 83513, *W-MDTL8-51-FM-CE-SSG*, VACOM Vakuum Komponenten & Messtechnik, Jena, Germany.
[31] SHVE Weldable coaxial feedthrough grounded, *9231001*, MDC Vacuum Ltd, Uckfield, United Kingdom.
[32] 8-pin current feedthrough, *W-HV1-8-CE-CU081*, VACOM Vakuum Komponenten & Messtechnik, Jena, Germany.

feedthrough[33] mounted on one of the DN16CF flanges, since they are not attached to the trap holder. An additional oven is placed on one of the DN16CF flanges[34] to reduce the heat influx and resulting thermal expansion thereby, compared to using the oven which is mounted on the trap holder.

The trap chamber is constantly pumped with a $34\,\mathrm{l/s}$ ion getter pump[35] as well as a titanium sublimation pump[36], both attached to separate DN40CF flanges. The titanium sublimation pump is water cooled by a secondary coolant circuit which is coupled to to the primary building coolant circuit via a heat exchanger[37] for the purpose of active temperature stabilisation ($\pm 0.1\,\mathrm{K}$). Typically the titanium sublimation pump is fired in periods of 8 hours. During periods of sensitive experimentation this pump is switched off to avoid fluctuations of the heat load. An additional valve[38] allows for connecting a turbo pump in order to pump the vessel from atmospheric pressure. The chambers base pressure is measured with a Bayard-Alpert type ionisation gauge[39]. Typically, the vacuum pressure is $5 \cdot 10^{-10}$ mbar.

3.4.2. Ion gun

A commercial ion gun[40] is used to load the Paul trap with ion species other than calcium. It is attached to the side of the vacuum chamber, such that the exiting beam is aligned with the axial direction of the trap (compare Fig. 3.12). It can ionise atoms from a wide range of gaseous sources using electron bombardment. From these ions it produces a collimated beam with a current up to $0.7\,\mu\mathrm{A}$ at an energy ranging from $500\,\mathrm{eV}$ to $5\,\mathrm{keV}$. A typical energy of $500\,\mathrm{eV}$ is used to load the Paul trap with nitrogen. The system is equipped with a Wien-type mass filter, to single out the desired ion species. Additionally, the ion gun provides a deflection unit which allows for scanning the beam by changing the deflection voltages. In the experiment this is used for precise alignment of the beam to the trap. It also enables the fast switching of the beam by changing between a voltage configuration where the beam is blanked and a configuration where it is coupled into the trap for a given period of time. This procedure has the advantage of being faster than switching of the extractor and as a result achieving much shorter exposure times.

3.4.3. Detection chamber

The detection chamber is a customised 5-way cross with $5\times$DN100CF flanges (for details see diploma thesis of S. Weidlich [Wei11]). It is constantly pumped by a $50\,\mathrm{l/s}$ ion getter

[33] 4-pin feedthrough, MIL-C-5015, *CF16-MPC5-4-SE-CE-AM*, VACOM Vakuum Komponenten & Messtechnik, Jena, Germany.
[34] 4-pin feedthrough, MIL-C-5015, *CF16-MPC5-4-SE-CE-AM*, VACOM Vakuum Komponenten & Messtechnik, Jena, Germany.
[35] VacIon Plus 40 StarCell, *9191240*, Agilent Technologies, Santa Clara, CA, USA.
[36] Titanium sublimation pump, *360043*, VACOM Vakuum Komponenten & Messtechnik, Jena, Germany.
[37] Heat exchanger, *WT 14-29565*, Deltatherm, Much, Germany.
[38] All-metal angle valve, *57132-GE02*, VAT Deutschland GmbH, Grasbrunn, Germany.
[39] Bayard-Alpert Gauge Tube, *UHV-24p*, Agilent Technologies, Santa Clara, CA, USA.
[40] Ion Source *IQE 12/38*, SPECS Surface Nano Analysis GmbH, Charlottenburg, Germany.

pump[41] and has its own pressure gauge[42]. For pumping the volume from atmospheric pressure, *e.g.* after changing microscopy or implantation samples, the chamber is equipped with a permanently mounted turbo molecular pump[43]. This pump can be separated from the vacuum of the detection chamber via an angle valve[44]. A DN100CF viewport is mounted on the top flange to allow for visual inspection and quick change of samples. An electrostatic einzel lens (see 3.2.2) together with a three axis piezo translation stage[45] is attached to a flange on the side of the chamber, also containing the voltage supply feedthroughs[46] [47] of both. A confocal microscope is realised by means of a microscope objective[48] mounted to the flange facing the trap chamber. A detailed characterisation of this microscope using NV colour centres can be found in the diploma thesis of S. Wolf [Wol12]. Originally this microscope was planed to be used to check for the conversion of nitrogen into NV colour centres after the implantation into a diamond substrate.[49] An ion detector[50] (see also 3.2.4) and the corresponding supply voltage feedthrough[51] are mounted to the back of the detection chamber on the axis of the einzel lens.

3.5. Optical setup

The optical setup consists of the imaging system (section 3.5.2) and the laser setup (section 3.5.1) comprising the infrastructure to stabilise, modulate, guide, polarise and focus the laser light to the ion trap.

3.5.1. Laser system

In total 6 different laser sources are necessary for the experiments of this work, each with different requirements regarding wavelength, stability and power of the emitted light. These requirements directly result from the application of driving different transitions of the calcium atom and ion. Given the required wavelengths, diode lasers with powers of $\leq 100\,\mathrm{mW}$ are sufficient to obtain intensities saturating the transitions while illuminating the whole Coulomb crystal. In order to drive the dipole allowed transitions, stabilities of better than $1\,\mathrm{MHz}$ are adequate, whereas coherent state manipulation on the quadrupole

[41] VacIon Plus 55 StarCell, *9191255*, Agilent Technologies, Santa Clara, CA, USA.
[42] Bayard-Alpert Gauge Tube, *UHV-24p*, Agilent Technologies, Santa Clara, CA, USA.
[43] Turbovak TW70, *800002V2236*, Oerlikon Leybold Vacuum, Bonn, Germany.
[44] All-metal angle valve, *57036-GE02*, VAT Deutschland GmbH, Grasbrunn, Germany.
[45] Positioner, *SLC-1720-S-UHV / SLC-24120-S-UHV*, SmarAct GmbH, Oldenburg, Germany.
[46] Lemo UHV feedthrough, *ALB-VF-SJG-CON-UHVT-42*, SmarAct GmbH, Oldenburg, Germany.
[47] Coaxial-SHV 5 KV feedthrough, *8630-02-W*, Hositrad Vacuum Technology, Hoevelaken, Netherlands.
[48] Plan Achromat, MPLAPO50X/0.95 UIS-OBJ,AA0.30, *037653*, Olympus Deutschland GmbH, Hamburg, Germany.
[49] This would enable to repeat the implantation at sites where this conversion failed, and in this way generate patterns of NV centres independent of the notoriously low conversion efficiency. However, this plan also necessitates the annealing to $800\,^{\circ}\mathrm{C}$ of the diamond sample as an intermediate step, which is difficult to reconcile with the piezo translation stage in use. For this reason the plan is put on hold for now.
[50] Electron multiplier tube AF553, *14553*, ETP electron multipliers, Ermington, NSW, Australia.
[51] Coaxial-SHV 5 KV feedthrough, *8630-02-W*, Hositrad Vacuum Technology, Hoevelaken, Netherlands.

transition requires a stability of at least 1 KHz. All lasers are located on a separate air-suspended optical table. Therefore, optical fibers are used to guide the light to the table hosting the vacuum setup with the trap. The wavelengths of all lasers are constantly measured with a wavelength meter[52], for the purpose of monitoring and coarse tuning.

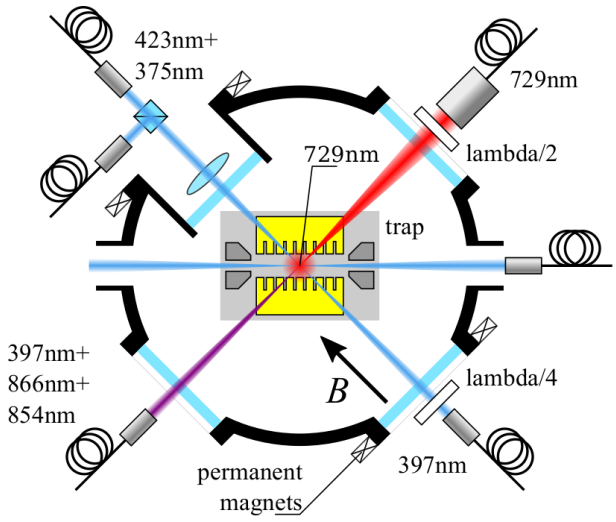

Figure 3.14.: Orientation of the different laser beams and the magnetic field with respect to the trap, as viewed from the top. The ionisation beams (top left) at 375 nm and 423 nm are superimposed with a PBS and focussed inside an extended viewport in order to permit a high numerical aperture. The second stage cooling laser as well as the 866 nm and the 854 nm lasers are supplied superimposed with a photonic fiber (bottom left). All three beams are focussed by an achromatic lens. The σ-polarised beam is aligned parallel to the magnetic field (bottom right). The beams for first stage Doppler cooling with high power and micromotion minimisation enter the trap from below under an angle of $\pi/4$ with respect to the trap axis (right side). The 729 nm beam enters either from the side, focussed with micro-focus optics inside the collimator (top right) or from the top, focussed by means of the imaging objective (center). The first configuration allows to address all modes, whereas the second one solely addresses the radial modes.

Lasers for photoionisation

There are two lasers used for the resonance-enhanced multiphoton ionisation of calcium, at wavelengths of 422.79245 nm and at about 375 nm. The laser close to 423 nm is a commercially available grating stabilised external cavity diode laser[53]. It is used to excite the calcium atom from the 4^1S_0 groundstate to the 4^1P_1 intermediate level. This transition is Doppler broadened to around 100 MHz, since the neutral atoms leave the oven with a thermal velocity distribution. In addition, its frequency is 50 MHz Doppler shifted to

[52] Wavelength meter *HF-ANGSTROM WS/U-30U*, in combination with an 8 channel opto-mechanical switch, HighFinesse GmbH, Tübingen, Germany.
[53] DL 100 pro, TOPTICA Photonics AG, Gräfelfing, Germany.

the red, due to the angle of $135\,^\circ$ of the ionisation laser with respect to the direction of the atom beam. From the 4^1P_1 level, the second laser, a free running diode at $375\,\mathrm{nm}$, ionises the atom. Both lasers are controlled with mechanical shutters [Sin02]. The light is guided to the trap by optical fibers and superimposed with a polarising beam splitter (PBS). Subsequently, both beams are focussed to about $50\,\mu\mathrm{m}$ in the trap centre with an achromatic lens, at powers of $2\,\mathrm{mW}$ and $3\,\mathrm{mW}$ of the $423\,\mathrm{nm}$ and the $375\,\mathrm{nm}$ light, respectively.

Laser for Doppler cooling, state detection and state initialisation

The dipole allowed $4^2S_{1/2}$ to $4^2P_{1/2}$ transition (compare 2.2.2) is used for Doppler cooling (2.2.3), state initialisation (2.2.4) and state detection (2.2.5). For effective Doppler cooling, the laser linewidth has to be small compared to the natural linewidth of the transition which is $\Gamma/2 \approx 2\pi \cdot 10\,\mathrm{MHz}$. To meet this requirement a grating stabilised external cavity laser in Littrov configuration, running at $396.95950\,\mathrm{nm}$ is used[54], and which in addition is actively stabilised to a low finesse reference cavity with the Pound-Drever-Hall method [Dre83, Fox03]. The output light with a power of about $20\,\mathrm{mW}$ is split into several beams, each with a different purpose (compare Fig. 3.15). For fast Doppler cooling a scheme is used which works in two steps: an initial coarse but fast cooling stage with high power and a second low-power Doppler cooling stage for achieving low temperatures. For the first step, the light is red-detuned by $400\,\mathrm{MHz}$ from the resonance of the cooling transition[55] at a power of $2\,\mathrm{mW}$. This beam is switched by a mechanical shutter and carried to the trap by a single mode polarisation maintaining fiber. It enters the trap chamber from below at an angle of 45° with respect to the axial direction of the trap. The focus in the centre of the trap has a size of about $50\,\mu\mathrm{m}$.

There are two other branches, both controlled by acousto-optic modulators (AOMs) in double pass configuration[56]. The RF signal to drive the AOMs is provided by custom designed driver circuits[57]. This allows for fast TTL controlled switching and adjustment of the intensity of the laser light by means of a control voltage. The rise and fall times of all AOMs are measured to be in the order of $500\,\mathrm{ns}$.

One of these branches is used for the second stage Doppler cooling and micromotion minimisation (4.1.2), having a power of $15\,\mu\mathrm{W}$. This beam is supplied to the trap via a single mode photonic crystal fiber[58] and focussed by a fiber collimator[59] in combination with a special lens [60] to a size of $50\,\mu\mathrm{m}$. The k-vector has an angle of $\Theta = (\pi/4, \pi/3, \pi/3)$ with respect to the principal axes of the trap to cool the ion in all spacial directions. The light is p-polarised with respect to the magnetic field. This allows for driving π-transitions

[54] DL 100, TOPTICA Photonics AG, Gräfelfing, Germany.
[55] The laser runs red detuned by $400\,\mathrm{MHz}$ and the beams which have a frequency close to the resonance are shifted to the blue by AOMs.
[56] BRI-QFZ-177-20-397, Brimrose, Sparks, MD, USA.
[57] AOM-Driver, Op5 V6, Heinz Lenk.
[58] LMA-PM-5, *K50-010-52*, NKT Photonics, Birkerød, Denmark.
[59] Fiber collimator, *60FC-T-4-M40-124*, Schäfter + Kirchhoff GmbH, Hamburg, Germany.
[60] Micro-Focus Optics, *13M-M125-13*, Schäfter + Kirchhoff GmbH, Hamburg, Germany.

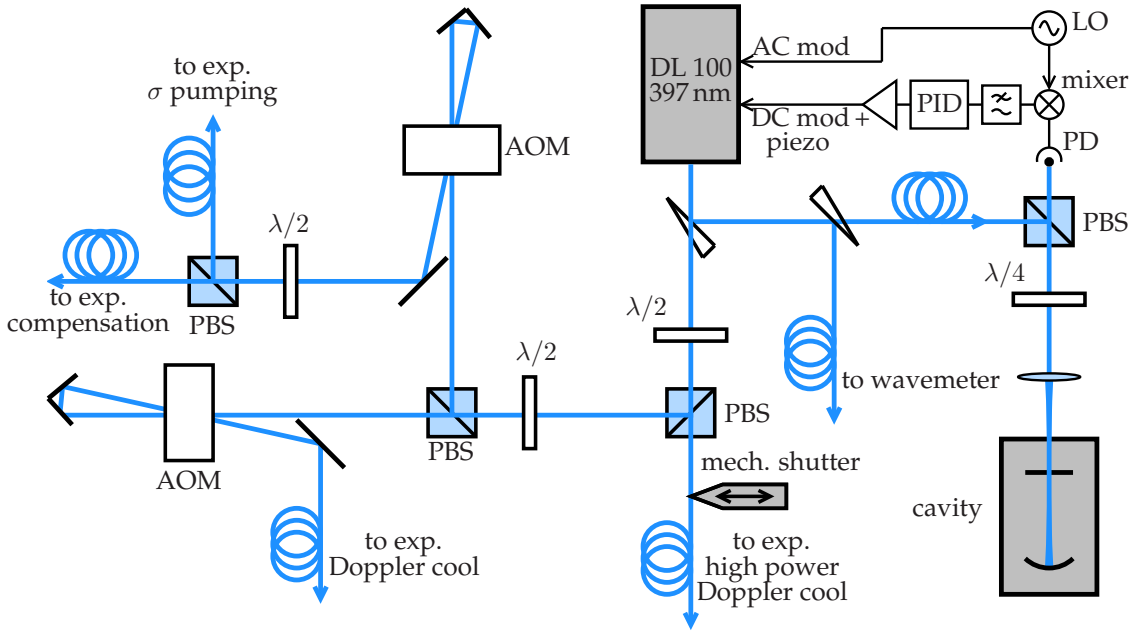

Figure 3.15.: Scheme of the 397 nm laser system, used for Doppler cooling, state detection and state initialisation. A small fraction of the light is used to monitor the absolute wavelength with a wavemeter and for stabilising the laser to a low finesse cavity by means of the PDH method (right hand side). About half of the power is used for initial cooling of the ion. The other half of the power is distributed among two branches, one for second stage Doppler cooling, the other for micromotion minimisation and state initialisation by σ-pumping. Both branches are switched with AOMs in double pass configuration.

of both Zeeman sublevels simultaneously which in first order have the same frequency.

The branch controlled by the second AOM is used for micromotion minimisation (4.1.2) and optical pumping (2.2.4) on the $4^2S_{1/2}$ to $4^2P_{1/2}$ transition by using σ-polarised light. Since these two applications are never used simultaneously, one of them can be selected by switching the light with a PBS. The light for micromotion minimisation enters the trap over the same path as the high power first stage cooling beam, while also having the same polarisation and intensity as the second stage cooling beam. The σ-polarised light for state initialisation is supplied via a dedicated single mode polarisation maintaining fiber, where the polarisation is adjusted with a $\lambda/4$ wave plate, located directly in front of the vacuum viewport.

Lasers for repumping and quenching

The metastable D levels can be depopulated by optically pumping the population to the short lived P levels. This technique is applied for the purpose of recovering the population from the D-levels to the cooling cycle when performing Doppler cooling, and hence is also termed repumping. Another application is the quenching the D-level population

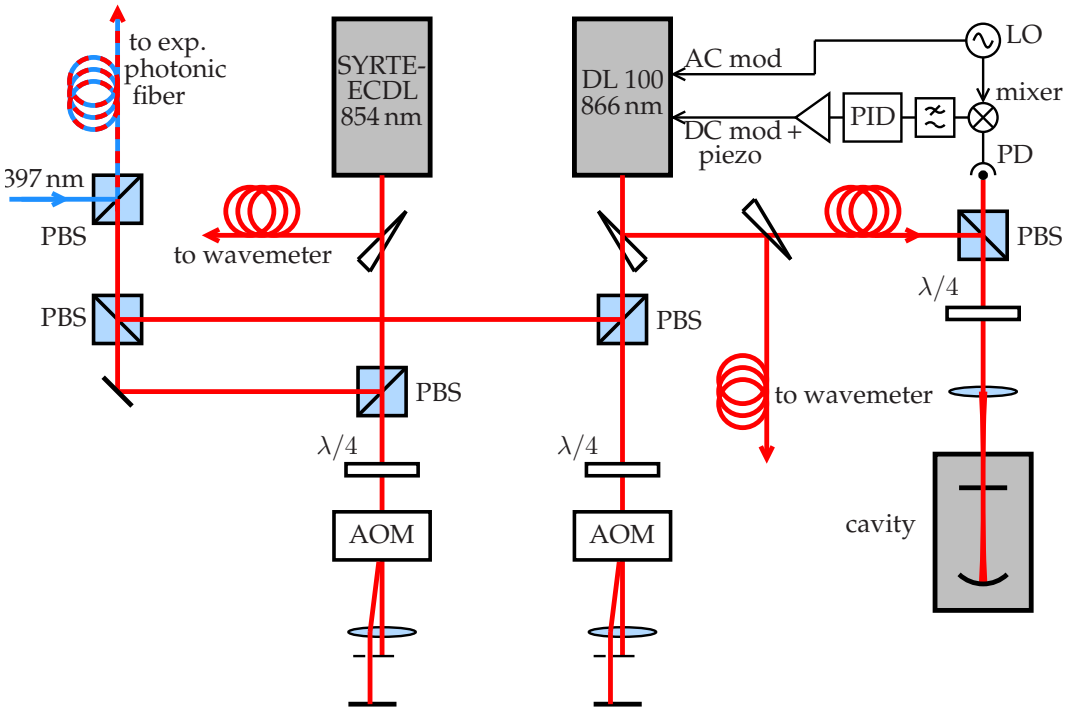

Figure 3.16.: Scheme of the laser setup for repumping and quenching. A small fraction of the light is splitt off right after the lasers to monitor the frequency of the light via the wavemeter. Both lasers can be switched with AOMs in double pass configuration. The repumping laser at 866 nm needs to be stabilised with the PDH method. The beams are superimposed with the light from the second stage Doppler cooling branch, and are coupled into a polarisation maintaining single mode photonic fiber.

in the context of coherent manipulations on the $4^2S_{1/2}$ to $3^2D_{5/2}$ transition. Repumping and quenching concerns two transitions, namely the $3^2D_{3/2}$ to $4^2P_{1/2}$ at 866 nm and the $3^2D_{5/2}$ to $4^2P_{3/2}$ at 854 nm (see also 2.2.2). For each transition a separate external cavity diode laser is used (compare Fig. 3.16), where the former is a commercial laser[61], which additionally is stabilised with the PDH locking technique to run at 866.45090 nm. The latter is a self build external cavity stabilised laser, whose wavelength can be selected with an interference filter [Zor88, Bai06, Gil07] and typically is running at 854.44362 nm. Both lasers can be switched with AOMs[62] in double pass configuration. The AOMs are controlled by similar driving circuits as those used for the blue light (see section 3.5.1). The beams are superimposed with the second stage cooling laser by means of a dichroic mirror in order to couple them into the same photonic crystal fiber. Subsequently all three beams are focussed with an achromatic fiber collimator[63] to a size of about 50 µm (compare 3.5.1). The repumping beams are s-polarised, such that they are simultaneously driving σ^+ and σ^- transitions in order to efficiently depopulate the D-states.

[61] DL 100, TOPTICA Photonics AG, Gräfelfing, Germany.
[62] BRI-TEM-85-2-729, Brimrose, Sparks, MD, USA.
[63] Fiber collimator, *60FC-T-4-M40-124*, Schäfter + Kirchhoff GmbH, Hamburg, Germany.

Laser for coherent state manipulation

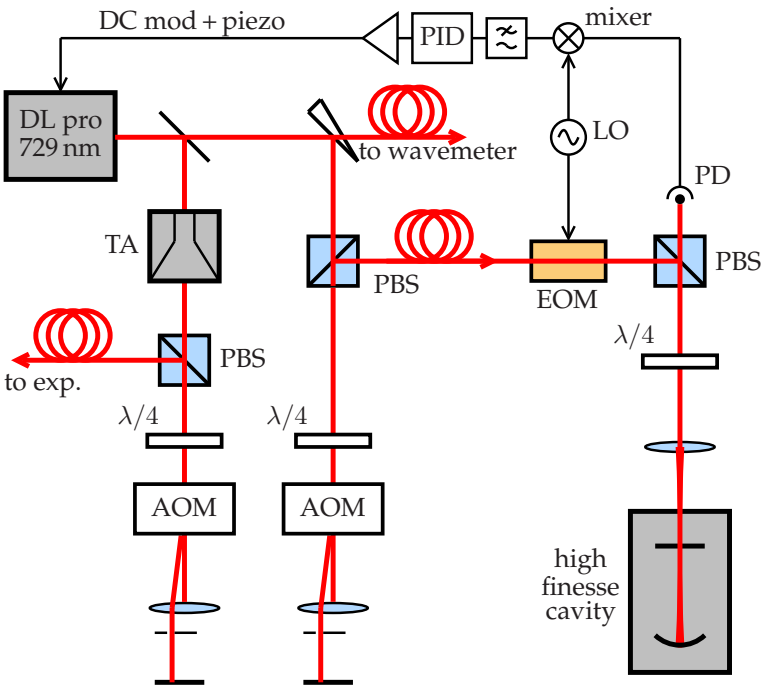

Figure 3.17.: Scheme of the laser setup for coherent state manipulation. The part of the light which is used for PDH stabilisation is split off prior to amplification with a tapered amplifier (TA) in order to avoid additional noise introduced by the TA. An AOM is used to match the closest mode of the cavity, followed by a phase modulation with an EOM. The amplified light is modulated in amplitude, frequency and phase with another AOM in double pass configuration, before it is coupled into a polarisation maintaining single mode fiber, leading to the experiment.

The laser system used for coherent manipulation of the $4^2S_{1/2}$ to $3^2D_{5/2}$ transition at 729 nm, is a grating stabilised external cavity diode laser in combination with a tapered amplifier[64] (TA) reaching an output power of up to 200 mW. It is actively stabilised to run at 729.34817 nm with a stability of $\Delta\nu = 10.4 \pm 4.5$ Hz [Deg13], by PDH-locking it to a resonator mode of a temperature stabilised high finesse cavity[65]. To this goal, an AOM[66] in double pass configuration is used to tune a small fraction of the light from the laser which is running at the transition frequency, to match the closest cavity mode (see Fig. 3.17). The phase modulation of the light, required for the PDH stabilisation, is provided by an electro optical modulator (EOM). In contrast to modulating via the diode current, this method has the advantage of a more linear response and in addition avoids to generate sidebands on the light which is sent to the ion. The technical details about the PDH stabilisation of the 729 nm laser can be found in the diploma thesis of C. Degünter [Deg13].

[64] TA pro, TOPTICA Photonics AG, Gräfelfing, Germany.
[65] Reference cavity assembly, *ATF-6030*, ADVANCED THIN FILMS, Boulder, CO, USA.
[66] BRI-TEM-200-50-729, Brimrose, Sparks, MD, USA.

Addressing and state manipulation of resolved carrier and sideband transitions requires pulsing with different amplitude, frequency and phase in fast succession. This is realised by another AOM[67] in double pass configuration, which is driven by a specialised arbitrary waveform generator[68]. Radio frequency pulse sequences of arbitrary shape, frequency and phase are prestored in an internal memory and can be triggered by a TTL signal.

The modulated light is supplied to the trap via a polarisation maintaining single mode fiber. The experimental setup allows for switching between two different beam orientations: The first configuration has an incident angle of $\Theta = (\pi/4,\pi/3,\pi/3)$ with respect to the principal axes of the trap. Consequently, it has a projection on all of these axes, addressing all vibrational modes accordingly. This beam enters the chamber from one of the DN60CF-flanges and is focussed by a fiber collimator[69] to $50\,\mu m$. The second configuration has an angle of $\Theta = (\pi/2,\pi/4,\pi/4)$ and is realised by coupling the beam into the microscope objective of the imaging system (3.5.2) by means of a dichroic mirror. This allows for harnessing the high numerical aperture of the objective for focussing, and in this way to realise a focal size of $5\,\mu m$[70]. Since this beam has no projection on the axial direction of the trap it only couples to the radial modes of vibration. Therefore, this configuration is used for sideband cooling and evaluation of the temperature exclusively in the radial plane. Both beams are linearly polarised, and in each case the orientation can be adjusted with a $\lambda/2$ wave plate.

3.5.2. Imaging system

The ion fluorescence at $397\,nm$ is imaged for the purpose of spatial localisation and state detection. The former requires the spatial resolution and the mechanical stability to be high enough to resolve single ions in a coulomb crystal. The latter demands a detection with a high quantum efficiency in order to rapidly discriminate between a fluorescent and a dark state (see 2.2.5). To meet these requirements, the imaging system combines a microscope objective[71] with high numerical aperture and an electron multiplied charged coupled device (EMCCD) camera[72] which has a fast readout (max. $10\,MHz$) and is optimised for UV light. The ions are imaged from the top of the vacuum vessel. A short object distance is enabled by using an extended length viewport and in this way permitting a high numerical aperture. The objective has focal length of $f = 66.8\,mm$ with an open aperture of $D = 38\,mm$ resulting in a numerical aperture of $NA = 0.27$ [Mai06]. In total it consists of 5 lenses which are anti-reflection coated for light at $397\,nm$ and $729\,nm$. To minimise the construction height a deflection mirror is used to redirect the optical path in horizontal direction. All elements of the imaging system are mounted on a movable aluminium profile, which allows for shifting the objective with respect to the trap to choose the focus and the imaging area. At the side facing the vacuum chamber, the stage

[67] BRI-TEF-80-20-729, Brimrose, Sparks, MD, USA.
[68] VFG-150, TOPTICA Photonics AG, Gräfelfing, Germany.
[69] Fiber collimator, *60FC-T-4-M60-124*, Schäfter + Kirchhoff GmbH, Hamburg, Germany.
[70] As per the typical inter ion distance is about $10\,\mu m$, this allows for single ion addressing.
[71] Sill Optics GmbH, Wendelstein, Germany.
[72] Andor iXon X3 *DU-860E-CS0-UVB*, Andor Technology, Belfast, Northern Ireland.

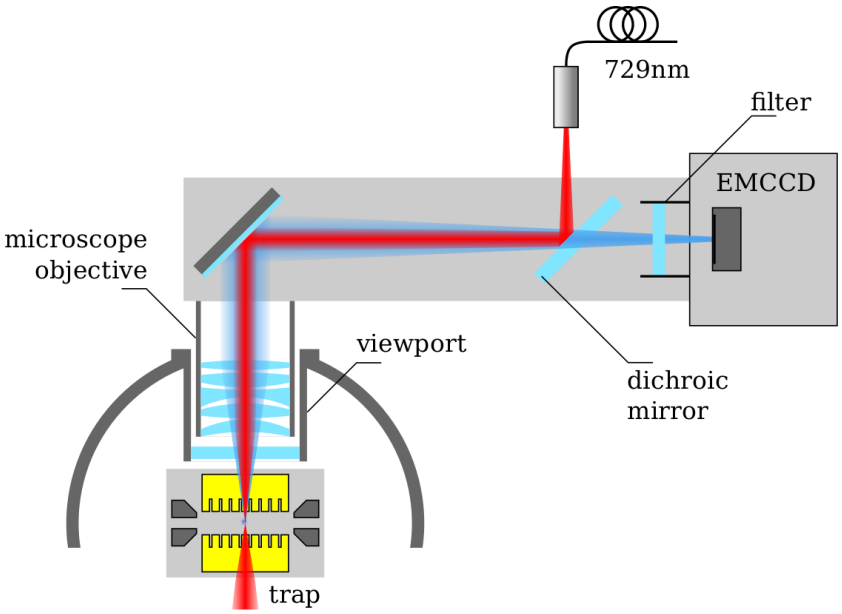

Figure 3.18.: Optical path of the imaging system as seen from the side. An extended length viewport permits to closely approach the trap with the microscope objective and in this way realising a high numerical aperture. The 729 nm beam is superimposed to the optical path by a dichroic mirror. In this way the objective can be used for imaging of the ions on the EMCCD and at the same time act as a focussing lens for the 729 nm beam. A bandpass filter is placed in front of the EMCCD to suppress background and stray light.

is supported in a ball joint. The position can be adjusted with a three axis stage which can be translated with micrometer screws[73]. At the the other end, the construction is mounted to the optical table with a combination of a linear slider[74], a rotation mount[75], and a rocker to provide the necessary degrees of freedom. The image distance can be adjusted by changing the length of the aluminium profile. For all experiments reported here, this length is 1.05 m resulting in a magnification of 15. The optical path to the camera is surrounded by a PVC-tube to shield the sensor from stray light. In addition, a narrow bandpass filter[76] around 394 nm is placed in the optical path to suppress background light. The image sensor of the camera, has a resolution of 128×128 pixel, and a pixel size of $24 \times 24\,\mu$m. Given the aforementioned magnification, this allows for imaging an area of about $220 \times 220\,\mu$m.

The objective lens can also be used for radial addressing the ions with 729 nm light (see also 3.5.1). With this configuration, the high numerical aperture of the objective allows

[73] Translation Stage PT1, *150-801ME*, Thorlabs, Newton, NJ, USA.
[74] Ball-Bearing Guide Bush Set 8 160x40 D14, *0.0.386.10* item Industrietechnik GmbH, Solingen, Germany.
[75] Rotation Platform, *RP01/M*, Thorlabs, Newton, NJ, USA.
[76] Bandpass Filter, 394nm CWL, 25mm Dia., Hard Coated OD 4 10nm, *65131*, Edmund Optics GmbH Deutschland, Karlsruhe, Germany.

for a focus, small enough to address single ions in a coulomb crystal. A dichroic mirror[77], which is reflective at 729 nm, and anti reflection coated for the fluorescence light at 397 nm, is used to couple the light into the optical path of the imaging system. It is is placed between objective and camera at an angle of $45°$. The fiber coupler for the 729 nm light is mounted to the aluminium profile by means of an optical bench, which is oriented perpendicular to the optical path of the imaging system. The polarisation of the light is linear and can be adjusted with a $\lambda/2$ wave plate.

[77] Out-coupler, *HR729/45°&HT397/45°*, LENS-Optics GmbH, Allershausen, Germany.

4. Characterisation and preliminary experiments

The scope of this chapter are different preparatory measures and characterisation experiments which are necessary in order to conduct and evaluate the final microscopy and implantation experiments discussed in chapter 5 and 6 of this work. Among these are:

- characterisation experiments
  - to assess if necessary requirements are met, *e.g.* critical parameters are within a required range.
  - to obtain parameter values, which are necessary for data evaluation of subsequent experiments.
- preparatory and alignment measurements to adjust parameters values for subsequent experiments.
- standard procedures which are a crucial part of a more complex experiment and therefore are discussed and evaluated separately.

While many of these experiments employ techniques adopted from fields such as ion trapping, quantum optics and accelerator physics, some methods regarding loading of the trap and ion extraction are new inventions and are therefore discussed in more detail. This chapter is roughly structured along the experimental succession: The first two sections, namely 4.1 *Trap operation* and 4.2 *Ion extraction: Implementation of the single ion source* address measurements and experiments pertaining ion trapping, ion extraction and beam characterisation, whereas section 4.3 *Ion lens operation* discusses the focussing of the beam and the measurement of the focal properties.

4.1. Trap operation

This section is dedicated to the automatic trapping of ions, as well as the related characterisation and preparatory measurements. All the operating procedures described in this section are standard methods also used in similar Paul trap experiments. While some of them only have to function reliably such as the micromotion minimisation or the sidband spectroscopy, others have special requirements concerning the characteristics of this experiment and for this reason have to be modified in order to match these demands. This applies for example to the ionisation and loading of the trap, as it has to be as fast as possible, because this limits the repetition rate of the experiment.

In 4.1.1 *Automatic trapping and cooling procedure*, the steps necessary to automatically prepare trapped cold single ions with a high repetition rate are described and evaluated. Section 4.1.2 *Micromotion minimisation*, explains the compensation of stray fields and mechanical imperfections of the trap by applying respective fields in order to guarantee optimal conditions for laser cooling and ion extraction. In 4.1.3 *Resolved sideband spectroscopy*, the temperature of an ion after Doppler cooling as well as after sideband cooling, is evaluated. This allows for calculating the size of the wave packet, which later will be compared to results from focus measurements.

4.1.1. Automatic trapping and cooling procedure

Trapping and cooling of the ions is automatised in order to make it fast and reliable. The entire procedure consists of ionisation, trapping and initial Doppler cooling of ions, followed by reducing the number of ions to a predefined value as well as a second cooling stage with reduced laser power. The physical details are described in the remainder of this section and a flowchart of the technical implementation is shown in Fig. 4.1.

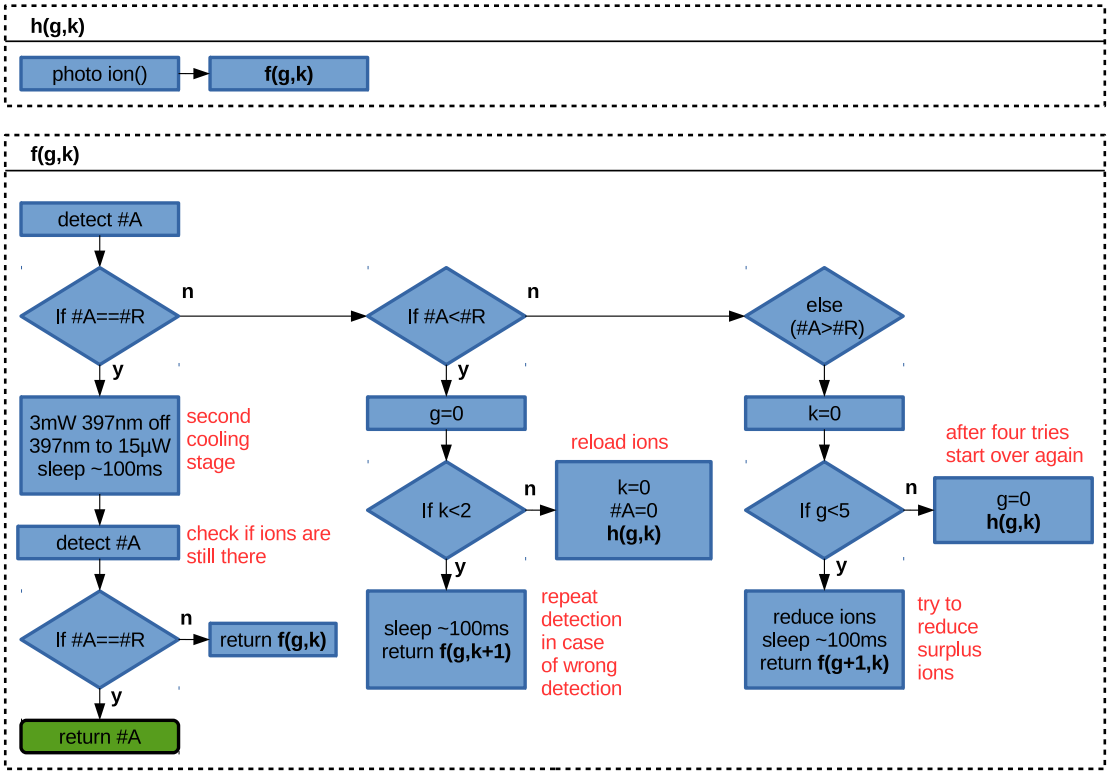

Figure 4.1.: Flowchart of the automatic trapping and cooling procedure, showing the most important steps. #*A* is the number of detected ions, #*R* is the amount of requested ions, *g* is the number of cases were #*A* was bigger than #*R* and *k* is the number of cases where #*A* was smaller than #*R*. The red annotations serve to clarify particular steps.

Photoionisation

For the ionisation of ^{40}Ca, resonance-enhanced multiphoton ionisation (REMPI) is used. In contrast to regular photoionisation, where an electron is exited above the ionisation threshold by absorption of a single photon, this process involves at least one interim step, which excites the atom to an intermediate state first. From this state it is finally ionised by a second excitation. This offers the advantages of being isotope selective and in addition allows for using longer wavelengths for the transitions which are therefore easier to be matched by diode lasers (see section 3.5.1). For the cascade used here, the atom is first excited with a laser at $423\,\mathrm{nm}$ to the 4^1P_1 level and then subsequently ionised by laser light at $375\,\mathrm{nm}$. Ions generated within the trapping potential (compare 2.1.1) at sufficiently low speeds are confined in the trap. A typical loading rate in the order of 10 ions per second is obtained in the experiment, depending on the oven current and intensity of the lasers.

Doppler cooling

In the present work, Doppler cooling (compare 2.2.3) is a critical part of all experiments involving ion extraction. It has to yield low temperatures, required to achieve favourable beam properties, while at the same time being fast, in order to increase the repetition rate of the experimental cycle. To meet both requirements, a dedicated sequence comprising switching of laser powers and trap frequencies is applied. After trapping, the ions are Doppler cooled on the $4^2S_{1/2}$ to $4^2P_{1/2}$ dipole transition near $397\,\mathrm{nm}$. The respective cooling laser is red-detuned by about $2\pi \cdot 15\,\mathrm{MHz}$ at a power of $50\,\mu\mathrm{W}$. To make this process faster, a $400\,\mathrm{MHz}$ red-detuned laser with a power of $3\,\mathrm{mW}$ is superimposed to the normal cooling beam. Both lasers have a focal radius in the order of $50\,\mu\mathrm{m}$ (see also 3.5.1). In addition, the trap frequencies are reduced by lowering the radio frequency supply voltage of the trap drive by $-3\,\mathrm{dB}$ as well as the voltage of the confining DC-potential by a preset amount (compare 3.3.3). This lowers the depth of the confining potential and excludes ions from higher velocity classes from being trapped. After a waiting time of $0.1\,\mathrm{ms}$ to $0.3\,\mathrm{ms}$, the trap frequencies are switched back to their original values while the cooling power is reduced to $15\,\mu\mathrm{W}$ to desaturate the cooling transition. This reduces saturation broadening around $\Gamma/2$ where cooling is most efficient leading to a lower cooling limit.

An evaluation of the laser cooling process by measuring the temperature of the Doppler cooled ion as well as an estimation of the respective wave packet size is presented in section 4.1.3.

Evaluation and reduction of the number of ions

The cooling procedure is followed by automatically counting the number of ions via imaging the ion fluorescence on a EMCCD-camera. If necessary, the control system reduces the number of ions to the desired value by lowering the axial trapping potential with a predefined voltage sequence on the DC segments of the trap. A repetition rate of

up to $3\,s^{-1}$ is achieved for the combined experimental sequence of ionising, cooling and reducing the number of ions.

4.1.2. Micromotion minimisation

Micromotion is a driven harmonic oscillation of the trapped ion, induced by the alternating radial quadrupole field (compare eq. (2.6)). It occurs as a consequence of a phase delay between the trap drive signal of opposing trap electrodes, or when the ion is shifted from the nodal position of the radial quadrupole field. The former can be minimised by ensuring that the electrical impedances of the electrodes are exactly the same. Such a mismatch can be caused for example by a difference in the inductances originating from unequal lengths of the leads to these electrodes. The latter is typically induced by residual electrostatic fields originating from patch charges on the insulating parts of the Paul trap. These fields can be counteracted by applying a respective voltage to dedicated electrodes, hereafter termed compensation electrodes. Although micromotion minimisation it is not

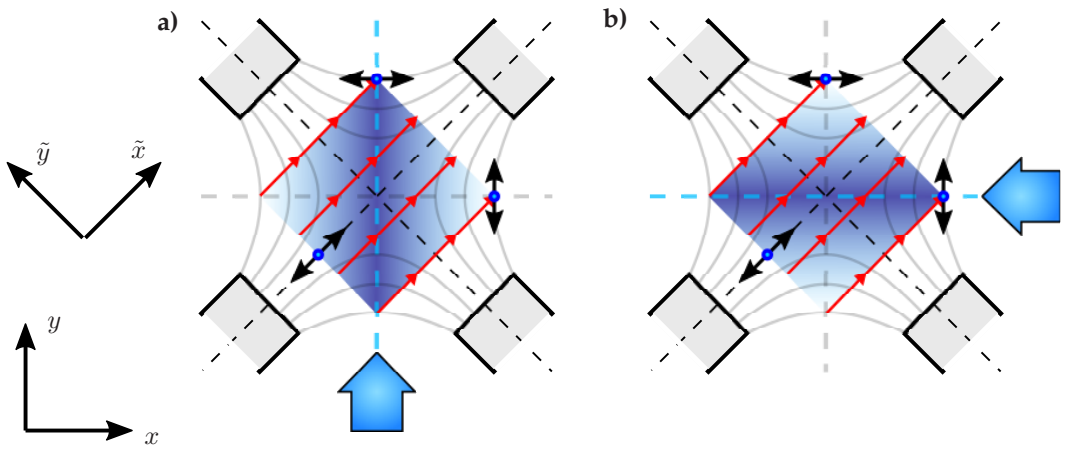

Figure 4.2.: Minimisation of the micromotion: The plots show a radial cross section through the trap including radial quadrupole field lines (gray). The red lines illustrate the scanning of the ion by applying respective voltages to the compensation electrodes. The ion is shown at three exemplary positions, with the micromotion along the field lines depicted by black arrows. **a)** If the Doppler laser from below (blue arrow, bottom) is switched on, the right position experiences maximum fluorescence, the bottom left position medium fluorescence and the top position minimum fluorescence, illustrated by the blue overlay in the background. **b)** If the Doppler laser from the side (blue arrow, right hand side) is switched on, the position on the top experiences maximum fluorescence, the bottom left position medium fluorescence and the position on the right minimal fluorescence, so that the overlay is effectively turned by $90°$.

crucial for the extraction of ions directly - as this process is synchronised to the radio frequency trap drive which additionally is switched off during the extraction - it can effect the extraction process indirectly by changing the atomic transition line shapes which results in an imperfect Doppler cooling of the ion [Ber98].

There are several well established techniques to reduce the micromotion in ion traps [Ber98, Iba11]. In this experiment, micromotion induced broadening of the cooling transition is used. This leads to a fluorescence signal which is proportional to the amplitude of the projection of the micromotion onto the k-vector of the laser beam. As a consequence, two lasers which are non parallel in their radial projection are needed in order to detect all micromotion directions in the radial plane (compare Fig. 4.2).

The minimising procedure is fully automatised in order to make it fast and reliable. With only one Doppler laser switched on, the compensation voltage is scanned in both radial directions $\tilde{x}$ and $\tilde{y}$ in small steps. At each $(\tilde{x},\tilde{y})$ position, the fluorescence signal is measured for a fixed integration time. For each row (constant $\tilde{y}$) this data is recorded and used to extract the fluorescence minimum in terms of compensation voltage via calculation of the centre of mass. The linear dependency of these minima on the $\tilde{y}$ voltage is derived using a linear regression. This line of minimal fluorescence corresponds to the voltage combinations where the micromotion amplitude in the direction perpendicular to the k-vektor of the Doppler laser is minimal. Repeating the procedure with the other laser switched on, yields another regression line with a different slope depending on the angle of this laser. The intersection of both lines is the point of minimal micromotion in the radial plane *e.g.* the nodal position of the radial quadrupole field.

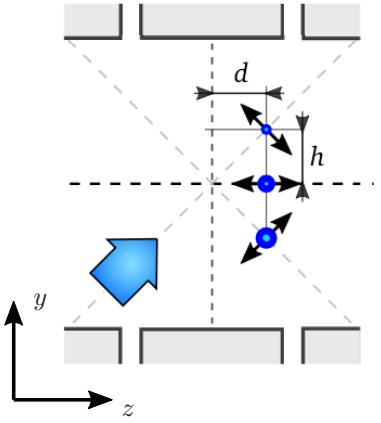

Figure 4.3.: Minimisation of the axial micromotion: If the ion is shifted by d from the position of minimal axial micromotion, there is a position shifted by h from the nodal point of the radial quadrupole field where the fluorescence is minimal. At the position where the radial micromotion is minimal the fluorescence is higher because the direction of the micromotion has a projection onto the direction of the Doppler laser (blue arrow).

The endcaps (compare 3.1.1), which are used for ion extraction, induce additional axial components of the RF field (see also Fig. 4.4 a)), giving rise to axial micromotion. Along the trap axis, the amplitude of this field is zero in the centre of the trap and rises towards the endcaps. Hence, if the ion position is shifted from the trap centre, axial micromotion occurs. Since both Doppler lasers have also a projection on the axial direction, the picture described above becomes more complicated. As the phase of the micromotion in axial and

radial directions is the same, their amplitudes can be added vectorial. At one particular (radial) position, the amplitudes of the axial and the radial contributions add up such that the direction of the micromotion becomes perpendicular to the Doppler laser (see Fig. 4.3). This results in a parallel shift of the line of minimal fluorescence signal to that position, and as a consequence, offsets the intersection point of minimal fluorescence signal as a function of the axial micromotion amplitude. Therefore this functional dependence can be used to minimise the axial micromotion. To this aim, the procedure for radial micromotion minimisation is performed for different positions of the ion along the trap axis. The results of this procedure are compared according to the shift of the ion on the camera image when the trap drive voltage is lowered by 5 dB, because this shift is directly proportional to the residual uncompensated shift from the nodal position. The axial compensation voltage is chosen where the shift of the ion with respect to its original position is smallest, because this indicates minimal axial micromotion. Typical variations of micro-motion compensation voltages amount to 3%, between different days of measurement.

4.1.3. Resolved sideband spectroscopy

In order to perform resolved sideband spectroscopy the $4^2S_{1/2}$ to $3^2D_{5/2}$ quadrupole transition (compare 2.2.2) at 729 nm is used. In the presence of a magnetic field it splits into 10 different Zeeman transitions (compare section 2.2.1). For all measurements presented here, a magnetic field of $B = 0.7$ mT is applied. This ensures well separated carrier transitions, such that their motional sidebands do not interfere with each other, while at the same time one is able to fully address all transitions within the 20 MHz range of the AOM which is employed for scanning of the laser light (see 3.5.1). Furthermore, a configuration is used, where the laser is incident from the top, having an angle of $\Theta = (\pi/2,\pi/4,\pi/4)$ with respect to the principal axes of the trap (see also 3.5.1). As a result, only radial modes are addressed, while at the same time the k-vector is perpendicular to the magnetic field. If additionally the polarisation is chosen to be perpendicular to the magnetic field, only transitions with $|\Delta m| = 2$ can be excited [Roo00]. A particular transition is selected by tuning the laser to the respective frequency via the AOM. In case of performing temperature measurements or sideband cooling, the $S_{1/2}(m = +1/2)$ to $D_{5/2}(m = +5/2)$ transition is used for the coherent excitation. For both applications, the process is advanced by coupling the upper level to the $P_{3/2}(m = +3/2)$ level via the 854 nm laser (see 3.5.1).

Temperature measurement

First, the temperature of the normal modes of the ion are determined after Doppler cooling. To this aim, the mean phonon numbers of these modes are measured by driving Rabi oscillations on the carrier as well as on the blue and red sideband transitions of the respective mode (compare 2.2.7). The oscillation signal is obtained by determining the excitation probability as described in 2.2.5 when scanning the waiting time. In order to extract the temperature, the oscillations are simultaneously fitted with equation (2.21)

while taking into account the Rabi frequencies of the transitions (equation (2.19)) to eliminate the dependence on the coupling strength Ω_0. From the phonon number, the temperatures as well as the wave packet sizes can be calculated using equation (2.21) and equation (2.25), respectively. The results of these measurements and the calculations are shown in table 4.1.

direction i	$\bar{n}$	ν_i (kHz)	T (mK)	σ_{th} (nm)
z	23.3 ± 1.3	947.5	1.08 ± 0.06	79.7 ± 2.2
z^*	27.2 ± 1.6	947.5	1.25 ± 0.07	85.9 ± 2.5
$\tilde{x}$	14.9 ± 0.5	1916.1	1.42 ± 0.05	45.1 ± 0.7
$\tilde{y}$	20.4 ± 0.6	1311.7	1.32 ± 0.04	63.5 ± 0.9
x, y	-	-	-	52.0 ± 0.6

Table 4.1.: Measured mean phonon numbers $\bar{n}$ of the respective modes i at the trap frequencies ν_i with the calculated temperatures T and the corresponding 1-sigma sizes of the thermal wave packet. The axial direction (z) is measured with (*), and without high voltage switch connected. The σ_{th} in x and y directions are calculated assuming an elliptical source and an angle of $\pi/4$ between $\tilde{x}$ and x.

The phonon number of the axial (z) mode is measured for the case where the high voltage switches are connected to the endcaps and the case where they are disconnected, in order to quantify the influence of the noise generated by these switches. However, for the fluctuations of the ion energy after the extraction, the temperature of the axial mode is negligible, given that the effect of the fluctuation of the extraction voltage is about eight orders of magnitude larger (compare section 4.2). The measurements of the radial ($\tilde{x}$,$\tilde{y}$) modes are not showing any influence of the high voltage switches. This can be explained by the shape of the electrical field of the endcaps, which on the trap axis only has a projection in axial (z) direction.

Ground state cooling

Sideband cooling via the $4^2S_{1/2}$ to $3^2D_{5/2}$ quadrupole transition (compare section 2.2.6) is applied in order to reach temperatures below the Doppler limit, at corresponding energies close to the motional ground state. Subsequently, a measurement of the mean phonon numbers is performed to evaluate the effects of the sideband cooling. Additionally, the heating of the ion per time, also termed heating rate, is determined by measuring the temperature increase after different waiting times following the cooling. This heating results from electrical field noise which may have various origins [Bro15]. The heating rate is of importance here, because it limits the temperature achievable with cooling and as a consequence the attainable emittance.

direction i	$\bar{n}$	ν_i (kHz)	T (µK)	σ_{th} (nm)	$\dot{\bar{n}}$ (ms^{-1})
$\tilde{x}$	1.2 ± 0.04	3339.7	264 ± 7	11.3 ± 0.1	0.8
$\tilde{y}$	2.5 ± 0.09	2925.8	417 ± 13	16.1 ± 0.2	20
x, y	-	-	-	13.1 ± 0.1	-

Table 4.2.: Measured mean phonon numbers of the radial modes at the respective trap frequencies with the calculated temperature T, the 1-sigma size of the thermal wave packet σ_{th} and the corresponding heating rates $\dot{\bar{n}}$. Even after a variety of tests and checks - including switching the anisotropy in the radial direction and grounding the DC-electrodes close to the ion - the reason for the fact that the heating rate of the $\tilde{y}$ direction is more than one order of magnitude larger than in the $\tilde{x}$ direction remains unclear. It can possibly be attributed to insufficient or defective gold coating of the respective electrodes.

Simultaneous cooling of both radial modes is required, as the goal of the cooling is to minimise the phase space occupation of the ion's wave function in the respective directions. The mode with the lowest heating rate is cooled first to keep heating as low as possible during the cooling of the other. Table 4.2 contains the measured heating rates of the radial modes and their minimal temperatures achieved with sideband cooling after consecutive cooling of both. The heating rates are determined by additionally inserting 1 ms and 2 ms waiting times between the cooling and the temperature measurements, with subsequently extracting the values by means of linear regressions.

4.1.4. Trapping and sympathetic cooling of N_2^+

Ions other than calcium, are loaded to the trap by means of an ion gun (3.4.2). In order to load nitrogen, initially, a single calcium ion is trapped, which will act as the cooling agent for the sympathetic cooling [Kie00, Wüb12]. Subsequently, a beam of molecular nitrogen ions with an energy of 500 eV is coupled into the trap by directing it through the aperture of the endcap facing the gun, for a given period of time. Using this blanking method, the typical exposure required for loading one nitrogen ion in average is 200 ms. Successful trapping and cooling of a nitrogen ion is detected by a shift of the calcium ion on the camera image by half the inter ion spacing. If no nitrogen is detected, the blanking procedure is repeated. If two nitrogen ions are trapped, the crystal will melt. In this case the trap is cleared and the loading procedure is started afresh. The whole loading and detection procedure is repeated until a crystal consisting of one calcium and one nitrogen ion is generated.

For the extraction the crystal has to be in the right order. This is necessary as because of the difference in charge to mass ratio, the nitrogen molecule will have a higher velocity than the calcium. If the calcium is ahead, the nitrogen therefore would have to pass the calcium, which was found to be detrimental for the beam divergence. To prevent this, the order is checked via the camera image prior to extraction. In case of wrong order, the radial trap frequency is temporarily lowered to the regime where the crystal orientation becomes perpendicular to the trap axis. When the radial trap frequency is increased back

to the old value the ions can swap their positions [Kau16]. This procedure is repeated until the right order is detected. With this method, loading rates of single nitrogen molecular ions of about 1 per minute are achieved.

Another element which successfully can be loaded is argon. Thereby, slightly higher loading rates of about 4 ions per minute are found. This is attributed to the better mode coupling between argon and calcium because of the same charge to mass ratio, which leads to a more efficient sympathetic cooling of argon when compared to nitrogen. This demonstration also serves as a proof of principle for the trapping of other species than nitrogen.

4.2. Ion extraction: Implementation of the single ion source

This section describes the implementation of a deterministic ion source by extracting single ions from the trap, which represents the most essential experimental tool for performing the single ion microscopy and single ion implantation of chapter 5 and 6.

Section 4.2.1 *Synchronising the extraction process* explains the interaction of all components and devices involved in the extraction, as well as the procedure of adjusting their synchronisation. In particular this concerns calibrating and evaluating the switching times of the extraction voltages, as well as the delay for switching off of the radio frequency drive. 4.2.2 *Time-of-flight measurement* contains a detailed measurement and analysis of the *time of flight* (TOF) of the ions and its fluctuations, which subsequently is used to calculate the energy and dispersion of the beam. In section 4.2.3 *Beam parameters*, a profiling measurement to derive the beam divergence is presented and the results are discussed. Moreover, this section contains a calculation of the beam emittance for different ion temperatures. 4.2.4 *Beam deflection* describes the deflection of the ions via dedicated electrodes and an exemplary determination of the deflection coefficient for a certain voltage. In addition, the effect of electrical noise on this electrodes is discussed.

4.2.1. Synchronising the extraction process

Ions are extracted from the trap by applying a high voltage of $0.3\,\mathrm{kV}$ to $6\,\mathrm{kV}$ to one endcap (compare 3.3.3). All devices included in this process, namely the switches for the extraction voltage and the switch of the RF trap drive are synchronised to the phase of the RF trap drive signal as well as the phase of the mains.

Near the endcaps the RF field has strong axial components (see Fig. 4.4a)). In the course of extraction these fields modulate the kinetic energy of the ions depending on the relative phase between RF drive and extraction time. Synchronising the extraction to the RF drive thus serves to unify this influence among extractions, whereas the switching off of the RF additionally minimises this influence. For illustration, Fig. 4.4b) shows the modulation of the measured TOF of the ions when not switching off the RF drive. At the slopes the standard deviation is largest, because the jitter of the switch for the extraction voltage $S_{\mathrm{ext},1}$ leads to a jitter in the modulating field. Distribution of the TTL signals which triggers the switches for both purposes and additionally initiate the detector readout, is accomplished

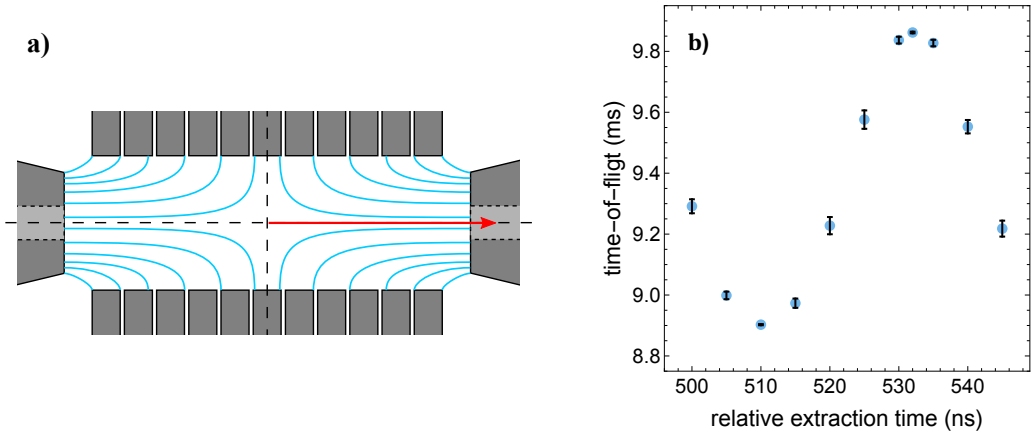

Figure 4.4.: Modulation of the kinetic energy of the extracted ion by the axial RF fields. **a)** Sketch of the RF field lines (blue) in the plane of the RF electrodes. The red arrow indicates the path of the ion during the extraction. The closer the ion gets to the endcap, the stronger the influence of the axial components of the RF field gets. **b)** Measured TOF of ions extracted with $500\,\mathrm{V}$ for different extraction times t_A. Each point represents the mean value of 50 extractions, where the error bars are drawn according to the standard deviation. The modulation of the ion energy leads to a modulation in the TOF.

by a delay generator (compare 3.3.3). A timing chart showing the different TTL signals can be found in Fig. 4.5.

Switching of the extraction voltage

When setting up the extraction experimentally, the times for the on and off switching of the extraction voltage are adjusted first. Triggering to an arbitrary but fixed phase defines the time $t = t_0 = 0$. After a fixed time, at $t = t_\mathrm{A}$ a negative extraction voltage $U_{\mathrm{ext},1}$ is applied to one endcap via the corresponding high voltage switch $S_{\mathrm{ext},1}$. For the adjustment, this time is chosen to be $t_\mathrm{A} = 500\,\mathrm{ns}$. Later on t_A will be scanned in order to change the relative phase between RF signal and extraction. When the ion is now accelerated towards the endcap, the time needed to reach its aperture depends on the applied voltage. If this voltage is switched off at $t = t_\mathrm{B}$ before the ion reaches the endcap, the total ion energy will decrease the earlier the voltage is switched off. Whereas the energy remains unchanged, if the switching (t_B) is accomplished while the ion is already within the endcap. Therefore, for a given extraction voltage, this effect can be used to determine the time when the ion reaches the endcap (see Fig. 4.6) and subsequently choose the switching time accordingly. Typically the switching is performed within the endcap, as this has the advantage of being most efficient in terms of energy while at the same time being less susceptible to switching jitters which would alter the ions energy when switching before reaching the endcap.

In order to increase the maximum extraction energy, instead of switching off the voltage, it can be changed to a positive value $U_{\mathrm{ext},2}$ via the second switch $S_{\mathrm{ext},2}$, in effect accelerating the ion further when it leaves the encap on the other side.

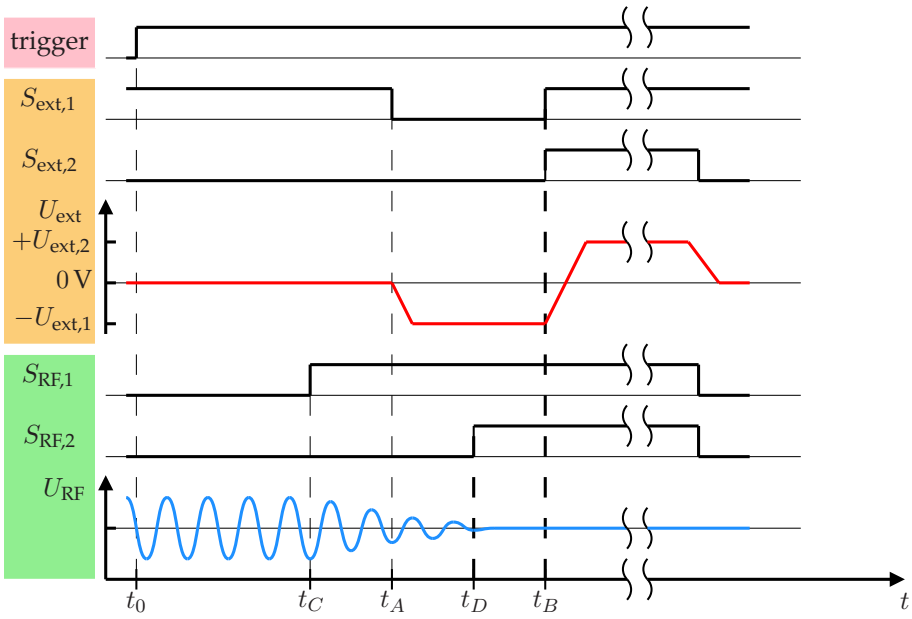

Figure 4.5.: Timing chart for the TTL signals (black) controlling the extraction signal (red) and the switching of the RF amplitude (blue). Note that the TTL of the switch $S_{ext,1}$ is inverted.

As mentioned above, the relative phase between RF signal and extraction can be changed by scanning t_A. For the first experiments this was used to carefully adjust t_A to a turning point in the modulated energy of the ions in order to reduce the influence of the switching jitter (compare Fig. 4.4 b)). However, in later experiments, the radio frequency drive is switched off for the extraction, suppressing the modulation of the ions kinetic energy bellow the limit of detection in terms of TOF (compare Fig. 4.6 b) in the following section).

Fast switching off of the radio frequency drive

The off switching process of the RF trap drive consists of two independent steps, both triggered by a TTL signal (compare 3.3.2). First, at $t = t_C$ the phase of the signal is shifted by π and switched to a 6 dB higher amplitude via $S_{RF,2}$. This effectively generates a superposition between the rising shifted signal and the decaying unshifted signal in the helical resonator. The superposition yields destructive interference when both signals reach equal amplitude. The second step consists in switching off the generator signal with $S_{RF,1}$ at precisely this zero crossing at $t = t_D$. This method has the advantage of being much faster than just switching off the generator signal, because of the otherwise slow damping of the resonator.

To adjust this process, the delay between the phase shifting at t_C and the off switching at t_D is varied until the remaining signal after the helical resonator is minimal. Subsequently, the switching time of the extraction voltage t_A is shifted[78], such that the damping of the RF

[78] In practice t_B is shifted in parallel, to keep the turn-on duration of the extraction voltage constant.

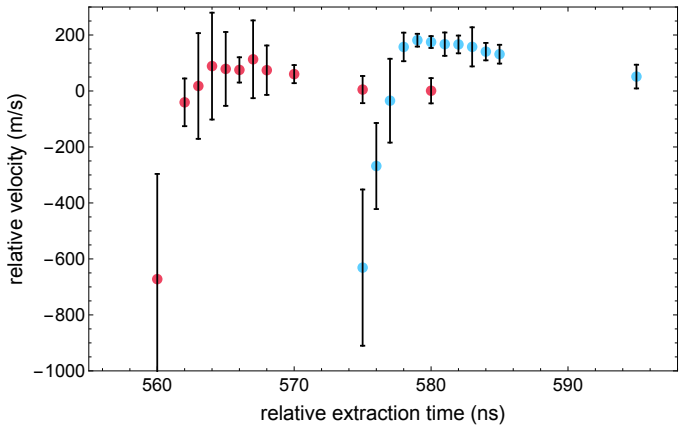

Figure 4.6.: Switching off of the extraction voltage for calcium (blue) and nitrogen (red). Each point shows the relative mean velocity of 20 extracted ions for a given switching off time t_B. The velocity grows until the switching (t_B) happens within the endcap.

signal is completed before the ion reaches the aperture of the endcap. This is accomplished by measuring the TOF (compare 4.2.2) for different shifts and recording the modulation as shown in Fig. 4.7 b). Typically a point close to where the damping of the modulation ends is chosen. If the waiting time is to long the emission direction of the beam will start to deviate, because in this case the damping starts before the extraction voltage is applied.

4.2.2. Time-of-flight measurement

The extraction energy determines the velocity as well as the TOF of an ion. Consequently, fluctuations of the extraction energy lead to fluctuations of both quantities and give rise to the measurement uncertainty of their values. These extraction energy fluctuations are important in order to estimate their effect in chromatic aberration and in the variation of the penetration depth when implanting ions into solid substrates, whereas energy fluctuations resulting from a finite ion temperature are too small to play a role in the total energy fluctuations which are discussed in the following.

In the present experiment, measuring the TOF is the only means to precisely determine the ion energy and velocity. However, this procedure introduces additional errors biasing the physical TOF information. On the one hand, there are systematic errors, caused by delay times and an imperfect acceleration, both of which are shifting the mean TOF values. Their precise extent will be determined by measuring the TOF at different extraction energies and fitting a corresponding model. On the other hand, there are statistical fluctuations resulting from technical limitations of the measurement procedure which add to the physical TOF fluctuations. Since the latter depend on the extraction energy and the former are invariant, the value of both fluctuations can be distinguished and determined by measuring the total TOF fluctuations as a function of the extraction energy and fitting a model accordingly. The TOF is measured between the trigger signal, controlling the switch for the extraction voltage and the detection time, which is given by the raising edge of the

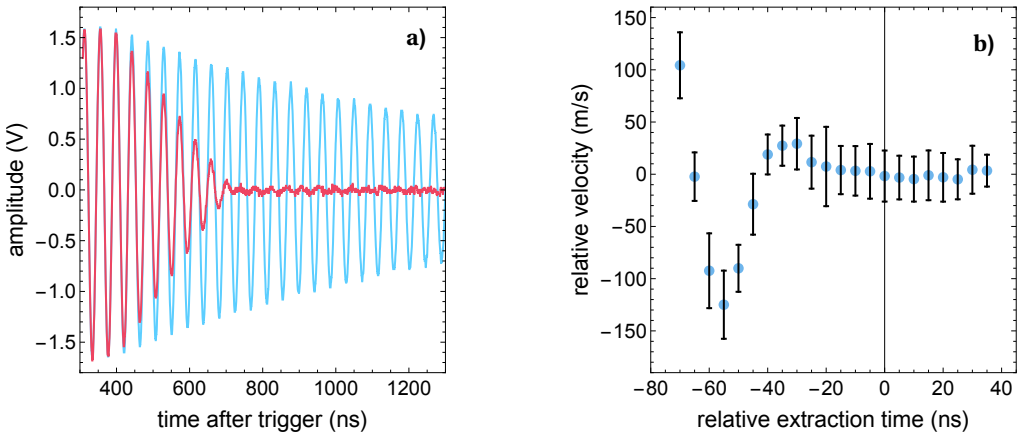

Figure 4.7.: Switching off of the RF drive. **a)** Voltage signal as measured at the capacitive divider, without (blue) and with switching (red) to the phase shifted signal. **b)** Adjustment of the extraction time t_A. The measured relative velocity is plotted as a function of the relative extraction time t_A. Each point represents the mean value of 50 extractions, where the error bars are drawn according to the standard deviation. The ions corresponding to six points on the left hand side are modulated by the axial RF fields *i.e.* the RF drive is not yet switched off completely when these ions enter the endcap. The zero of the relative extraction time is the time which is used for further experiments.

detector signal. A typical TOF measurement with 50 ions, extracted independently with an extraction voltage of 900 V, is shown in Fig. 4.8 b). Here, the TOF exhibits a mean value of 7525.0 ns and a standard deviation of 0.98 ns. This corresponds to an average velocity of 58.9 km/s and a standard deviation of 8.0 m/s. It has to be mentioned here, that this standard deviation permits to discriminate between the mass of adjacent elements by about 40 standard deviations at the energies and masses used here.

The measured TOF t_{meas} as a function of the extraction voltage is shifted by the aggregate delay time t_{del} and stretched by the efficiency coefficient k with respect to the physical TOF t_{phys}. The aggregate delay time consists of the switching delay, the delay caused by the detector and the signal propagation times. The efficiency coefficient accounts for the imperfect transformation of the the extraction voltage into kinetic energy due to a potential offset and for the acceleration time[79]. To determine the values of both parameters, the average TOF is measured for different extraction voltages and fitted with a model considering these dependencies (see Fig. 4.8 a)). The model for the TOF reads:

$$t_{\text{meas}}(U_{\text{ext,1}},U_{\text{ext,2}}) = t_{\text{phys}} + t_{\text{del}} = \sqrt{\frac{m s_1^2}{2 k_1 U_{\text{ext,1}} e}} + \sqrt{\frac{m(s_{\text{det}} - s_1)^2}{2\left(k_1 U_{\text{ext,1}} + k_2 U_{\text{ext,2}}\right) e}} + t_{\text{del}}, \quad (4.1)$$

where t_{del} is the aggregate delay time, $U_{\text{ext,1}}$ and $U_{\text{ext,2}}$ are the extraction voltages for the pulling and pushing potential, with respective efficiency coefficients[80] k_1 and k_2, m is

[79] The delay caused by the time needed for the ion acceleration scales in the same way to the extraction voltage as the TOF of a particle with constant velocity.

[80] The model is not taking into account the finite rise time of the extraction voltage.

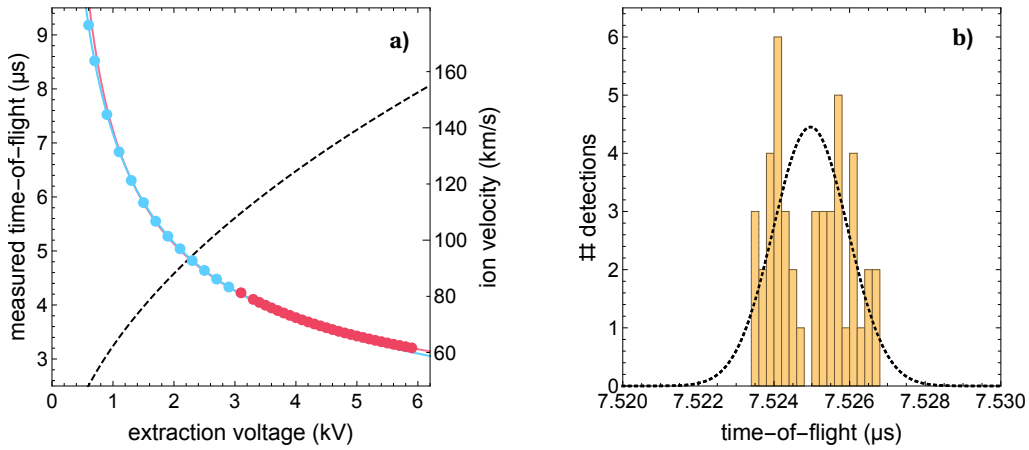

Figure 4.8.: TOF measurement: **a)** The dots show the mean value of the measured TOF, for different extraction voltages. Each data point represents the average of 50 independent extraction events (see (b)). For energies below 3keV (blue), the ion is accelerated using only a pulling potential. For energies above 3keV (red) the voltage at the endcap is additionally switched to a positive voltage while the ion is in the endcap. The solid lines are drawn according to the fitted model function $t_{\text{meas}}(U_{\text{ext},1},U_{\text{ext},2})$ (equation (4.1)). The dashed line shows the ion velocity as a function of the extraction voltage, calculated from the bias-corrected flight times. **b)** TOF histogram of detection events at an extraction voltage of 900 V. The dashed black curve is a Gaussian, drawn according to the mean and the standard deviation of the data.

the mass of the ion, $s_1 = 30\,\text{mm}$ is the distance from the centre of the trap to the end of the endcap, $s_{\text{det}} = 428\,\text{mm}$ the distance between source and detector and e the charge of the ion. The model assumes constant velocities for s_1 and $s_{\text{det}} - s_1$. The fit to the data yields $k_1 = 0.805 \pm 0.002$ and $k_2 = 0.813 \pm 0.008$ for the efficiency coefficients and $t_{\text{del}} = 293 \pm 8\,\text{ns}$ for aggregate delay time.

In principle, the fluctuation in the ion energy has two different sources, the fluctuation from the temperature of the ion in the trap, which is

$$\Delta E_{\text{therm}} = \frac{1}{2} k_{\text{B}} T_z,$$

and the portion resulting from the fluctuation of the extraction voltage, which reads

$$\Delta E_{\text{ext}} = \sqrt{(k_1 \Delta U_{\text{ext},1} e)^2 + (k_2 \Delta U_{\text{ext},2} e)^2}. \tag{4.2}$$

However, because ΔE_{therm} is about eight orders of magnitude smaller than $\Delta U_{\text{ext}} e$, we can neglect it in the TOF analysis. Thus, the total energy fluctuations are given by $\Delta E_{\text{tot}} = (\Delta E_{\text{therm}}^2 + \Delta E_{\text{ext}}^2)^{1/2} \approx \Delta E_{\text{ext}}$, resulting in corresponding TOF fluctuations of Δt_{phys}. The additional statistical TOF fluctuations Δt_{tech} introduced by technical limitations of the measurement process, consist of the switching jitter of the extraction voltage, the error introduced by the detector and the limited time resolution of the oscilloscope which is used to measure the TOF. As they are all independent from the extraction energy, they

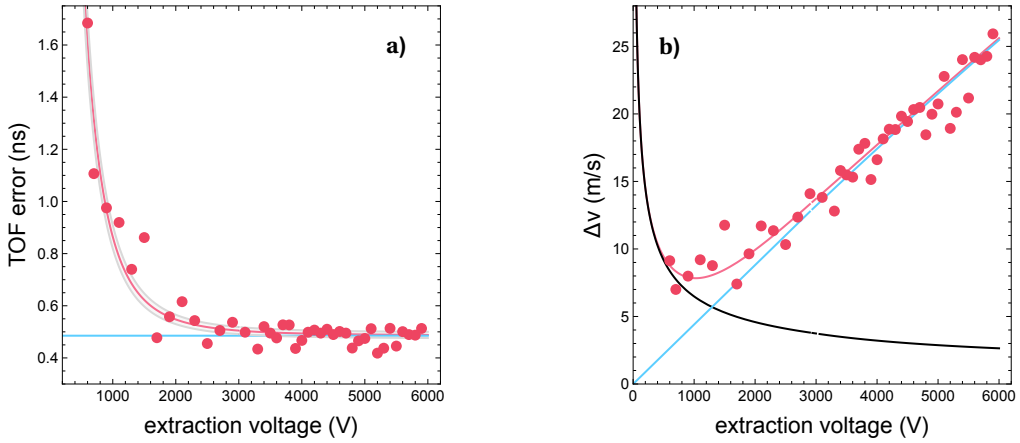

Figure 4.9.: a) TOF error: The red dots show the standard deviation of the measured TOF Δt_{meas} as a function of the extraction voltage. The red curve is drawn according to a fit to this data, where the fit error is depicted by the gray area. The blue line shows Δt_{tech} the amount of the TOF fluctuations which is introduced by technical limitations of the measurement process. **b)** Velocity error: The red dots and the red curve show the standard deviation in velocity as calculated from the TOF data from (a) and the corresponding fit, respectively. The red curve comprises fluctuations from physical as well as technical origin. Whereas the black curve and the blue curve are the amount of the standard deviation of the velocity due to the physical fluctuations and due to technical fluctuations of the TOF, respectively.

yield a constant offset to the measured TOF fluctuations. Hence, the total TOF fluctuations amount to:

$$\begin{aligned}\Delta t_{\text{meas}} &= \sqrt{\Delta t_{\text{phys}}^2 + \Delta t_{\text{tech}}^2} = \sqrt{\left(\frac{\partial t_{\text{meas}}}{\partial U_{\text{ext,1}}}\Delta U_{\text{ext}}\right)^2 + \left(\frac{\partial t_{\text{meas}}}{\partial U_{\text{ext,2}}}\Delta U_{\text{ext}}\right)^2 + \Delta t_{\text{tech}}^2} \\ &= \left(\frac{k_2^2\, m\, s_2^2\, \Delta U_{\text{ext}}^2}{8e\left(k_1 U_{\text{ext,1}} + k_2 U_{\text{ext,2}}\right)^3}\right. \\ &\left. + \frac{k_1^2 e^2}{8}\left(\frac{\sqrt{m s_1^2}}{\left(e k_1 U_{\text{ext,1}}\right)^{3/2}} + \frac{\sqrt{m s_2^2}}{\left(e\left(k_1 U_{\text{ext,1}} + k_2 U_{\text{ext,2}}\right)\right)^{3/2}}\right)^2 \Delta U_{\text{ext}}^2 + \Delta t_{\text{tech}}^2\right)^{1/2}.\end{aligned} \tag{4.3}$$

Thereby, it is assumed that the voltage fluctuations of both switches is the same, *i.e.*, $\Delta U_{\text{ext,1}} = \Delta U_{\text{ext,2}} = \Delta U_{\text{ext}}$. Fig. 4.9 shows a fit of this model to the measured TOF fluctuations. The fit yields $\Delta U_{\text{ext}} = 149 \pm 5\,\text{mV}$ and $\Delta t_{\text{tech}} = 0.49 \pm 0.01\,\text{ns}$. According to equation 4.2 the total energy dispersion amounts to $\Delta E_{\text{tot}} \approx \Delta E_{\text{ext}} = 174\,\text{meV}$.

4.2.3. Beam parameters

Direct measurement

In order to determine the values of the beam parameters position x_0 and width σ, a profiling edge, mounted on a translation stage (see section 3.2.3), is stepped into the beam and a fixed number of transmission measurements are made at each position. The simplest approach is to move the profiling edge in equidistant steps and extract the parameter values by fitting the data with a Gaussian error function (2.69) (see section 2.5.1). A more efficient profiling method compared to this linear scan is provided by the Bayes experimental design algorithm, which is presented in section 4.3.3. Fig. 4.10 shows the

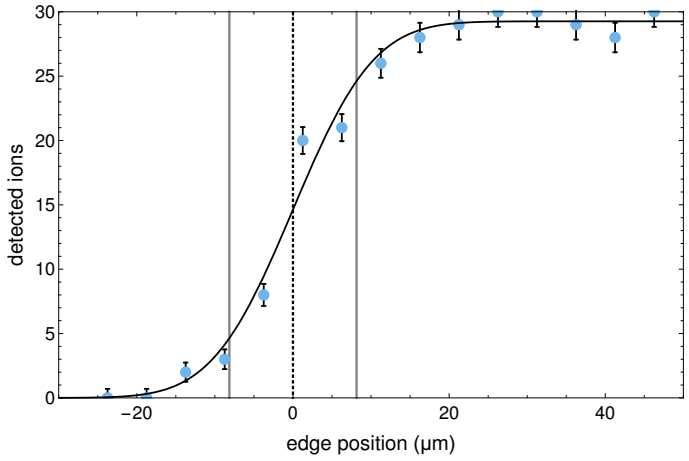

Figure 4.10.: Measurement of the beam divergence in x direction: The blue dots show the number of detected ions out of 30 single ion extractions at the corresponding profiling edge position, where the errors are determined from binomial counting statistics. The dashed line depicts the centre position and the gray lines shows the 1-σ radius of the beam. The black solid line is drawn according to a fit to the data with a Gaussian error-function.

result of a linear beam profiling measurement in x direction at an extraction energy of $5900\,\mathrm{V}$. The fit yields $\sigma_x = 8.14 \pm 0.85\,\mu\mathrm{m}$ for the 1-σ radius of the beam, $\Delta x_0 = 0.62\,\mu\mathrm{m}$ for the precision of determining the average beam-position and $a = 29.26 \pm 0.51$ ions, which corresponds to a detection efficiency of $97.5\,\%$.

From the radius, the beam divergence is calculated by $\sigma_\alpha = \sigma_x/s$, with s being the distance from the centre of the trap to the profiling edge. This yields $\sigma_\alpha = 23.7 \pm 2.5\,\mu\mathrm{rad}$. However, as it turned out, the beam divergence σ_α varies between different days of measurement. A thorough analysis of this phenomenon, comprising 28 profiling measurements from different days revealed a mean value of $\sigma_\alpha = 44.7\,\mu\mathrm{rad}$ and a standard deviation of $\Delta\sigma_\alpha = 13.4\,\mu\mathrm{rad}$. This discrepancy is attributed to residual ringing of the RF signal when the off switching process during extraction (see 4.2.1) is imperfectly adjusted.

Calculation and numerical simulation

Assuming the radial velocity as the only source of the beam divergence, both can be calculated from the radial ion temperature in the trap. However, such a calculation yields a discrepancy to the directly measured values: Taking into account a temperature of 2 mK in the radial direction results in a standard deviation of the radial velocity of $0.4\,\mathrm{m/s}$ which translates into a beam divergence of $\sigma_\alpha = 2.5\,\mu\mathrm{rad}$ when assuming an axial velocity of $155 \cdot 10^3\,\mathrm{m/s}$ (compare 4.2.2). This difference between calculated and measured values can be explained by a focussing behaviour of the extraction potential having radial field components. Numerical simulations of the extraction process indeed show such a focussing, effectively creating an intermediate focus between the centre of the trap and the endcap. This leads to an additional divergence of the beam, as shown in Fig. 4.11 a). The beam divergence from this simulation with a thermal ensemble of $T = 1.35\,\mathrm{mK}$, yields $\sigma_\alpha = 17.7\,\mu\mathrm{rad}$. In Fig. 4.11 b) the phase space distributions of the corresponding trajectories are plotted. Although, the focussing does not change the emittance of the beam, it prevents from directly calculating the emittance from the beam divergence. Nevertheless,

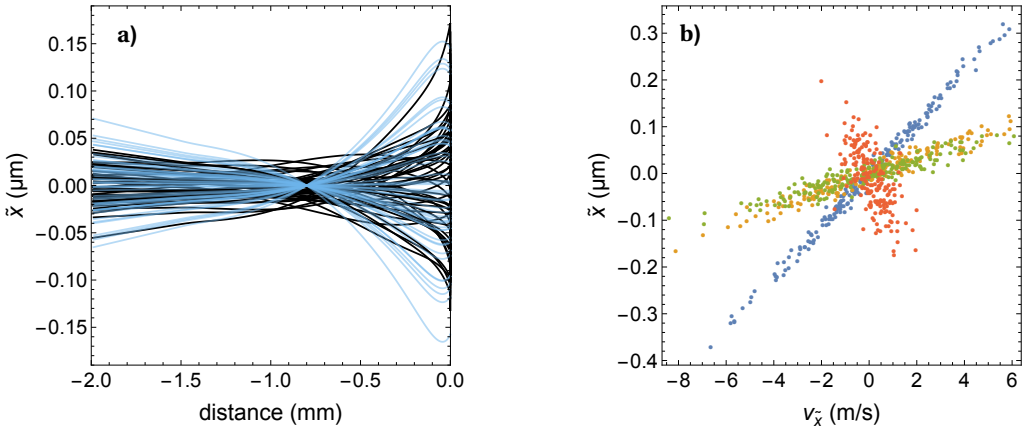

Figure 4.11.: a) Numerical simulation of the ion trajectories during extraction from the centre of the trap with realistic parameters. The black solid lines are drawn from a thermal ensemble where the radial velocity distribution and the radial spatial distribution are Gaussian and uncorrelated, whereas for the blue lines this radial velocity is set to zero in order to illustrate the focussing behaviour of the extraction process. **b)** Scatter plot in phase space in $\tilde{x}$ direction of a thermal ion ensemble during extraction at different positions along z: directly at the trap centre (red), at the intermediate focus (green), in the endcap (yellow) and 10 mm after the endcap (blue). Within the trap, the radial velocity is altered depending on the radial position, creating an additional divergence. After the endcap, the ions propagate freely with a constant divergence, only changing the radial positions.

the emittance can be calculated from the phonon numbers, measured in section 4.1.3. According to equation (2.30), the emittance in $\tilde{x}$-direction is $\epsilon_{\tilde{x}} = 1.11 \cdot 10^{-11}\,\mathrm{m\,rad}\,\sqrt{\mathrm{eV}}$ and in $\tilde{y}$-direction it is $\epsilon_{\tilde{y}} = 1.51 \cdot 10^{-11}\,\mathrm{m\,rad}\,\sqrt{\mathrm{eV}}$. The overall emittance of the Doppler cooled beam therefore is $\epsilon = \epsilon_{\tilde{x}} \cdot \epsilon_{\tilde{y}} = 1.69 \cdot 10^{-22}\,\mathrm{m^2\,rad^2\,eV}$. Fig. 4.12 shows this derived

emittances as a function of the temperature. For comparison the emittances from the phase space distribution of the simulated ion trajectories (see Fig 4.11 b)) calculated via equation (2.27) are shown. From the emittance values, equation (2.34) allows for deriving the peak brightness. Assuming an extraction rate of 3 ions per second, which corresponds to a current of $I_0 = 4.8 \cdot 10^{-19}$ A, the peak brightness amounts to $B_{\text{peak}} = 72\,\text{A}\,\text{m}^{-2}\,\text{sr}^{-1}\,\text{eV}^{-1}$. The respective emittances of sideband cooled ions are calculated

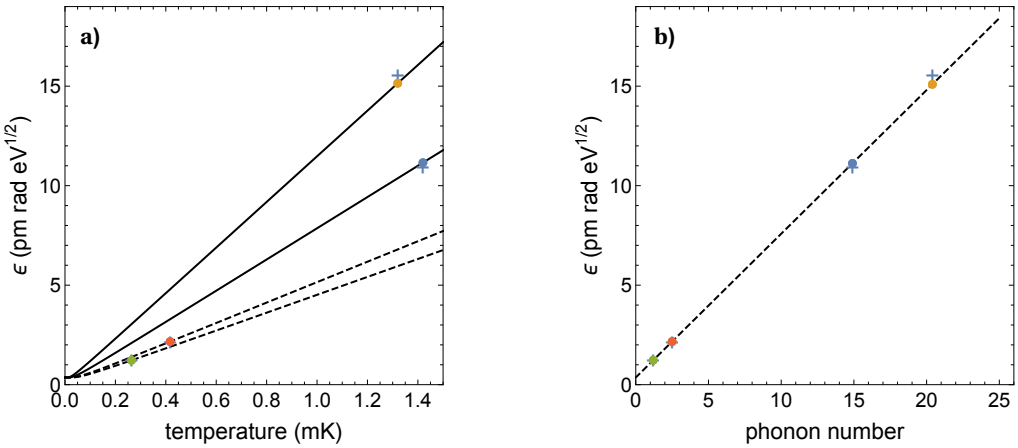

Figure 4.12.: a) The emittance as a function of the ion temperature (equation (2.31)) for the trap frequencies of the respective modes. The blue and the yellow dot indicate the emittances at the measured temperatures after Doppler cooling in $\tilde{x}$ and $\tilde{y}$ direction, respectively. The black solid lines show the extrapolation to other temperatures. The red and the green dot show the measured temperatures after sideband cooling, where the dashed lines are the extrapolations. **b)** Shows the emittance as a function of the phonon number (equation (2.30)) where the measured modes are drawn according to the same colour coding as in (a). The crosses depict the results of the corresponding numerical simulations, which are performed with the same parameters.

to be $\epsilon_{\tilde{x}} = 1.21 \cdot 10^{-12}\,\text{m rad}\,\sqrt{\text{eV}}$ as well as $\epsilon_{\tilde{y}} = 2.16 \cdot 10^{-12}\,\text{m rad}\,\sqrt{\text{eV}}$ and hence, the overall emittance of the sideband cooled beam is $\epsilon = \epsilon_{\tilde{x}} \cdot \epsilon_{\tilde{y}} = 2.60 \cdot 10^{-24}\,\text{m}^2\,\text{rad}^2\,\text{eV}$, corresponding to a peak brightness of $B_{\text{peak}} = 4.7 \cdot 10^3\,\text{A}\,\text{m}^{-2}\,\text{sr}^{-1}\,\text{eV}^{-1}$.

4.2.4. Beam deflection

The direction of the beam of extracted ions can be precisely adjusted by means of deflection electrodes (3.2.1). In section 4.3 *Ion lens operation*, this is used to align the beam to the axis of the lens. As a prerequisite for this, it is necessary to know the change in deflection angle $\Delta\alpha$ per alteration in deflection voltage ΔU_{defl} for a specific ion energy. This deflection coefficient $m_\alpha = m/h$, can be determined experimentally by measuring the beam position d for different deflection voltages at a given distance h from the deflection electrodes and calculate $m = \Delta d/\Delta U_{\text{defl}}$. An example of such a measurement in x direction, at an extraction voltage of 5900 V can be seen in Fig. 4.13. With the results from this measurement the deflection coefficient reads $m_\alpha = m/h = 1.21 \pm 0.01\,\text{mrad/V}$, with $h = 298.6\,\text{mm}$.

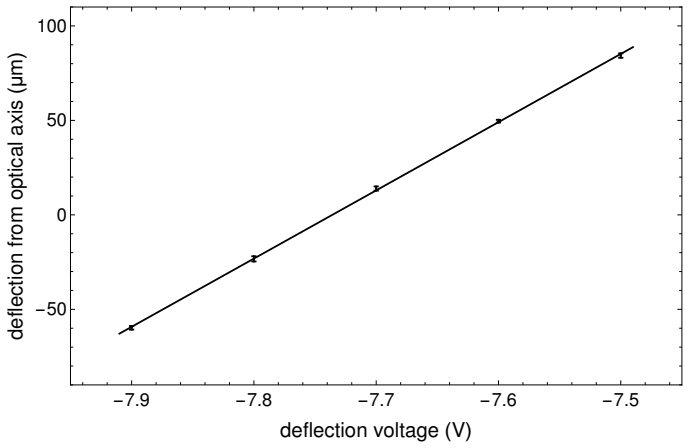

Figure 4.13.: Determination of the deflection coefficient in x direction: The points show the beam position d as a function of different deflection voltages U_{defl}. They are obtained with the profiling edge method described in section 4.2.3. The errorbars are drawn according to the fit errors. A linear regression is used to extract the slope m. It yields $m = 361.1 \pm 2.7\,\mu\text{m/V}$.

Typical fluctuation of the deflection voltages are in the order of $\Delta U_{\text{defl}} \approx 0.2\,\text{mV}$, resulting in a fluctuation of the deflection angle of $\Delta\alpha = m_\alpha\,\Delta U_{\text{defl}} = 242 \pm 2\,\text{nrad}$. Since this is small compared to the 1-σ beam divergence of $\sigma_\alpha = 23.7\,\mu\text{rad}$, as measured in section 4.2.3, the effect of this additional fluctuation in terms of spherical aberration can be neglected (compare 4.3.1). However, a change in the deflection voltage also moves the lateral position of the focus as the deflection electrodes are not placed directly at the source. This is because they do not solely alter the beam direction, but also virtually move the source position (compare 3.2.1) and hence, yield a virtual broadening of the source size $\Delta\sigma_r$ as a function of a fluctuation of the deflection voltage ΔU_{defl} which is described by

$$\Delta\sigma_r = g \cdot m_\alpha \cdot \Delta U_{\text{defl}} = g \cdot \Delta\alpha, \tag{4.4}$$

where $g = 46.3\,\text{mm}$ is the distance from the trap to the deflection electrodes. As a result, the source is broadened by $\Delta\sigma_r = 11.2 \pm 0.8\,\text{nm}$ and the focus is broadened by $\Delta r = \Delta\sigma_r \cdot M = 0.44 \pm 0.04\,\text{nm}$, with $M = 0.039$ being the magnification of the lens (compare 4.3.5).

Another, possible error source may be the deflection by spin forces in magnetic field gradients. Such a deflection, however, was ruled out by comparing the beam position of a spin polarised beam (compare 2.2.4) with a randomly initialised beam, where no measurable difference occurred.

4.3. Ion lens operation

This section discusses the operation of the electrostatic einzel lens, which is used to focus the beam of single ions to a spot of a few nanometers. First, in 4.3.1 *Measurement of*

spherical aberration and beam alignment, the coefficient of spherical aberration is determined and the implications on the focal radius are calculated and discussed. Furthermore, this measurement provides a way to align the beam to the axis of the lens. In section 4.3.2, the previously measured beam divergence is used to calculate the effect of chromatic aberration as a function of the extraction energy. In 4.3.3, two methods to measure the beam focus are presented and the results are discussed and compared. Moreover, the long term stability of the focus position and the focal radius is determined in 4.3.4 *Measurement of the two-sample deviation*. To put all the above results in a broader context the beam waist is measured in 4.3.5. This allows for extracting the source size, compare it to the previous findings and discuss the result with respect to the lens error calculated before.

4.3.1. Measurement of spherical aberration and beam alignment

The focusing behaviour of the lens, taking into account spherical aberration, is modelled by equation (2.42). It describes the refraction of the incident beam as a function of the incident angle α. Spherical aberration is the non-linear term in this dependency. It can

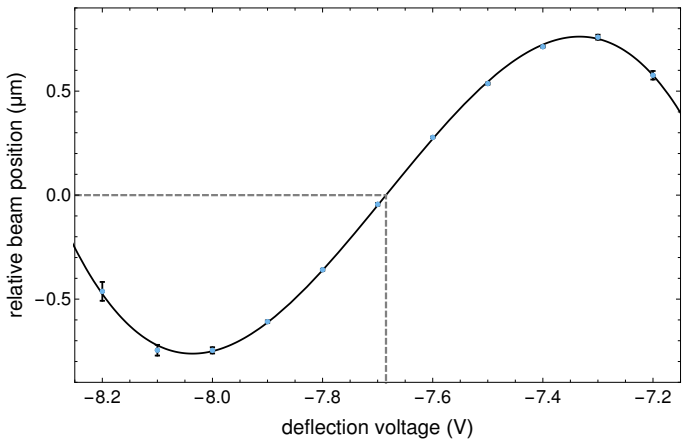

Figure 4.14.: Measurement of the spherical aberration coefficient: The beam position is measured at given deflection voltages ranging from $-8.2\,\mathrm{V}$ to $-7.2\,\mathrm{V}$. The error bars are drawn according to the fit errors of each measurement. The data points are drawn relative to the symmetry axis and are fitted with equation (4.5) to extract the focal length f, the coefficient of spherical aberration c_2 and the offset to the symmetry axis r_0. The data shows, that a deflection voltage of $U_0 = -7.684 \pm 0.002\,\mathrm{V}$ is required to align the beam to the symmetry axis of the lens (vertical dashed line).

be determined experimentally, via deliberately scanning α by deflecting the incident beam from the optical axis and measuring the corresponding beam positions at a given distance from the principal plane of the lens. The aberration coefficient c_2 can now be extracted by fitting this data with function (2.42), where α can be expressed in terms of deflection voltage $\alpha = m_\alpha(U_{\mathrm{defl}} - U_0)$, and $m_\alpha = 1.21\,\mathrm{mrad/V}$ is the deflection coefficient

as determined in 4.2.4. This yields

$$r(U_{\text{defl}}) = \left(S_1 + S_2 - \frac{S_1 S_2}{f}\right) m_\alpha(U_{\text{defl}} - U_0) + \frac{c_2 S_1^3 S_2}{f^2} \left(m_\alpha(U_{\text{defl}} - U_0)\right)^3 + r_0. \quad (4.5)$$

Here $S_1 = 285.8\,\text{mm}$ is the distance from the deflection electrodes to the principal plane of the lens. The position of the principal plane is obtained from numerical simulations[81]. $S_2 = 12.97\,\text{mm}$ is the distance from the principal plane to the profiling edge. For the fit, the remaining parameters are free: f is the focal length, U_0 is the deflection voltage where the beam goes trough the centre of the lens, and an offset r_0 is introduced to take into account the distance to the zero position of the profiling edge in terms of piezo coordinates. The results from the aberration measurement in x direction as well

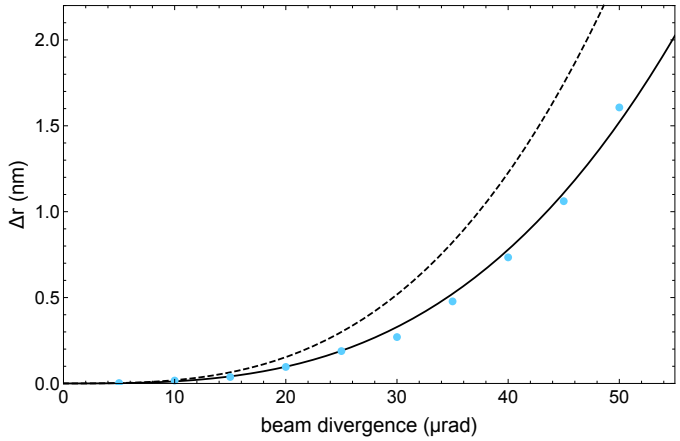

Figure 4.15.: Numerical simulation of the spherical aberration coefficient: The 1-σ beam radius for different given divergences of the incident beam is determined from trajectory simulations. This data points (blue) are fitted with equation (2.46) to extract the coefficient of spherical aberration C_s. The black curve is drawn according to the fit. For comparison, the dashed line shows the curve for the aberration coefficient obtained from the measurement.

as the fit to this data can be seen in Fig. 4.14. The fit yields $f = 12.522 \pm 0.001\,\text{mm}$, $U_0 = -7.684 \pm 0.002\,\text{V}$ and $c_2 = 2.57 \pm 0.05\,\text{mm}^{-1}$. According to equation (2.47), this corresponds to a $C_\text{s} = 1122 \pm 20\,\text{mm}$ (see 2.4.2). A numerical simulation (compare 2.4.3), where the focal radius as a function of the beam divergence was fitted with equation (2.46) yields $C_\text{s} = 712 \pm 14\,\text{mm}$ (see Fig. 4.15). The discrepancy between these values is attributed to a deviation of the exact edge rounding of the electrode apertures of the real lens from those of the simulated lens. Taking into account the coefficient from the measurement, the focal radius increases by $\Delta r = 255 \pm 52\,\text{pm}$ as calculated with equation (2.45) and assuming $\sigma_\alpha = 23.7 \pm 2.5\,\mu\text{rad}$ from the previous measurement of the beam divergence.

The symmetry of function (2.42), resulting from its non-linear dependency on the deflection voltage, allows for alignment of the beam to the symmetry axis of the lens, by

[81] The principal plane is at the point where a paraxial incident beam intersects the exiting convergent beam.

setting the deflection voltage to $U_{\text{defl}} = U_0$. Once the above measurement is evaluated, the beam alignment can be drastically simplified by moving the profiling edge position to $r = r_0$ where it intercepts the symmetry axis of the lens. A subsequent profiling measurement, where the deflection voltage U_{defl} is scanned, rather than the position of the profiling edge, yields U_0.

4.3.2. Calculating the effect of chromatic aberration

The increase of the focal radius due to chromatic aberration can be calculated with equation (2.50) and taking into account the previously measured beam divergence and energy spread.

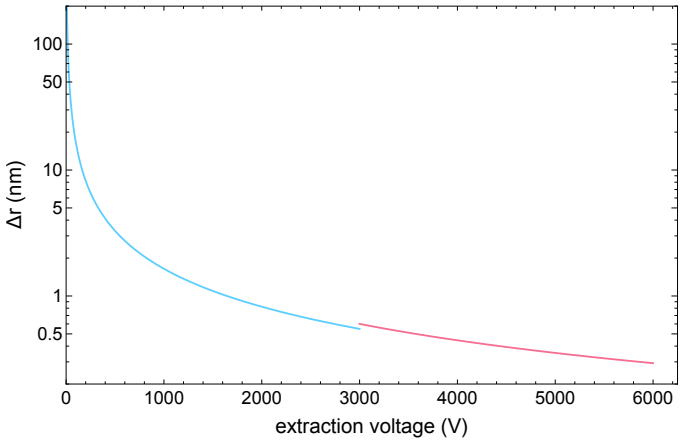

Figure 4.16.: Calculated chromatic aberration assuming a constant beam divergence. The blue curve only takes into account the fluctuations on the acceleration voltage of the first high voltage switch, whereas the red curve considers the fluctuations of both switches.

Fig. 4.16 shows the increase of the focal radius as a function of the kinetic energy $E_{\text{kin}} = (k_1 U_{\text{ext,1}} + k_2 U_{\text{ext,2}})\, e$, plotted on a logarithmic scale. The calculation neglects the dependence of the beam divergence from the extraction voltage.

4.3.3. Measurement of the beam focus

For an accurate determination of the spatial resolution in the focal plane, a linear profiling measurement in x direction, analogue to that from the determination of the beam parameters in section 4.2.3 is performed. Fig. 4.17 shows the result of such a measurement, conducted under optimal conditions. To obtain the beam parameters, the data is fitted with a Gaussian error function $p(x) = \frac{a}{2}\left[1 + \text{erf}\left(\frac{x-x_0}{\sigma_x\sqrt{2}}\right)\right]$. This yields $\sigma_x = 5.8 \pm 1.0\,\text{nm}$ for the 1-σ radius of the beam waist, $\Delta x_0 = 0.6\,\text{nm}$ for the precision of determining the beam-position and $a = 28.1 \pm 0.5$, which corresponds to a detection efficiency of $93.7 \pm 1.7\,\%$.

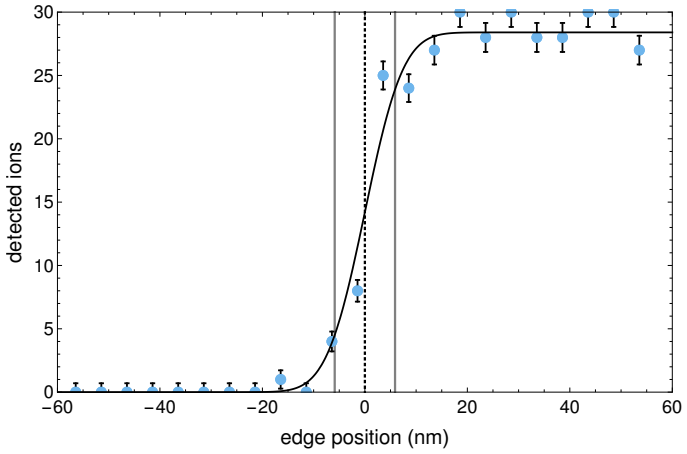

Figure 4.17.: Beam profiling measurement in x direction: The blue dots show the number of detected ions out of 30 single ion extractions at the corresponding profiling edge position, where the errors are determined from binomial counting statistics. The dashed line depicts the centre position and the gray lines the 1-σ radius of 5.8 ± 1.0 nm of the beam waist. The black solid line is drawn according to a fit to the data with Gaussian error-function.

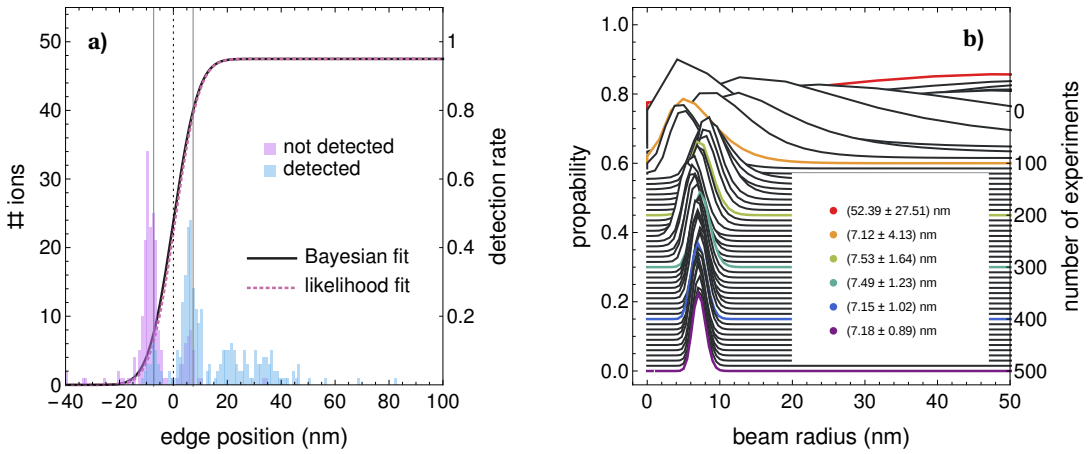

Figure 4.18.: a) Profiling edge measurement in the focal plane using the Bayes experimental design method: The histogram shows the optimal blade positions of 500 ion extraction events, as calculated by the algorithm during the measurement. This data is split into cases where the ion was detected (blue) and cases where it was not (purple). The Bayes fit function $p(y = 1|\theta,\xi)$ is drawn according to the final parameter values (black), where the zero of the x-axis is set to x_0, the mean value of the beam position. For comparison, a maximum likelihood fit is drawn (dashed, purple). **b)** The marginal PDF of the beam radius as a function of the number of experimental iterations in the Bayes method. For the sake of clarity, only the PDF of every tenth iteration is shown.

In comparison to the linear scan, the Bayes experimental design algorithm (see section 2.5.3) provides a more efficient way to collect experimental data. For each iteration of

the measurement, this method permits to calculate the profiling edge position where the information gain is maximal. The result of a typical Bayes-optimised profiling edge measurement is shown in Fig. 4.18. The parameter values for the Bayes fit function are derived by calculating the mean values of the marginal PDFs of the corresponding parameters. This yields $\sigma_x = 7.2 \pm 0.9\,\text{nm}$ for the 1-σ radius and detector efficiency of $a = 0.95 \pm 0.02$. The values determined by the Bayesian method are in principle not independent of the exact sequence of the data points. This is a consequence of the iterative nature of the Bayes fitting procedure by point wise updating. To compare the results with a method which is independent from the order of the data points, the same data is fitted with the maximum likelihood method[82]. This yields $\sigma_x = 7.1 \pm 0.7\,\text{nm}$, and $a = 0.95 \pm 0.02$, where the mean value has a difference of $x_0 = 0.73\,\text{nm}$ compared to the Bayes method. The change of the marginalised PDF for the beam radius σ_x while the iteration proceeds is shown in Fig. 4.18 b). The discrepancy in the beam radius between the linear and the Bayes measurement is attributed to the hysteresis of the piezo, when driving back and forth using the Bayes method. A more detailed discussion of the different contributions to the focal radius can be found in section 4.3.5. A similar measurement performed with sympathetically cooled Nitrogen molecular ions results in a resolution of $92.7 \pm 25.2\,\text{nm}$.

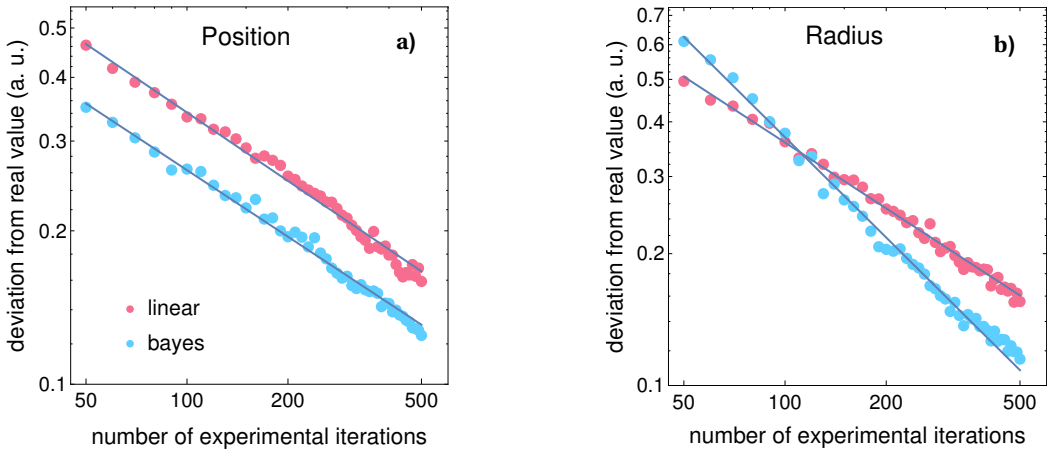

Figure 4.19.: Comparison of the Bayesian and the linear method by numerical simulations. The log-log plot depicts the average deviation of the simulation results from the real value as a function of the number of iterations with the Bayes (blue) and linear (purple) method. The advantage of the Bayes over the linear method scales multiplicative with respect to the number of experimental iterations when measuring the beam position **a)** and exponential when measuring the beam radius **b)**.

To compare the linear method with the Bayesian method, numerical simulations of both approaches were implemented and the average deviation of the simulation outcomes from the real values as a function of the number of iterations n are calculated. The results are depicted in Fig. 4.19. For each data point the deviation is calculated from the results of

[82] This is only true if the measured parameters are independent of the order of the data points. For parameters drifting in time, this condition is not fulfilled.

1000 independent simulation runs, where the initial parameters of the real value and the initial guess of the Gaussian prior are randomised. By fitting the simulated data points, a multiplicative speed up of a factor of about $4/3$ is found, in determining the beam-position, whereas an exponential speed up from $n^{-0.5}$ to $n^{-0.76}$ is found in determining the radius, when comparing the Bayesian method with the linear method.

4.3.4. Measurement of the two-sample deviation

The long-term stability of the focus position and beam focus is an essential prerequisite for high resolution imaging and ion implantation. It can be assessed by evaluating the two-sample deviation of the lateral position (see Fig. 4.20 a)) and the radius (see Fig. 4.20 b)) of the focus (see section 2.5.2). To this end, 2048 linear profiling edge measurements,

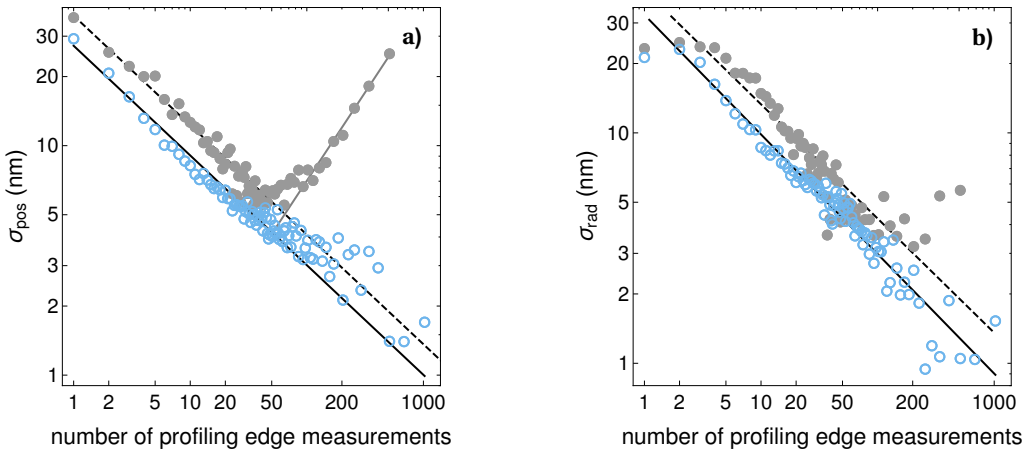

Figure 4.20.: Log-log plot of the two-sample deviation of the beam position **a)** and the beam radius **b)**. The blue circles show the measurement data obtained under best conditions. For comparison, the results of the same measurement under less stable conditions are depicted by the grey dots. For the position they show a drift after about $n = 50$ measurements. The black line is drawn according to the results of a fit to the data obtained under best conditions. The integration time for $n = 10$ is about 5 minutes, for $n = 100$ it is about one hour.

similar to those in Fig. 4.17, were carried out repetitively. Every measurement comprises 26 contiguous profiling edge positions separated by 10 nm, each probed with a single ion. In total the data set thus contains 53,248 extraction events within an acquisition time of 18 hours. The two-sample deviation is given by equation (2.70), thus the variance reads

$$\sigma^2(n) = \frac{1}{2(N-1)} \sum_{i=0}^{N-1} \left(\bar{x}_{i+1}(n) - \bar{x}_i(n)\right)^2 ,$$

where $\bar{x}_i(n)$ is the mean value for the i-th segment, which is derived from fitting to the aggregate count data from n consecutive profiling edge measurements.

If the measurements are dominated by statistical fluctuations rather than beam pointing drifts, the two-sample deviation scales as $1/\sqrt{n}$. Under stable thermal and constant

trapping conditions[83], a fit to the beam position deviations (blue circles in Fig. 4.20 a) and the beam radius deviation (blue circles in Fig. 4.20 b)) indeed reveal a slope of -0.48 ± 0.01 and -0.52 ± 0.01, respectively. This demonstrates the long-term stability of the ion beam over the entire integration time of about nine hours. The minimal two-sample deviation of the beam position yields a long-term beam-pointing stability of around 1.5 nm, where the minimal two-sample deviation of the beam radius is determined to be in the order of 1 nm.

4.3.5. Measurement of the beam waist

In order to determine the waist function, several profiling measurements in x direction yielding the beam radius are performed along the z-axis of the beam (Fig. 4.21). Subse-

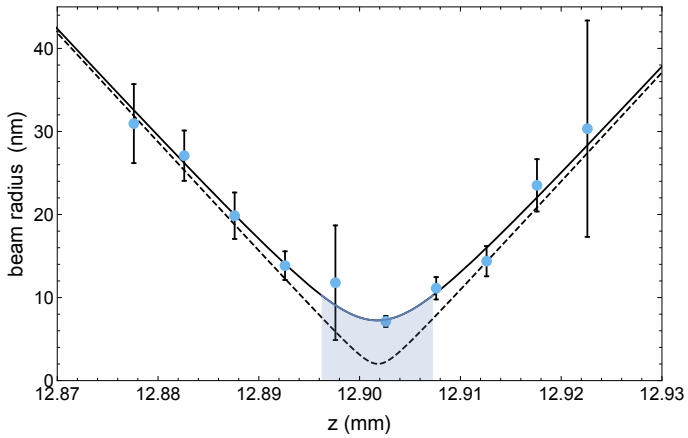

Figure 4.21.: The 1-σ beam radius dependence along the beam axis (blue dots), around the Gaussian image plane of the lens. The error bars are obtained from the standard deviation of the probability density function from the Bayesian experimental design method. The data (in total roughly 2 h data acquisition, about 5,000 ions) is fitted with equation (2.39) (solid line). The blue area indicates the depth of focus. The dashed line shows the same function (2.39) assuming a source size of $\sigma_r = \sigma_x = 51.96$ nm as obtained from the measurements in 4.1.3.

quently the data is fitted by the function (2.39)

$$w(S_2) = \sqrt{\left(S_1 + S_2 - \frac{S_1 S_2}{f}\right)^2 \sigma_\alpha^2 + \left(1 - \frac{S_2}{f}\right)^2 \sigma_r^2},$$

where $S_2 = z$ denotes the position along the extraction axis and $S_1 = 332.2$ mm the distance between source and principal plane of the lens. For the remaining free parameters the fit reveals a beam divergence of $\sigma_\alpha = 51.0 \pm 1.6$ µrad, a source radius of $\sigma_r = 187 \pm 16$ nm and a focal length of $f = 12.4195 \pm 0.0003$ mm. This model does not take lens errors into account as the aggregation of all lens errors is small compared to the measured

[83] The calcium oven is continuously switched on and the use of a titanium sublimation pump is avoided. The radio frequency-drive and all lasers are continuously working under load conditions.

minimal focus. The contributions of different lens errors are discussed in detail further below. For the same reason the broadening of the focus by electrical noise on the deflection electrodes is neglected (compare 4.2.4). Also neglected is the error contribution of the piezo, which, according to the data sheet, amounts to 1 nm. The focal radius resulting from the minimum of the fitted waist function (see Fig. 4.21) equals 7.3 ± 1.0 nm at a distance of $S_2 = 12.90$ mm. From this, the magnification can be calculated yielding $M = S_2/S_1 = 0.039$. The depth of focus, defined by the distance between the positions along the optical axis where the radius of the beam equals $\sqrt{2}$ times the focal radius, amounts to 11.0 µm.

The immediate beam divergence of the source is fully consistent with a value of 44.7 ± 13.4 µrad divergence, as measured independently without the focusing lens (see section 4.2.3). The value of the effective source radius σ_r of about 200 nm is well above the single ion wave packet size of about 50 nm as derived from the resolved sideband spectroscopy measurements (4.1.3). This discrepancy is attributed to mechanical vibrations which move the source with respect to the lens increasing the effective source size.

Applying the model function for the waist size and assuming a 50 nm source radius, which corresponds to an ion after Doppler cooling without any additional source point fluctuations (see 4.1.3), results in a calculated focal radius of 2.02 nm over a 3 µm depth of focus (dashed line in Fig. 4.21). This result is supported by classical numerical trajectory Monte-Carlo simulations [Sin10] predicting the same focal radius.

error source	eq.	theo. expectation (nm)	
		min.	typical
source size	(2.40)	2.02 ± 0.02	2.02 ± 0.02
spherical aberration	(2.45)	0.26 ± 0.08	1.73 ± 1.55
axial chromatic aberration	(2.50)	0.30 ± 0.03	0.57 ± 0.17
radial chromatic aberration	(2.51)	0.002	0.002
total		2.33	3.22

Table 4.3.: List of errors and their minimal contributions to the 1-σ beam radius of the focus. The total balance is derived by quadratic addition of the errors as a function of the position along the axis and subsequently calculating the minimum from the resulting function with respect to this position (see Fig. 4.22).

Table 4.3 shows a list of contributions to the focal radius, itemised according to their cause, using the 1-σ source size $\sigma_r = \sigma_x = 51.96$ nm obtained in 4.1.3, the measured beam divergence, either the minimal value $\sigma_\alpha = 23.7$ µrad or the typical value $\sigma_\alpha = 44.7$ µrad from 4.2.3, the coefficient of spherical aberration $c_2 = 2.57\,\mathrm{mm}^{-1}$ determined in 4.3.1 and the energy as well as its dispersion from 4.2.2.

The contributions from different sources to the minimal focal radius as a function of the distance to the lens z are shown in Fig. 4.22.

With additional sidebandcooling the phonon numbers of the radial modes were reduced to $n = 2.2$ phonons and $n = 1.2$ phonons, which corresponds to a source size 16.1 nm

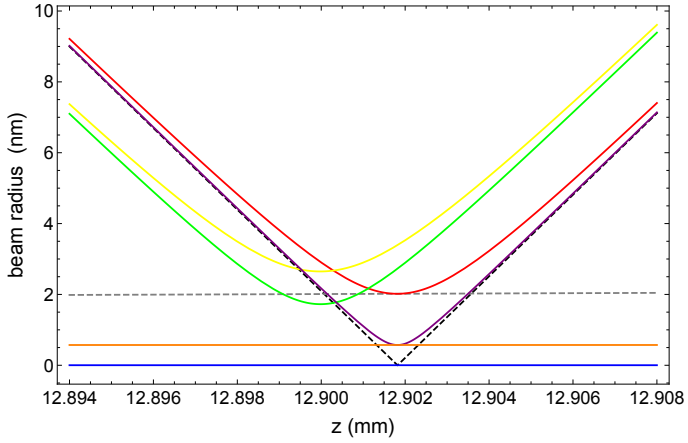

Figure 4.22.: Different contributions to the focus in terms of 1-σ beam radius as a function of the distance along the axis z. The dashed black line shows a focussed point source with a 1-sigma beam divergence σ_α, the dashed gray line is the 1-σ beam radius of a collimated beam of a source with size σ_r, and the red line depicts the combination of both, namely the focus of a extended source with size σ_r and emission angle σ_α. The focus of a point source under spherical aberration is shifted towards the lens (green). The yellow line shows the combined extended source under spherical aberration. The offset introduced by axial chromatic aberration (orange), increases the focus of a point source (purple). For comparison, the offset resulting from the radial chromatic aberration (blue).

and 11.3 nm respectively (compare 4.1.3). However, as a result no reduction of the focal size was observed. This coincides with the previous findings, that already in the Doppler cooled case the focal size is not limited by the source size.

5. Transmission microscopy with single ions

The subject of this chapter is the implementation of a single particle microscope by using an ion source which provides deterministic emission properties. This offers an advantage over microscopy with conventional particle sources - in particular, a higher signal-to-noise ratio (SNR), especially at ultimate low exposures and thus, a higher information gain per particle, which can be increased even further, when combined with the Bayes experimental design method.

For ion implantation, imaging of the sample substrate as a fault tolerant method for referencing of the impact site relative to structures or markers already in place, is a crucial prerequisite. If these are transmissive structures, such as the edge of the substrate or a marker hole, this referencing can be achieved by simply using the implantation beam for imaging. Depending on the application, it may be necessary to use a different ion species for the imaging to avoid contamination of the sample.

5.1. Imaging with a single ion source

In conventional electron or ion microscopy, the SNR can typically be improved by increasing the the particle exposure. This is a direct consequence of the probabilistic nature of the sources in use, which are subject to Poissonian counting statistics. However, a high particle dose may be detrimental in some applications where, for example, high irradiation causes charging, contamination or even damage to sample substrates. By using a deterministic source the SNR is in principle independent of the particle flux, eventually resulting in *noiseless* imaging and therefore requiring an exposure of only a single particle to probe for transmission. However, in combination with a detector of finite quantum efficiency, the counting statistics become *binomial*. This still leads to inherently more information per particle and thus higher SNR than would be possible with Poissonian statistics. Moreover, when gating the detection by the extraction event, the detector dark counts can be suppressed by six orders of magnitude. In combination with the Bayes experimental design method, a deterministic source can be used to maximise the spatial information gained when imaging transmissive structures with a parametrisable transmission function.

5.1.1. Imaging protocol

The imaging protocol is shown in Fig. 5.1. It consists of several preparatory steps and the microscopy loop. The former comprises micromotion compensation as well as beam

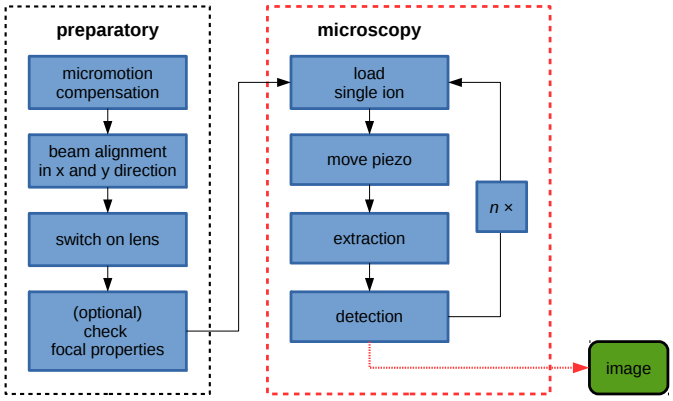

Figure 5.1.: A flowchart of the microscopy protocol, separated into preparatory steps and the microscopy protocol.

alignment. The latter is fully automatised. It consists in loading of a single calcium ion, moving the sample to the position for the next probing, the actual probing for transmission which includes extraction and focussing of the ion to that position, and the detection as well as the storage of the detection result. This process is repeated for each probing position, which eventually correspond to the pixels of the resulting image.

5.1.2. Imaging results

The imaging of transmissive structures is demonstrated by scanning a photonic waveguide-cavity fabricated from diamond (see Fig. 5.2). The sample has a thickness of $300\,\mathrm{nm}$ and was prepared in the group of C. Becher in Saarbrücken, using a Ga^+ ion FIB [RM12]. Fig. 5.2 a) shows a large-area view of the diamond substrate comprising three of these structures. A close-up SEM image of the structure located in the lower right corner is shown in Fig. 5.2 b).

For acquisition of Fig. 5.2 c) each pixel was probed with exactly one ion. The detector was gated by the extraction event with a gate-time of $200\,\mathrm{ns}$. This ensures that the dark count rate of typically less than $100\,s^{-1}$ does not affect the image contrast. Whereas the contrast in the transmissive areas is assumed to be limited solely by the detector efficiency, and hence is showing binomial counting statistics. The detector efficiency was measured to be $96 \pm 2\,\%$. Other influences such as background gas collisions are considered to be negligible. At the edges of the structure *i.e.* between transmissive and non-transmissive parts, the contrast is dominated by the finite beam radius (compare 4.3.3). To contrast the imaging properties of the deterministic with a Poissonian source, Fig. 5.2 d) shows the same structure, but imaged with an experimentally emulated Poissonian source: Prior to the probing of each pixel, the number of ions to be extracted is obtained using a random number generator with a Poisson-distributed output, where the mean value is set to one.

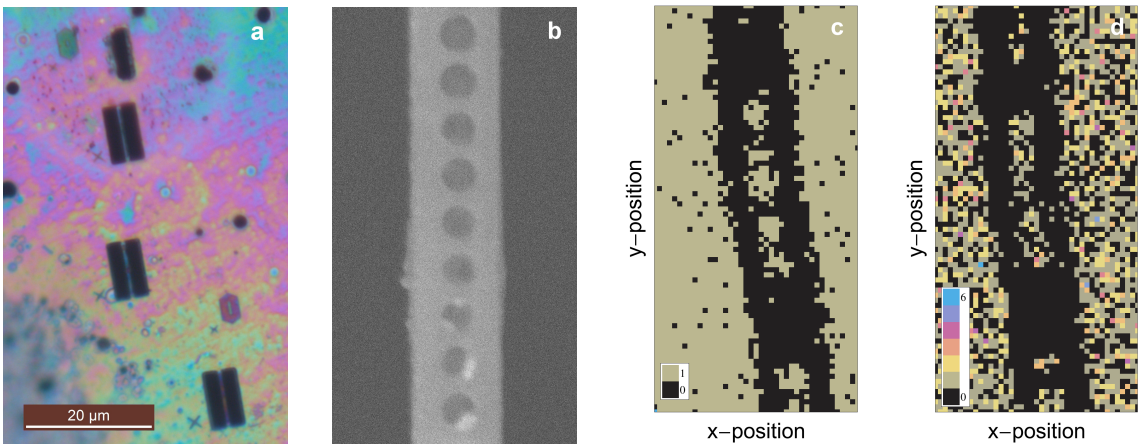

Figure 5.2.: Imaging a transmissive diamond sample: a) A large-area view of the transmissive cavity structures (black) in the diamond sample [RM12], imaged with a conventional optical microscope. The structure shown in (b), (c) and (d) is located in the lower right corner. b) SEM image of the waveguide-cavity structure. The holes have a diameter of about 150 nm. c) The cavity structure is scanned using one ion at each lateral position, with a resolution of (25x25) nm^2 per pixel. The entire information in the picture is based on 2659 transmission events out of 4141 extracted ions. d) The same structure as imaged in (c) using a source with emulated Poissonian behaviour. The lower SNR as compared to (c) is clearly visible. The missing holes compared to the image in (b) are attributed to blind holes. Here the image is based on 2420 transmission events out of 3694 extracted ions.

5.1.3. Discussion

A quantitative comparison of the two types of sources is presented in Fig. 5.3. The SNR calculated as a function of the mean number of extracted ions is compared for different detection probabilities a. Note that the dark count noise is not taken into account in this comparison. This is justified by the aforementioned circumstance that the detector signal of both sources - the deterministic and the emulated Poissonian - is gated. For the plot the definition $\mathrm{SNR} = \mu/\sigma$ is used, where μ is the mean value and σ the standard deviation of the corresponding probability mass function.

In general this means, compared with a Poissonian source with flux Θ_{Pois}, a deterministic source requires a flux of only $\Theta_{\mathrm{det}} = \Theta_{\mathrm{Pois}}\,(1-a)$ to achieve the same SNR, where a is the efficiency of the detector, considering the same exposure time. For the deterministic microscope at hand, with a detector efficiency of 0.96, the same SNR as a corresponding microscope with a Poissonian source can be achieved with only $4\,\%$ of the flux.

5.2. Microscopy using the Bayes experimental design method

With a deterministic source, the Bayes experimental design method can be used to image structures with a parametrisable transmission function with optimal efficiency. For each

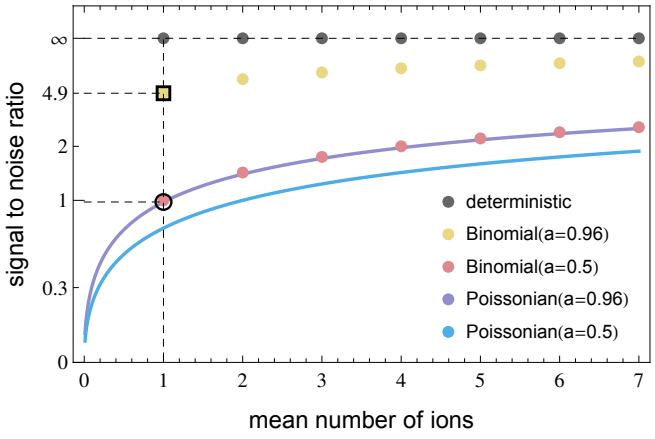

Figure 5.3.: Calculated SNR of a binomial and a Poissonian source plotted as a function of the mean number of extracted ions for different detector efficiencies. The scale on the y-axis is compactified by the function $f/(f+1)$. Note that the SNR for binomial statistics with $a = 0.5$ is identical to the Poissonian SNR with $a = 1$. The square and the circle depict the operating points of the detector-efficiency-limited deterministic source (as in Fig. 5.2 c) and the emulated source (as in Fig. 5.2 d) respectively. In both cases the mean number of extracted ions per pixel is one and the detector efficiency is 0.96. This results in an SNR of 4.90 for the deterministic source and an SNR of 0.96 for the emulated Poissonian source.

probing event, the algorithm optimises the probing position for maximal information gain. The parameters values are then determined by incorporating the resulting information, using the Bayesian update rule. Here, this method is used to experimentally demonstrate finding and measuring the lateral position of a circular hole.

5.2.1. Bayes imaging results

The measurement of parameter values of two-dimensional transmissive structures with a parametrisable transmission function is demonstrated by means of a circular hole in a diamond sample (see Fig. 5.4). This is also a practical example for sample alignment, since for many applications, such as the deposition of dopants, it is useful to know the exact lateral position of a sample with respect to the beam focus. For this purpose two perpendicular profiling edges as used in the previous example could equally be employed. However, for practical reasons, it might be more convenient to use a simple hole structure as a marker, which is in close proximity to the area of interest.

For comparison with the Bayes approach, the hole structure is first scanned with a linear sequence, using 1332 ions in total, where each lateral position is probed with one ion. A maximum likelihood fit to the data yields an precision of $\Delta x = 47.1\,\mathrm{nm}$ and $\Delta y = 22.6\,\mathrm{nm}$ for the position, where the radius was extracted to be $r = 1057 \pm 32\,\mathrm{nm}$.

Now, the same hole is imaged using the Bayes approach. First, the structure is parametrised by a 5-parameter probability function from which 2 parameters are set

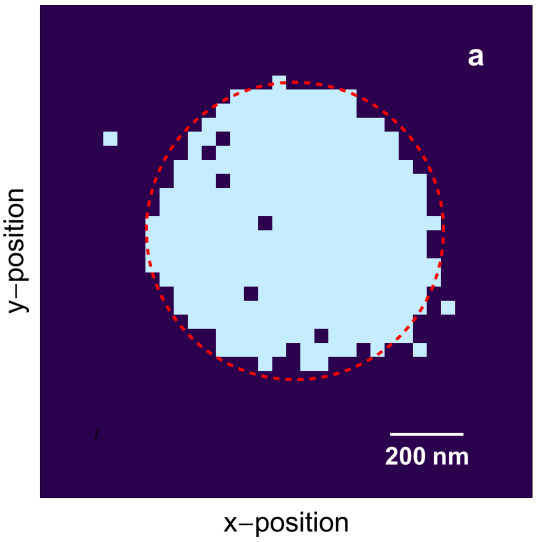

Figure 5.4.: Determination of alignment-hole parameters with linear scan: A circular hole structure is scanned using one ion at each lateral position, with a resolution of (100x100) nm^2 per pixel. The red circle shows the result of a maximum likelihood fit to the data.

to be constant to reduce the computational effort. It consists of the lateral position of the centre of the circular hole, its radius as well as the 1-σ radius of the ion beam and the detector efficiency. The parameters radius of the beam and detector efficiency are set to be constant at $25\,\mathrm{nm}$ and $95\,\%$, respectively. Both values had been determined before and are assumed to be stable during the experiment, since the ion energy, lens voltages, and other parameters of the experiments are kept the same.

Using 379 ions in total, the position is determined with an precision of $\Delta x = 2.7\,\mathrm{nm}$ and $\Delta y = 2.1\,\mathrm{nm}$, where the radius converges to $r = 1004 \pm 2\,\mathrm{nm}$ (see Fig. 5.5 and 5.6). Compared to the linear scan, the precision, thus, is about one order of magnitude higher when determining the hole position even though, less than $30\,\%$ of ions have been used. Certainly, the Bayes approach is based on the assumption of a circular hole which may not be perfectly valid. The systematic errors resulting from the deviations of the real shape to the parametrisation (ideal circle) are difficult to quantify, since the precise extent of this deviation is unknown. However, the method may be easily adapted to elliptical distortions of the marker holes, or rectangular shaped markers on the substrate.

Although this means a strict comparison in terms of precision per probe event is difficult, it can be concluded that the average information gain per probe event provided by the Bayes method is significantly higher due to more targeted probing, and therefore, a significant reduction in exposure and measurement duration can be achieved using the Bayes method instead of a linear sequence scan of the same area.

As indicated above, in the case of ion implantation where absolute positioning is necessary, transmissive structures can be used for referencing. Imaging these markers

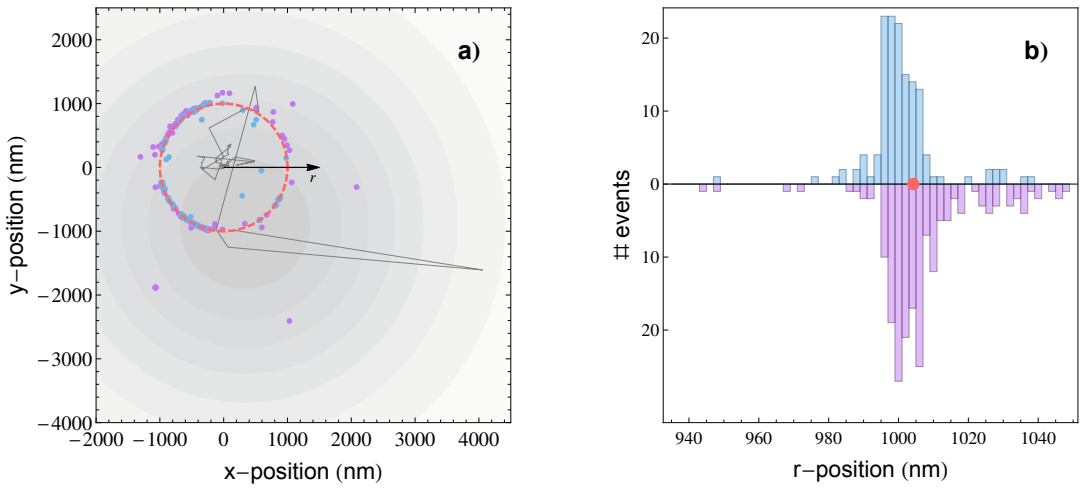

Figure 5.5.: a) Determination of alignment-hole parameters with the Bayes method. For the plot the x and y position of the hole were set to zero. The blue and red dots represent the positions where an ion was, or was not, detected, respectively. The final location and radius of the hole structure is depicted by the dashed red circle. The initial guess of the Gaussian shaped PDF for the position is depicted as a gray shade in the background. The dark gray line follows the progression of its mean value *i.e.* the assumed centre position of this distribution as a function of the number of extracted ions. Within the first four iterations no ion is transmitted. The spatial information of these blocked particles shifts the assumed position, since it excludes that specific areas are transmissive. After the first ion is transmitted the assumed position makes a step towards its location. b) A histogram of detected and not detected events dependent on r the distance to the centre of the structure. The red point depicts the measured radius.

with the same source which is used for the implantation, allows for the accurate alignment of dopants relative to this markers, free of parallax errors. Depending on the application, it can be necessary to use a different ion species for the imaging to avoid contamination of the sample. For this purpose, it has to be considered that the energy of the different species remain the same, in order to avoid different spatial positions of the beam focus as a result of inconsistent deflection. An example application, where such an alignment is used is presented in Section 6 *Implantation with single ions*.

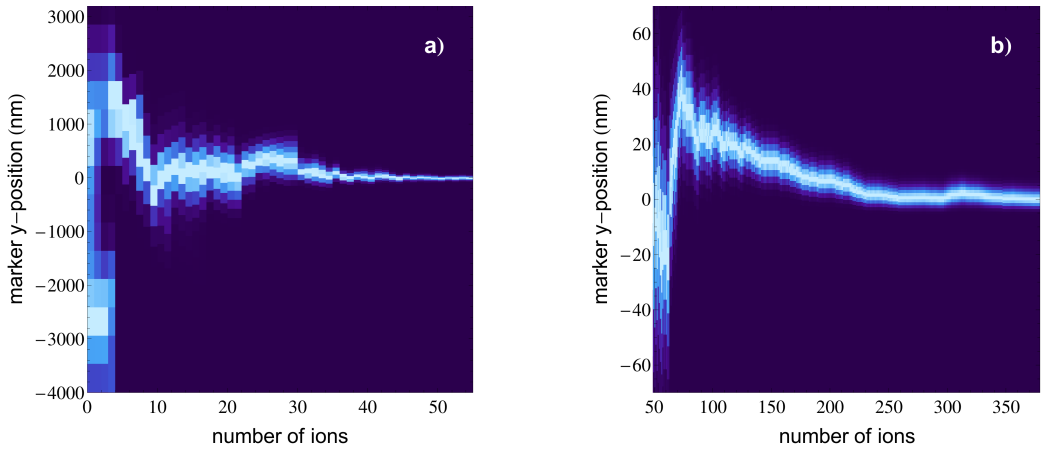

Figure 5.6.: Plot of the marginal PDF for the y coordinate of the circle as a function of the number of ions. **a)** Shows the evolution of the marginal PDF for the first 50 ions. With the first transmitted ion (at the 5th), the width of the PDF collapses, because the position of the structure is now known to its assumed radius. **b)** shows a zoom to the region around the final value staring from ion number 50.

6. Implantation with single ions

The experimental apparatus with the single ion source, was predominantly designed for the purpose of deterministic single ion implantation on the nanometer scale. This may allow for the fabrication of scalable solid state quantum devices, where individual dopants are coupled by their mutual dipolar magnetic interaction. The focus of this experiment is on systems of coupled nitrogen vacancy (NV) colour centres [Dol13], coupled single phosphorous nuclear spins in silicon [Kan98, Don10, Pla12, Vel15] and cerium or praseodymium in yttrium orthosilicate (YSO) [Kol12]. Yet another promising application of such a focussed deterministic single ion beam is the doping and structuring of graphene [Kot15].

Verifying implantation into solid state substrates is a relatively hard task, because of the difficulty of detecting single atoms within such a solid. For this reason, the creation of colour centres by single ion implantation is demonstrated, since their favourable scattering rate allows for a detection of single centres with a confocal microscope. The different colour centres considered were NV colour centres in diamond, and cerium or praseodymium in YSO. The decision was in favour of nitrogen, as it can be loaded to the trap by means of the ion gun (compare 4.1.4) and it has a favourable charge to mass ratio with regard to sympatetic cooling via calcium. In the following the full production chain is demonstrated, starting with an undoped ultra pure diamond crystal, the implantation of a pattern of N_2^+ ions of a specific isotope (^{15}N), annealing of the diamond sample, and finally the detection of NV centres which have been formed.

However, this method shows a low yield of around $0.5\,\%$ [Pez10] when creating colour centres at impact energies of $> 10\,\mathrm{kV}$ which are currently accessible by the experiment. Going to higher energies, on the other hand, would cause straggling of the ions on their way though the diamond lattice, deteriorating the resolution for which the apparatus was designed for. For this reason, the creation of NV centres in diamond with the expected yield can serve as a case example which proves the functionality of the method.

6.1. Implantation protocol

For performing the implantation, an additional step is required in comparison to the procedure of trapping, cooling and extraction of the nitrogen molecular ions described in section 4.1.4 *Trapping and sympathetic cooling of N_2* and 4.3.3 *Measurement of the beam focus*, namely the sample has to be aligned with respect to the beam. To this aim, the perpendicular edges of the diamond substrate are used to perform a beam focus measurement, similar to the experiment in 4.3.3. This yields the position of the edges with respect to the beam focus in x, y and z direction, providing a reference for the subsequent implantation.

These measurements are conducted with calcium, rather than nitrogen in order to avoid contamination of the sample. Fig. 6.1 shows the entire implantation protocol: First, the

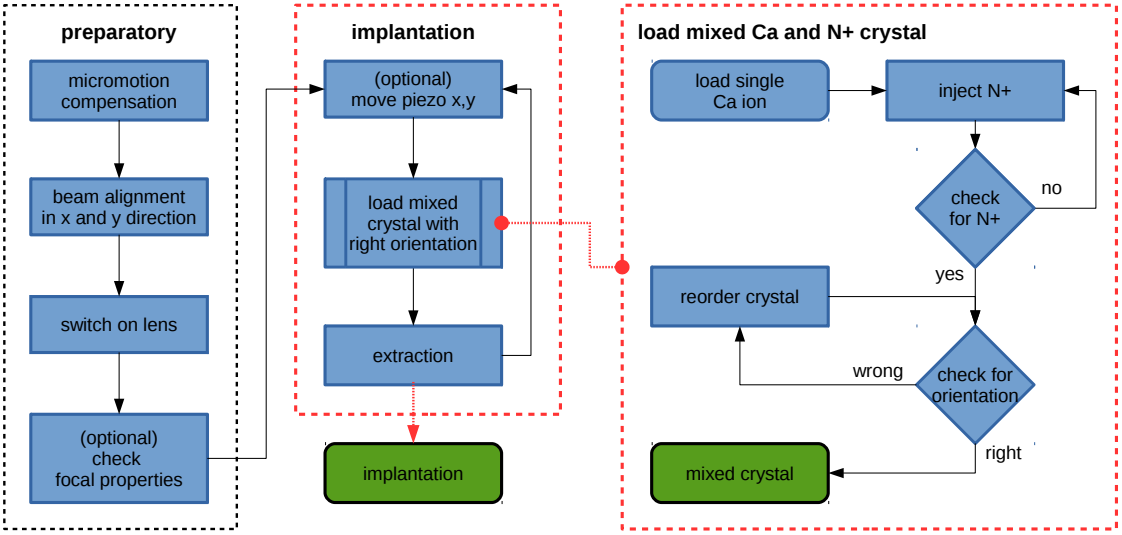

Figure 6.1.: A flowchart of the implantation protocol, separated into preparatory steps and the implantation protocol. A detailed chart of the loading of mixed ion crystals is shown seperately on the right hand side.

source is prepared by micromotion compensation and alignment of the ion beam to the lens, where optionally the focal properties of the beam can be checked. Subsequently, the target substrate is aligned with respect to the beam as described above. Finally, the actual implantation process is started, consisting in repetitively extracting and focusing single ions onto the target substrate with respect to the previously determined references. Depending on the type of implantation *i.e.* all dopants are implanted into one spot, or alternatively into a spatial arrangement where the position of the target substrate is moved between the extractions.

6.2. Implantation results

To demonstrate the feasibility of the implantation method, an array of 5×5 spots with 20 molecular ions each, is implanted $70\,\mu m$ away from the two edges of one corner of the sample substrate[84]. Prior to the implantation, this area was carefully checked to contain no NV^--centres. Note that all following steps were performed by C. Osterkamp from the group of Fedor Jelezko at the University of Ulm. After implantation, the sample substrate is annealed for two hours at $800°$ C. This procedure permits a diffusion of the vacancies which were created by the implantation, whereby they eventually attach to a nitrogen atom and form a NV colour centre. However, it is a reasonable assumption that during this process, most of the vacancies can escape to the surface, due to the shallow penetration

[84] Electronic grade diamond (1 ppb N), Element Six Ltd, Harwell Oxford, UK

depth of about 7 nm at which the ions come to rest when using an energy of 3 keV per single nitrogen. Additionally, is has been conjectured that diffusion of hydrogen might shift the Fermi level and lead to neutral NV centres. In addition, surface quality and charge traps are expected to affect shallow implanted NV most [Ost13].

Following the annealing procedure, the implanted area of the sample diamond is investigated under a confocal microscope using laser light at 532 nm. Thereby, a microscope objective focusses the light onto the diamond surface where it excites fluorescence of the colour centres. Lateral scanning of the focus while simultaneously collecting and measuring the fluorescence light with the confocal microscope allows for spatial imaging. Fig. 6.2 shows the result of such an imaging scan of the diamond sample implanted with nitrogen. Overall, 6 NV colour centres out of 500 implanted molecular nitrogen ions

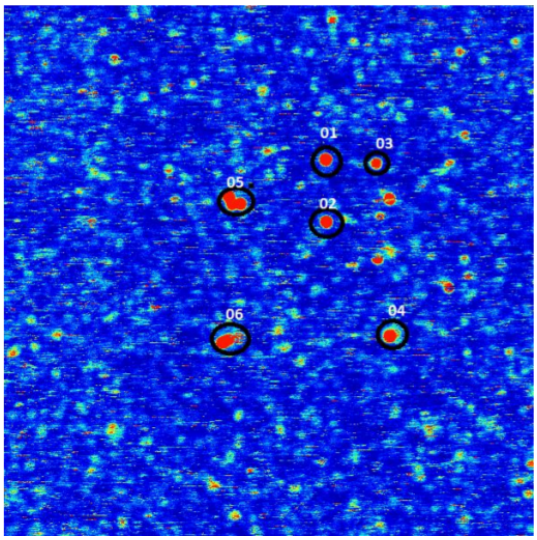

Figure 6.2.: Fluorescence image of the implanted nitrogen vacancies as acquired with the confocal microscope. The image was made by Christian Osterkamp at the University of Ulm.

were created. This makes a total of 1000 nitrogen doping atoms, resulting in a yield of $0.60 \pm 0.02\,\%$. For all centres fluorescence spectra were taken, indicating that 3 of them are in the NV^- charge state and the others are NV^0.

7. Conclusion and outlook

7.1. Conclusion

In this work, a deterministic ion source was implemented by extracting single laser cooled $^{40}Ca^{+}$ ions from a linear segmented Paul trap, at energies ranging from $300\,\mathrm{eV}$ to $5.9\,\mathrm{keV}$. First, the characteristics of this source were measured: The energy dispersion was determined to be $119\,\mathrm{meV}$ and $174\,\mathrm{meV}$, when extracting with one switch or two high voltage switches, respectively. Moreover, this value was found to be solely limited by the electrical noise of these switches. The emittance of the beam was deduced from spectroscopic temperature measurements to be $1.69 \cdot 10^{-22}\,\mathrm{m^2\,rad^2\,eV}$ for Doppler cooled ions and $2.60 \cdot 10^{-24}\,\mathrm{m^2\,rad^2\,eV}$ for sideband cooled ions. The beam divergence was measured to be $23.7\,\mathrm{\mu rad}$. Secondly, the beam consisting of singly extracted ions, was focused to a 1-σ spot radius of $5.8\,\mathrm{nm}$, over a $11\,\mathrm{\mu m}$ depth of focus and a position stability of about $1.5\,\mathrm{nm}$ over 9 hours.

The focussed beam was used successfully to perform transmission microscopy with single ions. Furthermore, it was shown how this microscopy benefits from the unique statistical properties of the single ion source in two different ways. On the one hand, the deterministic source in combination with a detector of finite quantum efficiency exhibits binomial noise characteristics which provides better SNR when compared to conventional Poissonian sources. Additionally, the deterministic property permits imaging with negligible dark counts when gating the detector signal with respect to the extraction event. On the other hand, it is demonstrated that the gain per particle in spatial information can be maximised by using the Bayesian experimental design method, in cases where additional topological information about the imaged structures is available. The high SNR and the optimisation measures presented here are clearly not the only factors to determine how fast an image with a certain contrast can be acquired, since this strongly depends on the repetition rate *i.e.* the ion current. However, the approach at hand is suitable for applications where the acceptable current is limited, for example due to insulating, very pure, or fragile samples which would otherwise suffer from charging, contamination, or damage from radiation, respectively.

In the context of this thesis, the applicability of the deterministic source for single ion implantation was also demonstrated. To this goal, molecular nitrogen ions were implanted into a diamond substrate, arranged in an array of 5×5 spots, where each spot consisted of 20 implantations. In total 500 molecular ions were implanted from which 6 turned into NV colour centres, resulting in a yield of $0.6\,\%$.

7.2. Outlook

7.2.1. Source

For future experiments and realisations of similar devices a number of improvements are conceivable. The arrangement with two seperate chamber has turned out to be susceptible to shear vibrations and should be solved differently in further experiments. For his reason, the overall reliability, and also the resolution could be further improved by integrating the presented source into a commercial ion beam column featuring high mechanical stability and better optics, which would help both implantation and microscopy applications. The ultimate goal would be a system solely limited by the source, consisting in ground state cooled ions. Fig. 7.1 provides a plot of temperature $\sqrt{k_\mathrm{B}T/2}$ versus the source size σ_x comparing different sources in terms of emittance $\epsilon = \sigma_x\sqrt{k_\mathrm{B}T/2}$, where the data for the other sources is taken from [McC16].

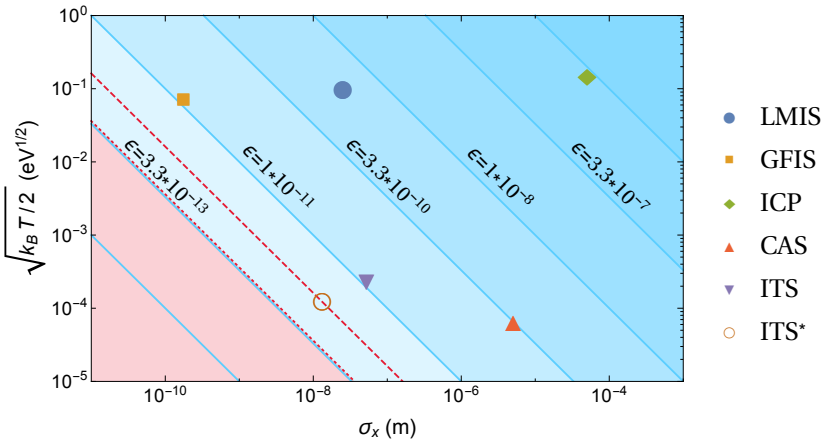

Figure 7.1.: Plot comparing the emittance of different sources types [McC16]. The straight lines indicate constant emittance which is given in (m rad $\sqrt{\mathrm{eV}}$). For calcium the emittance is limited by Heisenberg uncertainty principle to $\epsilon = 3.61 \cdot 10^{-13}$ m rad $\sqrt{\mathrm{eV}}$ (red area on the left bottom side), whereas the red dashed line shows this limit for helium ions (both calculated with equation (2.32)). The comparison includes the liquid metal ion source (LMIS), the gas field ionisation source (GFIS), the inductively coupled plasma (ICP) source, the cold atom source (CAS) and the ion-trap source (ITS). For the latter the source size and temperature from 4.1.3 were used. ITS* shows the emittance of the sideband cooled ions.

In addition divergence of the beam may be minimised. A numerical analysis of the extraction process yielded a focussing of the beam at about 1 mm in front of the endcap (compare 4.2.3), implying that the current divergence of the beam is dominated by this effect rather than by the emittance. This means, an optimisation of the extraction process to minimise this focussing could yield a smaller divergence, and therefore further reduction of the spherical aberration as well as a higher depth of focus. There are also no close fundamental limits which prevent one from expanding the energy range of the source, to

both lower and higher extraction energies. Currently, lower energies are limited by the detector in use, which requires energies $> 500\,\mathrm{eV}$, whereas the upper energy limit is set by the dielectric strength of the electrical insulation of the endcaps. The latter could be circumvented using drift tubes for acceleration. Together, these could enable an energy range spanning over several orders of magnitudes, from single eV to tens of keV.

Another highly desirable enhancement is to increase the repetition rate. This could be accomplished by remote loading of the Paul trap with ions from a magneto-optical trap (MOT). In a corresponding experiment [Sag12], in this way, a loading rate of about $125\,\mathrm{s}^{-1}$ was achieved. An even higher loading rate of up to $4 \cdot 10^5\,\mathrm{s}^{-1}$ has been attained by superimposing the MOT directly with the trapping volume of the Paul trap [Cet07]. However, such modifications impose higher demands on the apparatus design as additional laser access is required. A similar option to improve the loading rate might be realised by generating a constantly refilled reservoir of cold trapped ions, from where single ions are shuttled to an extraction site. Using a multi-segmented planar trap, where the extraction is performed perpendicular to the surface could enable one to operate many such reservoirs in parallel. Realising continuous sources by the above-mentioned methods could possibly reach the picoampere regime. A problem of working with a reservoir of trapped ions arises, when combining it with the switching off of the RF drive for extraction, which inevitably clears the trap. This issue could be circumvented by using a symmetric trap drive, making the off switching obsolete. A proposal for a design, which realises a symmetric RF drive with a linear segmented architecture, and at the same time avoiding insulating surfaces close to the trapping volume can be seen in Fig. 7.2.

Implementing a deterministic source with a ion or atom reservoir would probably still require some sort of feedback involving counting of the number of loaded ions by photodetection, where the minimum required time is in the order of $10\,\mu\mathrm{s}$ [Mye08], thus, limiting the repetition rate to $1 \cdot 10^5\,\mathrm{s}^{-1}$. Another way to guarantee the loading of only a single ion from a MOT could be the photoionisation from a Rydberg level, where the dipole blockade mechanism ensures the excitation of only one atom within the focus of an ionisation laser as proposed by [Ate13]. Also combinations of the above mentioned proposals could proof beneficial.

Although brightness is typically a very useful measure to characterise a source, this is not entirely true for deterministic sources. Generally, the phase space volume or the emittance can be reduced by introducing apertures into the beam path. With a deterministic source, however, this would completely destroy the deterministic quality. This means, in the context of a deterministic source the emittance provides a better figure of merit, whereas brightness only makes sense when talking about high currents at small spots as for example required for milling or fast image acquisition. Since the above-mentioned improvements suggest the feasibility of drastically higher repetition rates, Fig. 7.3 shows a plot of the extrapolated brightness as a function of the current.

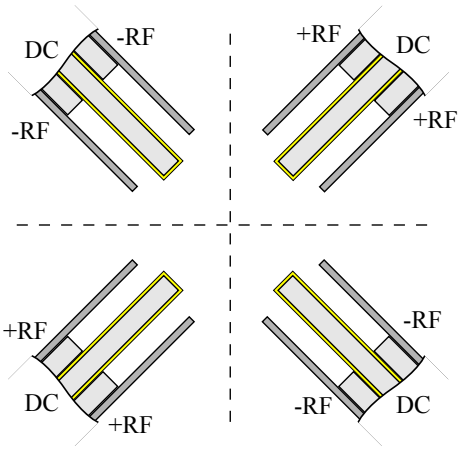

Figure 7.2.: Radial cut trough a segmented, symmetric 3-D trap for ion extraction with endcaps (not shown). The proposal combines the symmetry of the x-shaped arrangement of the trap used in this thesis with the common sandwich design [Sch09b], to allow for a symmetric RF drive. The segmented DC electrodes are gold coated alumina chips (light gray), where the electrode structure is laser milled. The RF electrodes are also gold coated alumina chips or alternatively thin metal sheets (dark gray), which are insulated from the DC chips via spacers of uncoated alumina chips. The sandwich like assembly, thereby, provides low structural complexity and the precise alignment of all components ca be provided by edges on the endcaps (compare Fig. 3.4).

7.2.2. Microscopy

Regarding microscopy applications, a higher repetition rate would permit faster image acquisition and thus promote the practical applicability of the presented microscopy scheme. This could also enable more conventional microscopy applications, such as secondary electron microscopy, secondary ion microscopy and backscattered ion microscopy. For the latter, the low energy range covered by the source at hand could prove beneficial, because the yield of backscattered ions drops with increasing ion energy [McC16]. Furthermore, the regular charge distribution of the beam resulting from the non stochastic nature of the source could help to mitigate the adverse implications of space charges, as they could become relevant when increasing the flux.

Another category of applications could arise from harnessing the TOF information of the ions. Since the ion energy can be directly calculated from the TOF, ion energy loss spectroscopy (IELS) similar to electron loss spectroscopy seams feasible. The resolution, which currently is limited to about $0.1\,\mathrm{eV}$ by noise of the extraction voltage could be improved by using better switches or cascaded extraction including resistive acceleration tubes.

In the context of the above mentioned secondary electron or backscattered ion microscopy, switching and gating of the detector not only could be used to suppress dark-counts but also would allow for higher fields to extract these secondary or backscattered particles and in this way make the detection more efficient. Moreover, the TOF energy

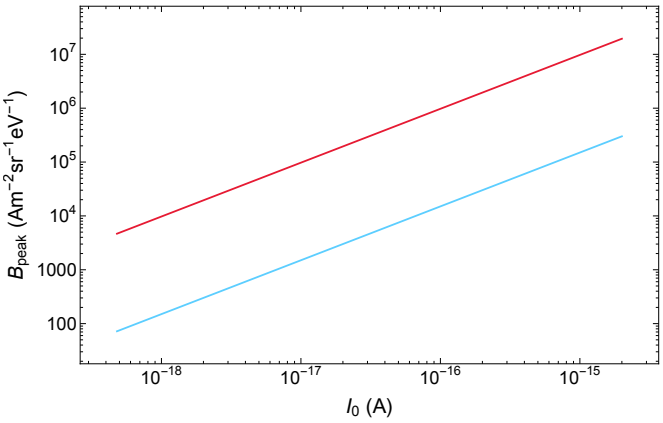

Figure 7.3.: Plot comparing the brightness of the Doppler cooled and sideband-cooled source. Starting with the experimentally obtained value of $4.8 \cdot 10^{-19}$ A on the left hand side, the brightness is extrapolated for higher currents up to the femtoampere regime, which corresponds to a repetition rate of $5 \cdot 10^5\,\mathrm{s}^{-1}$.

analysis could be used to determine the element which was responsible for the scattering [McC16]. With higher repetition rates secondary ion mass spectroscopy (SIMS) would be feasible, where typically the mass of secondary ions sputtered from a target is analysed. To this end, also the TOF information could be used.

For some of these applications it might also be worth considering species lighter compared to calcium, such as beryllium, because they induce less sputtering. Conversely, heavier elements such as ytterbium or even molecules could permit higher resolution imaging as they allow for a smaller emittance, or promote better sputtering for applications such as milling or SIMS.

The temporal control of the ions down to the picosecond regime may also enable ultrafast time resolved microscopy and stroboscopic measurements with ions. Moreover, the TOF information could be used to switch the focusing fields and thus circumvent the resolution-limiting Scherzer-theorem [Sch02, Fic09], which states that a rotationally symmetric ion optical lens with static electromagnetic fields, excluding space charges, always exhibits unavoidable spherical and chromatic aberrations [Sch36].

By means of optical pumping it is possible to implement a fully spin-polarised source, for example to probe magnetic polarisation of surfaces as pioneered in spin-polarised low-energy electron microscopy (SPLEEM) [Dud98]. In a similar experimental scheme, where the sample acts as a electrostatic mirror, the lens could be used to refocus and recapture the backscattered ions and determine the energy loss by the TOF. Alternatively, the accumulated phase of an ion prepared in a spin superposition of the electronic spin state could provide a signal which changes under the influence of the local magnetic field of the sample. A spin-polarised source also could enable Stern-Gerlach type experiments, which up to the present, have never been performed with charged particles.

Ultimately, the combination of control of internal and external degrees of freedom

of the ion could allow for the realisation of matter wave interferometry with single ions [Arn12, Has10].

7.2.3. Implantation

There are also a number of suggestions for improvements of the single ion implantation. A problem with sympathetic cooling when having ions of different mass, is the difference in trap frequency. The higher this difference, the weaker the mutual coupling which accounts for the cooling of the ion which is not directly laser cooled [Wüb12]. An option to improve the sympathetic cooling between ions where the relative mass difference is larger than one, could be to use higher charged ions to achieve a more favourable charge to mass ratio and subsequently better coupling between the ions. For an even higher mass difference, two different trap drive frequencies applied at the same time may be used to match trap frequencies, which in a similar way improves the sympathetic cooling, in order to allow for the cooling of large molecules.

Another application which could become interesting with a higher repetition rate is the deposition of material. If in addition the resolution is improved to the size of the lattice constant of solids, individual ions could deliberately be placed on top of each other, realising a nano-assembler or 3-D printer for single atoms.

A. Design drawing of the trap holder

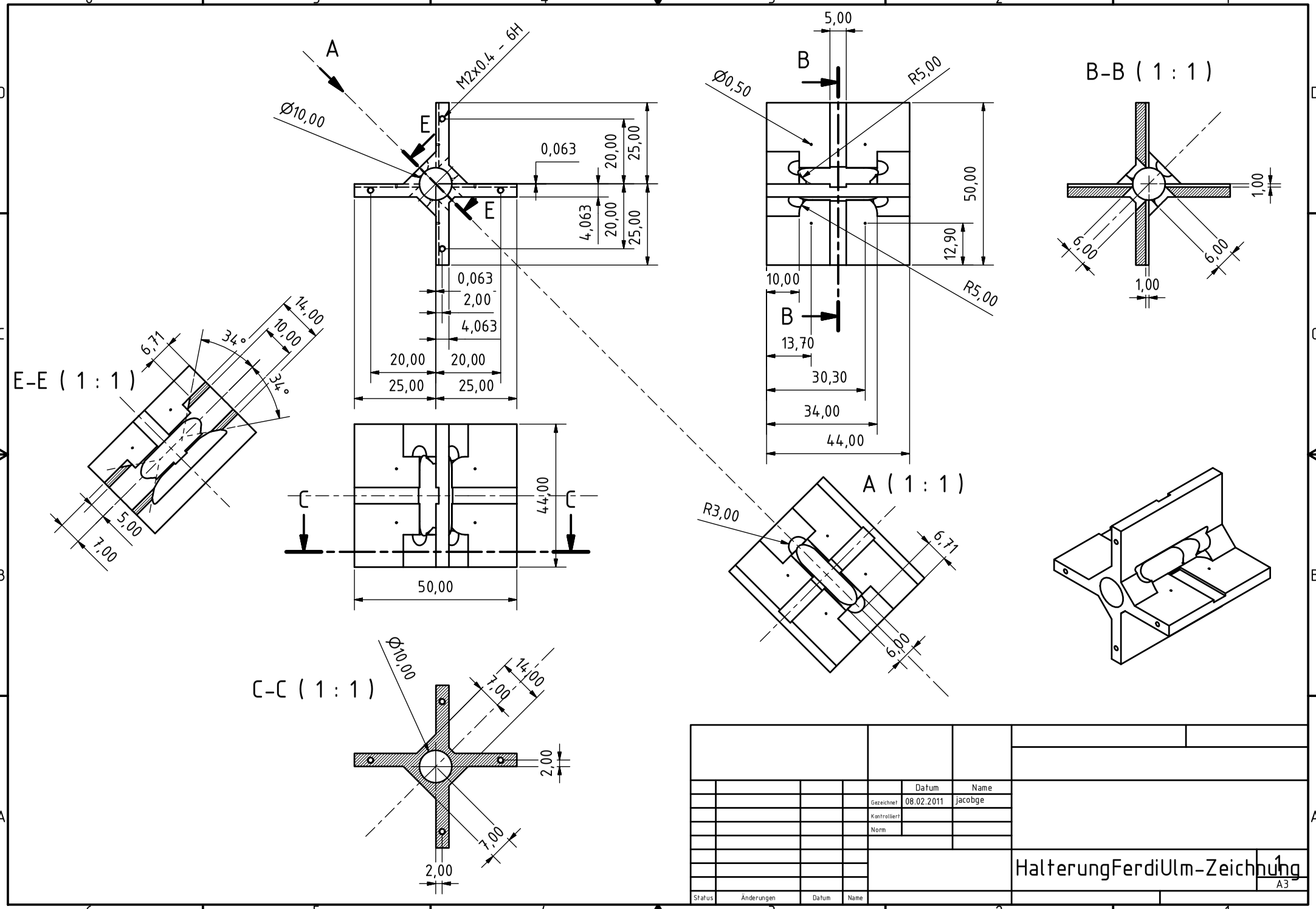
A
M2x0.4 - 6H
Ø10,00
E
E
0,063
20,00
25,00
4,063
20,00
25,00
0,063
2,00
4,063
20,00
20,00
25,00
25,00
44,00
C
C
50,00
E-E (1 : 1)
14,00
10,00
6,71
34°
34°
5,00
7,00
B
B
5,00
R5,00
Ø0,50
50,00
12,90
10,00
R5,00
13,70
30,30
34,00
44,00
B-B (1 : 1)
1,00
6,00
6,00
1,00
A (1 : 1)
R3,00
6,71
6,00
C-C (1 : 1)
Ø10,00
14,00
7,00
2,00
7,00
2,00
Datum
Name
Gezeichnet
08.02.2011
jacobge
Kontrolliert
Norm
HalterungFerdiUlm-Zeichnung
1
A3
Status
Änderungen
Datum
Name

B. Design drawing of the einzel lens

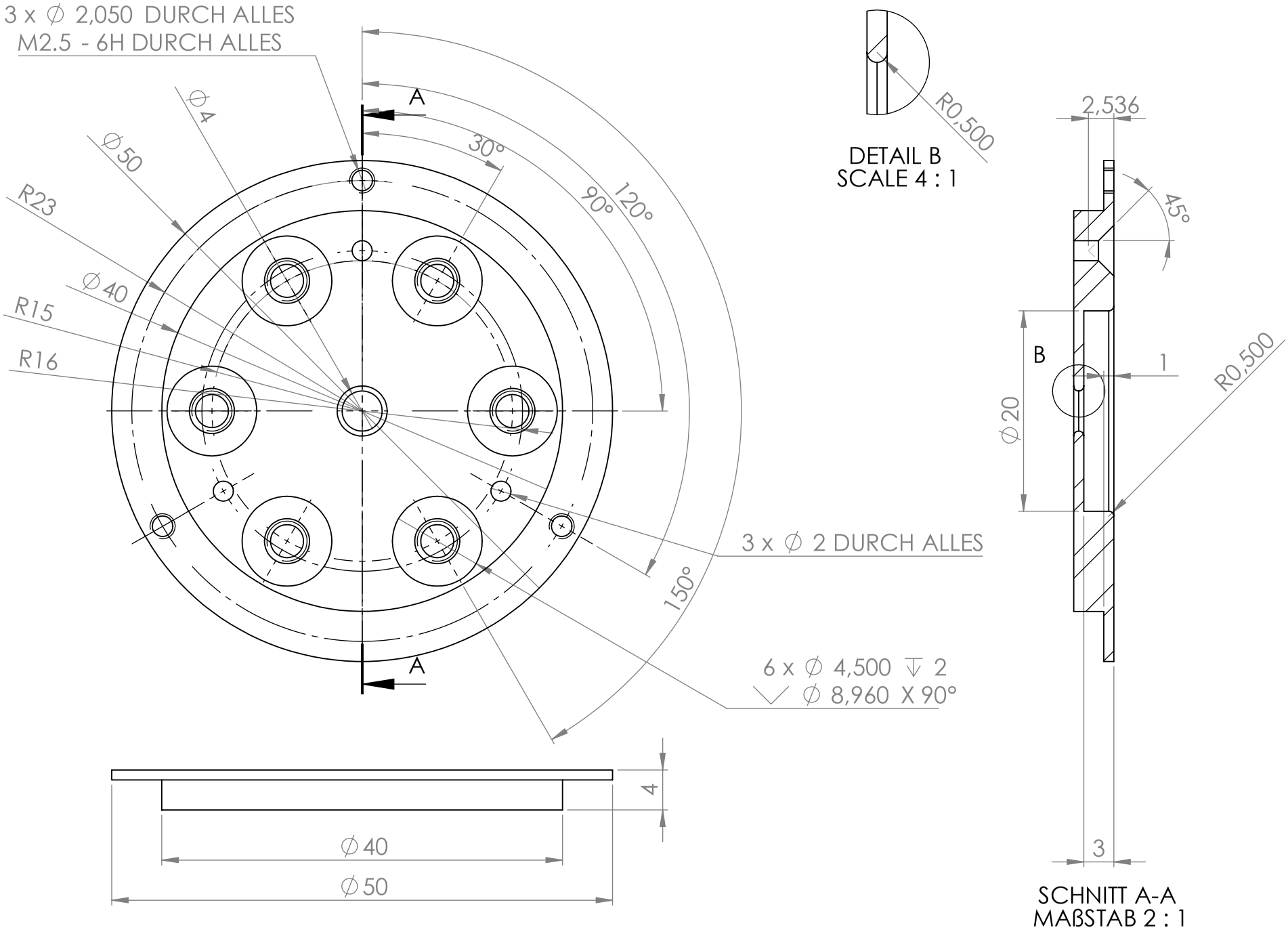
3 x ∅ 2,050 DURCH ALLES
M2.5 - 6H DURCH ALLES
∅4
∅50
R23
∅40
R15
R16
A
30°
90°
120°
150°
3 x ∅ 2 DURCH ALLES
6 x ∅ 4,500 ↧ 2
⌵ ∅ 8,960 X 90°
4
∅40
∅50
DETAIL B
SCALE 4 : 1
R0,500
2,536
45°
B
1
R0,500
∅20
3
SCHNITT A-A
MAßSTAB 2 : 1

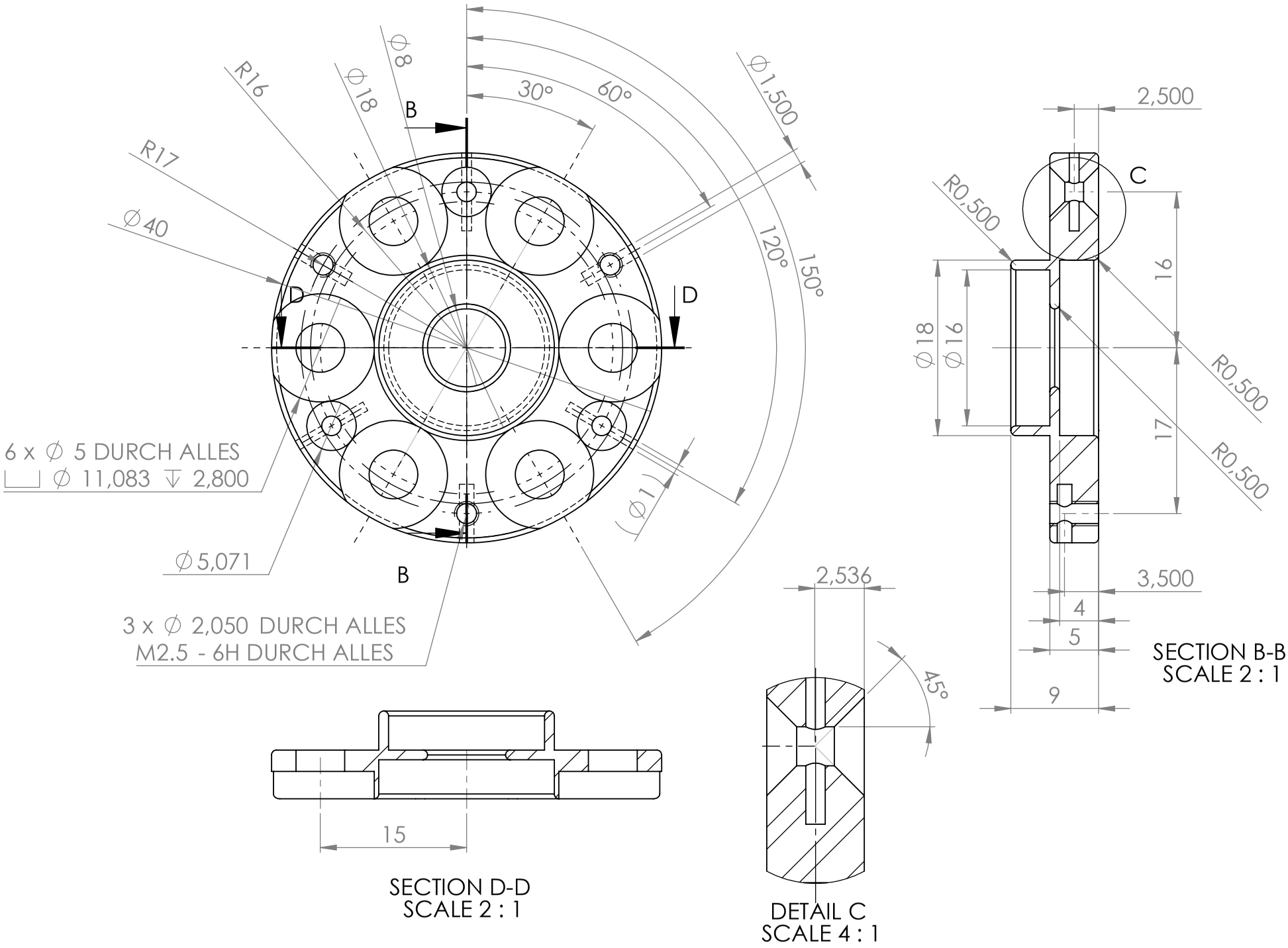
R16
⌀18
⌀8
30°
60°
⌀1,500
R17
⌀40
120°
150°
B
D
D
6 x ⌀ 5 DURCH ALLES
⌴ ⌀ 11,083 ↧ 2,800
⌀5,071
(⌀1)
B
3 x ⌀ 2,050 DURCH ALLES
M2.5 - 6H DURCH ALLES
2,500
C
R0,500
⌀18
⌀16
16
R0,500
17
R0,500
3,500
4
5
9
SECTION B-B
SCALE 2 : 1
15
SECTION D-D
SCALE 2 : 1
2,536
45°
DETAIL C
SCALE 4 : 1

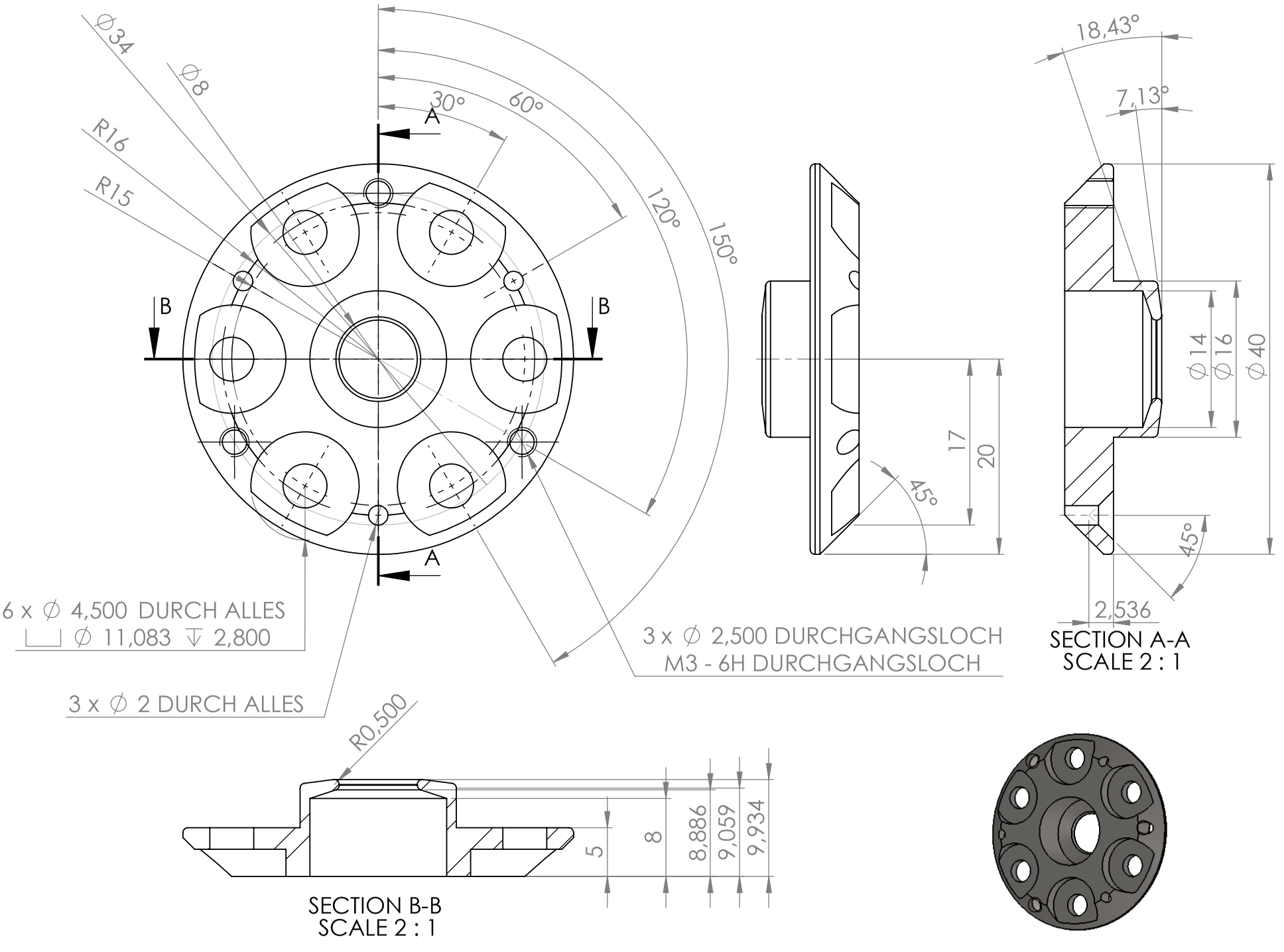
⌀34
⌀8
R16
R15
30°
60°
120°
150°
A
A
B
B
6 x ⌀ 4,500 DURCH ALLES
⌴ ⌀ 11,083 ↧ 2,800
3 x ⌀ 2 DURCH ALLES
3 x ⌀ 2,500 DURCHGANGSLOCH
M3 - 6H DURCHGANGSLOCH
17
20
45°
18,43°
7,13°
⌀14
⌀16
⌀40
45°
2,536
SECTION A-A
SCALE 2 : 1
R0,500
5
8
8,886
9,059
9,934
SECTION B-B
SCALE 2 : 1

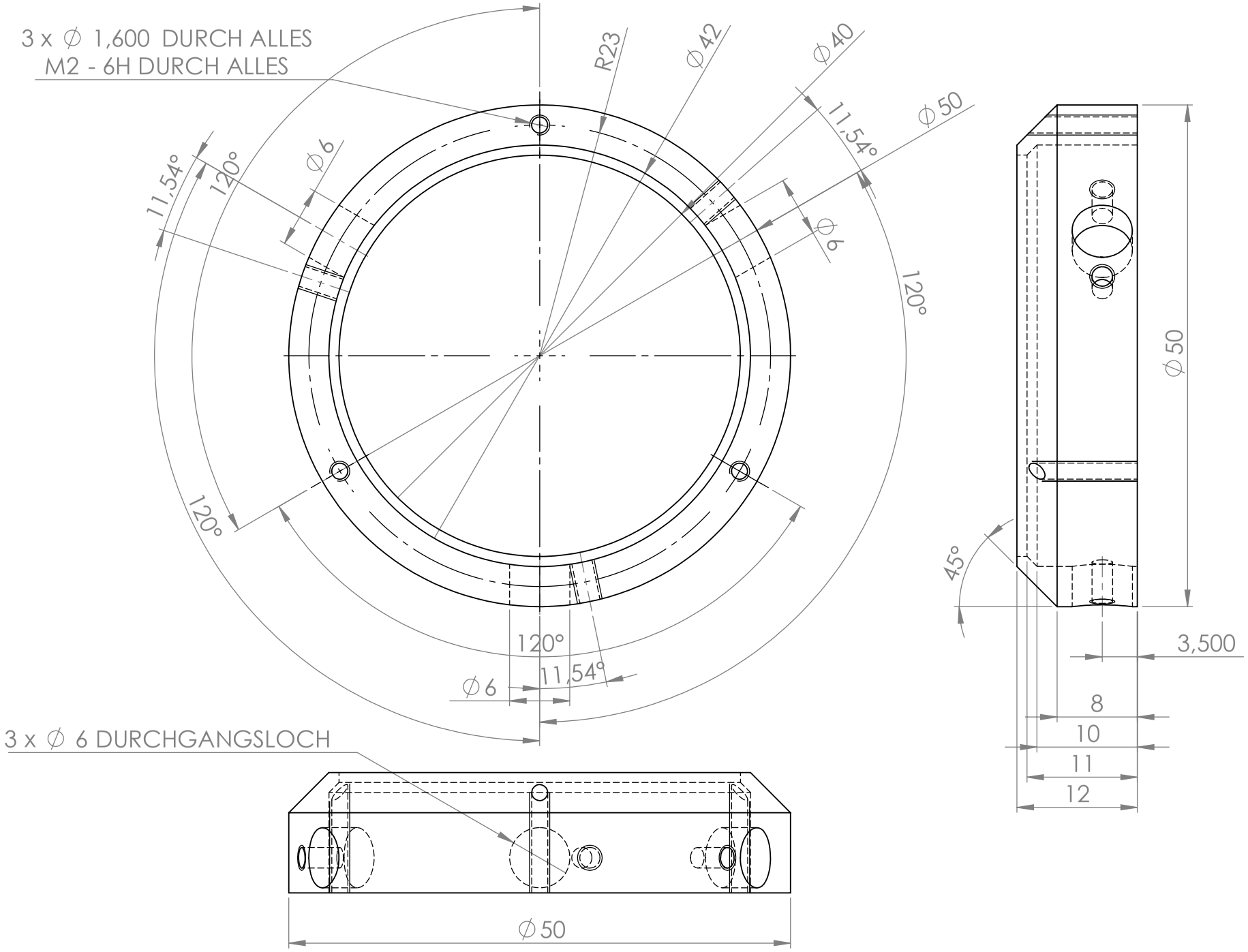
3 x ∅ 1,600 DURCH ALLES
M2 - 6H DURCH ALLES
R23
∅42
∅40
11,54°
∅50
∅6
120°
11,54°
120°
∅6
120°
120°
11,54°
∅6
∅50
45°
3,500
8
10
11
12
3 x ∅ 6 DURCHGANGSLOCH
∅50

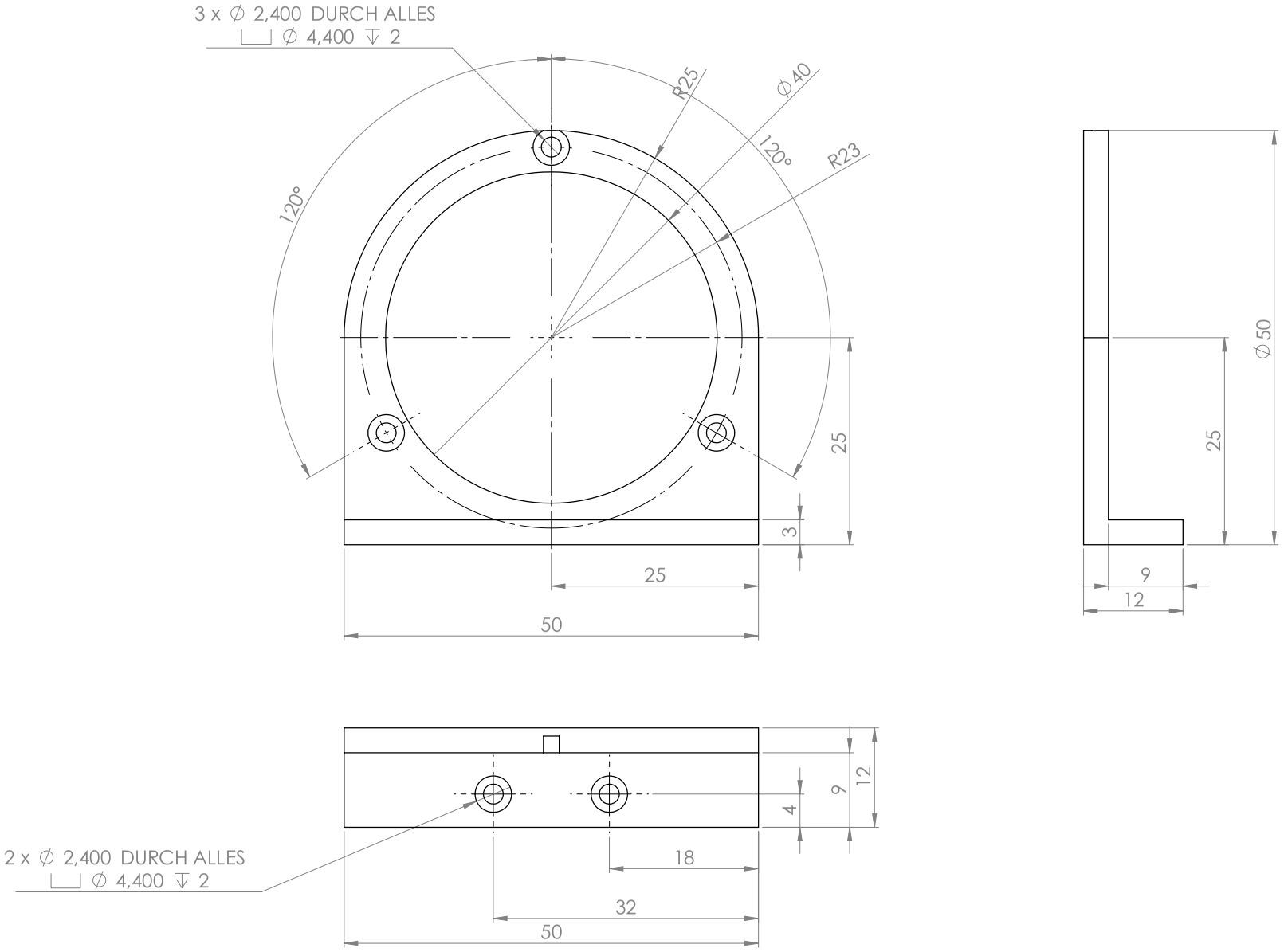
3 x ∅ 2,400 DURCH ALLES
⌴ ∅ 4,400 ↧ 2
R25
∅40
120°
R23
120°
25
3
25
50
∅50
25
9
12
2 x ∅ 2,400 DURCH ALLES
⌴ ∅ 4,400 ↧ 2
4
9
12
18
32
50

C. Scientific publications

Publications related to this thesis:

Transmission Microscopy with Nanometer Resolution Using a Deterministic Single Ion Source,
G. Jacob, K. Groot-Berning, S. Wolf, S. Ulm, L. Couturier, S. T. Dawkins, U. G. Poschinger, F. Schmidt-Kaler, and K. Singer,
Physical Review Letters **117**, 043001 (2016),
featured in *Physics*.

Maximizing the information gain of a single ion microscope using bayes experimental design
G. Jacob, K. Groot-Berning, U. G. Poschinger, F. Schmidt-Kaler, and K. Singer,
SPIE Proceedings 9900, Quantum Optics (2016).

Mikroskopieren mit einzelnen Ionen
G. Jacob, K. Groot-Berning, S. Wolf, S. T. Dawkins, U. G. Poschinger, F. Schmidt-Kaler und K. Singer,
Accepted for publication in GIT Labor-Fachzeitschrift.

Publications not directly related to the topic of this thesis:

Observation of the Kibble-Zurek scaling law for defect formation in ion crystals,
S. Ulm, J. Roßnagel, G. Jacob, C. Degünther, S. T. Dawkins, U. G. Poschinger, R. Nigmatullin, A. Retzker, M. B. Plenio, F. Schmidt-Kaler, and K. Singer,
Nature Communications **4**, 2290 (2013).

Precise experimental investigation of eigenmodes in a planar ion crystal,
H. Kaufmann, S. Ulm, G. Jacob, U. G. Poschinger, H. Landa, A. Retzker, M.B. Plenio, and F. Schmidt-Kaler,
Physical Review Letters **109**, 263003 (2012).

Single-Ion Heat Engine at Maximum Power,
O. Abah, J. Roßnagel, G. Jacob, S. Deffner, F. Schmidt-Kaler, K. Singer, and E. Lutz,
Physical Review Letters **109**, 203006 (2012).

Focusing a deterministic single-ion beam,
W. Schnitzler, G. Jacob, R. Fickler, F. Schmidt-Kaler, and K. Singer
New Journal of Physics, **12**, 065023 (2010).

Bibliography

[Abb73] E. Abbe, *Beiträge zur Theorie des Mikroskops und der mikroskopischen Wahrnehmung*, Arch. Mikrosk. Anat. **9**, 413 (1873).

[Arn12] M. Arndt, A. Ekers, W. von Klitzing, and H. Ulbricht, *Focus on modern frontiers of matter wave optics and interferometry*, New J. Phys. **14**, 125006 (2012).

[Ate13] C. Ates, I. Lesanovsky, C. S. Adams, and K. J. Weatherill, *Fast and Quasideterministic Single Ion Source from a Dipole-Blockaded Atomic Ensemble*, Phys. Rev. Lett. **110**, 213003 (2013).

[Bai06] X. Baillard, A. Gauguet, S. Bize, P. Lemonde, P. Laurent, A. Clairon, and P. Rosenbusch, *Interference-filter-stabilized external-cavity diode lasers*, Opt. Commun. **266**, 609 (2006).

[Bas14] N. Bassim, K. Scott, and L. A. Giannuzzi, *Recent advances in focused ion beam technology and applications*, MRS Bull. **39**, 317 (2014).

[Ber98] D. Berkeland, J. Miller, J. Bergquist, W. Itano, and D. Wineland, *Minimization of ion micromotion in a Paul trap*, J. Appl. Phys. **83**, 5025 (1998).

[Bla08] R. Blatt and D. Wineland, *Entangled states of trapped atomic ions*, Nature **453**, 1008 (2008).

[Bra12] S. Brakhane, W. Alt, T. Kampschulte, M. Martinez-Dorantes, R. Reimann, S. Yoon, A. Widera, and D. Meschede, *Bayesian feedback control of a two-atom spin-state in an atom-cavity system*, Phys. Rev. Lett. **109**, 173601 (2012).

[Bro15] M. Brownnutt, M. Kumph, P. Rabl, and R. Blatt, *Ion-trap measurements of electric-field noise near surfaces*, Rev. Mod. Phys. **87**, 1419 (2015).

[Cet07] M. Cetina, A. Grier, J. Campbell, I. Chuang, and V. Vuletić, *Bright source of cold ions for surface-electrode traps*, Phys. Rev. A **76**, 041401 (2007).

[Cir92] J. I. Cirac, R. Blatt, P. Zoller, and W. D. Phillips, *Laser cooling of trapped ions in a standing wave*, Phys. Rev. A **46**, 2668 (1992).

[Cir94] J. I. Cirac, L. J. Garay, R. Blatt, A. S. Parkins, and P. Zoller, *Laser cooling of trapped ions: The influence of micromotion*, Phys. Rev. A **49**, 421 (1994).

[Cla07] B. J. Claessens, M. P. Reijnders, G. Taban, O. J. Luiten, and E. J. D. Vredenbregt, *Cold electron and ion beams generated from trapped atoms*, Phys. Plasmas **14** (2007).

[Deg13] C. Degünther, *Untersuchung struktureller Defekte in Ionenkristallen*, Diplomarbeit, Johannes Gutenberg-Universität Mainz (2013).

[Dem09] W. Demtröder, *Experimentalphysik 2*, Springer-Lehrbuch, Springer Berlin Heidelberg, 2009, 5th ed.

[Dol13] F. Dolde, I. Jakobi, B. Naydenov, N. Zhao, S. Pezzagna, C. Trautmann, J. Meijer, P. Neumann, F. Jelezko, and J. Wrachtrup, *Room-temperature entanglement between single defect spins in diamond*, Nat. Phys. **9**, 139 (2013).

[Don10] J. A. V. Donkelaar, A. D. Greentree, A. D. C. Alves, L. M. Jong, L. C. L. Hollenberg, and D. N. Jamieson, *Top-down pathways to devices with few and single atoms placed to high precision*, New J. Phys. **12**, 065016 (2010).

[Dre83] R. W. P. Drever, J. L. Hall, F. V. Kowalski, J. Hough, G. M. Ford, A. J. Munley, and H. Ward, *Laser Phase and Frequency Stabilization Using an Optical Resonator*, Appl. Phys. B **31**, 97 (1983).

[Dud98] T. Duden and E. Bauer, *Spin-polarized low energy electron microscopy*, Surf. Rev. Lett **5**, 1213 (1998).

[Ege05] R. F. Egerton, *Physical principles of electron microscopy: an introduction to TEM, SEM, and AEM*, Springer, 2005.

[Eng13] W. Engelen, M. van der Heijden, D. Bakker, E. Vredenbregt, and O. Luiten, *High-coherence electron bunches produced by femtosecond photoionization*, Nat. Commun. **4**, 1693 (2013).

[Ern09] R. Erni, M. D. Rossell, C. Kisielowski, and U. Dahmen, *Atomic-Resolution Imaging with a Sub-50-pm Electron Probe*, Phys. Rev. Lett. **102**, 096101 (2009).

[Esc75] W. H. Escovitz, T. R. Fox, and R. Levi-Setti, *Scanning Transmission Ion Microscope with a Field Ion Source*, Proc. Natl. Acad. Sci. **72**, 1826 (1975).

[Fel15] T. Feldker, P. Bachor, M. Stappel, D. Kolbe, R. Gerritsma, J. Walz, and F. Schmidt-Kaler, *Rydberg Excitation of a Single Trapped Ion*, Phys. Rev. Lett. **115**, 173001 (2015).

[Fic09] R. Fickler, W. Schnitzler, N. M. Linke, F. Schmidt-Kaler, and K. Singer, *Optimized focusing ion optics for an ultracold deterministic single ion source targeting nm resolution*, J. Mod. Opt. **56**, 2061 (2009).

[Fox03] R. W. Fox, C. W. Oates, and L. W. Hollberg, *Stabilizing diode lasers to high-finesse cavities*, Experimental methods in the physical sciences **40**, 1 (2003).

[Fue12] M. Fuechsle, J. A. Miwa, S. Mahapatra, H. Ryu, S. Lee, O. Warschkow, L. C. Hollenberg, G. Klimeck, and M. Y. Simmons, *A single-atom transistor*, Nat. Nanotechnol. **7**, 242 (2012).

[Gil07] M. Gilowski, C. Schubert, M. Zaiser, W. Herr, T. Wübbena, T. Wendrich, T. Müller, E. Rasel, and W. Ertmer, *Narrow bandwidth interference filter-stabilized diode laser systems for the manipulation of neutral atoms*, Opt. Commun. **280**, 443 (2007).

[Gue07] C. Guerlin, J. Bernu, S. Deleglise, C. Sayrin, S. Gleyzes, S. Kuhr, M. Brune, J.-M. Raimond, and S. Haroche, *Progressive field-state collapse and quantum non-demolition photon counting*, Nature **448**, 889 (2007).

[Han08] J. L. Hanssen, S. B. Hill, J. Orloff, and J. J. McClelland, *Magneto-Optical-Trap-Based, High Brightness Ion Source for Use as a Nanoscale Probe*, Nano Lett. **8**, 2844 (2008), pMID: 18715041.

[Har13] S. Haroche, *Nobel Lecture: Controlling photons in a box and exploring the quantum to classical boundary**, Rev. Mod. Phys. **85**, 1083 (2013).

[Has10] F. Hasselbach, *Progress in electron-and ion-interferometry*, Rep. Prog. Phys. **73**, 016101 (2010).

[Hed00] D. W. O. Heddle, *Electrostatic lens systems*, 2nd edition, CRC Press, 2000.

[Hel15] S. W. Hell, *Nobel Lecture: Nanoscopy with freely propagating light**, Rev. Mod. Phys. **87**, 1169 (2015).

[Hen10] F. Henkel, M. Krug, J. Hofmann, W. Rosenfeld, M. Weber, and H. Weinfurter, *Highly Efficient State-Selective Submicrosecond Photoionization Detection of Single Atoms*, Phys. Rev. Lett. **105**, 253001 (2010).

[Het15] M. Hettrich, T. Ruster, H. Kaufmann, C. F. Roos, C. T. Schmiegelow, F. Schmidt-Kaler, and U. G. Poschinger, *Measurement of Dipole Matrix Elements with a Single Trapped Ion*, Phys. Rev. Lett. **115**, 143003 (2015).

[Hil03a] S. B. Hill and J. J. McClelland, *Atoms on demand: Fast, deterministic production of single Cr atoms*, Appl. Phys. Lett. **82**, 3128 (2003).

[Hil03b] S. B. Hill and J. J. McClelland, *Performance of a feedback-controlled, deterministic source of single chromium atoms*, J. Opt. Soc. Am. B: Opt. Phys. **21**, 473 (2003).

[Hil14] L. Hilico, J.-P. Karr, A. Douillet, P. Indelicato, S. Wolf, and F. S. Kaler, *Cooling antihydrogen ions for the free-fall experiment GBAR*, arXiv preprint arXiv:1402.1695 (2014).

[Hom06] P. Hommelhoff, C. Kealhofer, and M. A. Kasevich, *Ultrafast Electron Pulses from a Tungsten Tip Triggered by Low-Power Femtosecond Laser Pulses*, Phys. Rev. Lett. **97**, 247402 (2006).

[Hop08] T. Hopf, C. Yang, S. M. Hearne, D. N. Jamieson, E. Gauja, S. E. Andresen, and A. S. Dzurak, *Low-Noise Detection System for the Counted Implantation of Single Ions in Silicon*, IEEE Trans. Nucl. Sci. **55**, 812 (2008).

[Hän75] T. Hänsch and A. Schawlow, *Cooling of gases by laser radiation*, Opt. Commun. **13**, 68 (1975).

[Iba11] Y. Ibaraki, U. Tanaka, and S. Urabe, *Detection of parametric resonance of trapped ions for micromotion compensation*, Appl. Phys. B **105**, 219 (2011).

[Ihe01] H. Ihee, V. A. Lobastov, U. M. Gomez, B. M. Goodson, R. Srinivasan, C.-Y. Ruan, and A. H. Zewail, *Direct imaging of transient molecular structures with ultrafast diffraction*, Science **291**, 458 (2001).

[Ind14] P. Indelicato, G. Chardin, P. Grandemange, D. Lunney, V. Manea, A. Badertscher, P. Crivelli, A. Curioni, A. Marchionni, B. Rossi, A. Rubbia, V. Nesvizhevsky, D. Brook-Roberge, P. Comini, P. Debu, P. Dupré, L. Liszkay, B. Mansoulié, P. Pérez, J.-M. Rey, B. Reymond, N. Ruiz, Y. Sacquin, B. Vallage, F. Biraben, P. Cladé, A. Douillet, G. Dufour, S. Guellati, L. Hilico, A. Lambrecht, R. Guérout, J.-P. Karr, F. Nez, S. Reynaud, I. C. Szabo, V.-Q. Tran, J. Trapateau, A. Mohri, Y. Yamazaki, M. Charlton, S. Eriksson, N. Madsen, D. van der Werf, N. Kuroda, H. Torii, Y. Nagashima, F. Schmidt-Kaler, J. Walz, S. Wolf, P.-A. Hervieux, G. Manfredi, A. Voronin, P. Froelich, S. Wronka, and M. Staszczak, *The Gbar project, or how does antimatter fall?*, Hyperfine Interact. **228**, 141 (2014).

[Jam16] D. N. Jamieson, W. I. Lawrie, S. G. Robson, A. M. Jakob, B. C. Johnson, and J. C. McCallum, *Deterministic doping*, Mater. Sci. Semicond. Process. – (2016).

[Joy11] D. C. Joy, *Scanning He+ Ion Beam Microscopy and Metrology*, in: *FRONTIERS OF CHARACTERIZATION AND METROLOGY FOR NANOELECTRONICS: 2011*, vol. 1395, 80–84, AIP Publishing, 2011.

[Kan98] B. E. Kane, *A silicon-based nuclear spin quantum computer*, Nature **393**, 133 (1998).

[Kau16] H. Kaufmann, T. Ruster, C. T. Schmiegelow, M. A. Luda, V. Kaushal, J. Schulz, D. von Lindenfels, F. Schmidt-Kaler, and U. G. Poschinger, *Fast ion swapping for quantum information processing*, arXiv preprint arXiv:1607.03734 (2016).

[Keh11] A. Kehlberger, *Entwicklung und Aufbau einer neuartigen Ionenfalle*, Diplomarbeit, Johannes Gutenberg-Universität Mainz (2011).

[Ket02] W. Ketterle, *Nobel lecture: When atoms behave as waves: Bose-Einstein condensation and the atom laser*, Rev. Mod. Phys. **74**, 1131 (2002).

[Kie00] D. Kielpinski, B. E. King, C. J. Myatt, C. A. Sackett, Q. A. Turchette, W. M. Itano, C. Monroe, D. J. Wineland, and W. H. Zurek, *Sympathetic cooling of trapped ions for quantum logic*, Phys. Rev. A **61**, 032310 (2000).

[Kim10] Y.-M. Kim, H. Y. Jeong, S.-H. Hong, S.-Y. Chung, J. Y. Lee, and Y.-J. Kim, *Practical Approaches to Mitigation of Specimen Charging in High-Resolution Transmission Electron Microscopy*, J. Vac. Sci. Technol., B **1**, 134 (2010).

[Kno32] M. Knoll and E. Ruska, *Das elektronenmikroskop*, Z. Phys. **78**, 318 (1932).

[Knu11] B. Knuffman, A. V. Steele, J. Orloff, and J. J. McClelland, *Nanoscale focused ion beam from laser-cooled lithium atoms*, New J. Phys. **13**, 103035 (2011).

[Knü12] S. Knünz, M. Herrmann, V. Batteiger, G. Saathoff, T. Hänsch, and T. Udem, *Sub-millikelvin spatial thermometry of a single Doppler-cooled ion in a Paul trap*, Phys. Rev. A **85**, 023427 (2012).

[Knu13] B. Knuffman, A. V. Steele, and J. J. McClelland, *Cold atomic beam ion source for focused ion beam applications*, J. Appl. Phys. **114** (2013).

[Koe11] P. M. Koenraad and M. E. Flatté, *Single dopants in semiconductors*, Nat. Mater. **10**, 91 (2011).

[Kol12] R. Kolesov, K. Xia, R. Reuter, R. Stöhr, A. Zappe, J. Meijer, P. Hemmer, and J. Wrachtrup, *Optical detection of a single rare-earth ion in a crystal*, Nat. Commun. **3**, 1029 (2012).

[Kot15] J. Kotakoski, C. Brand, Y. Lilach, O. Cheshnovsky, C. Mangler, M. Arndt, and J. C. Meyer, *Toward two-dimensional all-carbon heterostructures via ion beam patterning of single-layer graphene*, Nano Lett. **15**, 5944 (2015).

[Kre05] A. Kreuter, C. Becher, G. P. T. Lancaster, A. B. Mundt, C. Russo, H. Häffner, C. Roos, W. Hänsel, F. Schmidt-Kaler, R. Blatt, and M. S. Safronova, *Experimental and theoretical study of the* $3d\ ^2D$*–level lifetimes of* $^{40}\mathrm{Ca}^+$, Phys. Rev. A **71**, 032504 (2005).

[Kru00] D. Kruger, P. Schneck, and H. Gelderblom, *Helmut Ruska and the visualisation of viruses*, Lancet **355**, 1713 (2000).

[Kuy16] F. Kuypers, *Klassische Mechanik*, John Wiley & Sons, 2016.

[Lar86] D. J. Larson, J. C. Bergquist, J. J. Bollinger, W. M. Itano, and D. J. Wineland, *Sympathetic Cooling of Trapped Ions: A Laser-Cooled Two-Species Nonneutral Ion Plasma*, Phys. Rev. Lett. **57**, 70 (1986).

[Lei03] D. Leibfried, R. Blatt, C. Monroe, and D. J. Wineland, *Quantum dynamics of single trapped ions*, Rev. Mod. Phys. **75**, 281 (2003).

[Lin56] D. V. Lindley, *On a measure of the information provided by an experiment*, Ann. Math. Stat. 986–1005 (1956).

[Lob05] V. A. Lobastov, R. Srinivasan, and A. H. Zewail, *Four-dimensional ultrafast electron microscopy*, Proc. Natl. Acad. Sci. USA **102**, 7069 (2005).

[Lud15] A. D. Ludlow, M. M. Boyd, J. Ye, E. Peik, and P. O. Schmidt, *Optical atomic clocks*, Rev. Mod. Phys. **87**, 637 (2015).

[Mac59] W. W. Macalpine and R. O. Schildknecht, *Coaxial Resonators with Helical Inner Conductor*, Proc. of the IEEE **47**, 2099 (1959).

[Mai06] R. Maiwald, *Abbildungs- und Steuerungssystem für ein Experiment mit einzelnen Ionen*, Diplomarbeit, Universität Ulm (2006).

[McC11] A. McCulloch, D. Sheludko, S. Saliba, S. Bell, M. Junker, K. Nugent, and R. Scholten, *Arbitrarily shaped high-coherence electron bunches from cold atoms*, Nat. Phys. **7**, 785 (2011).

[McC16] J. J. McClelland, A. V. Steele, B. Knuffman, K. A. Twedt, A. Schwarzkopf, and T. M. Wilson, *Bright focused ion beam sources based on laser-cooled atoms*, Appl. Phys. Rev. **3** (2016).

[Mei06] J. Meijer, T. Vogel, B. Burchard, I. W. Rangelow, L. Bischoff, J. Wrachtrup, M. Domhan, F. Jelezko, W. Schnitzler, S. A. Schulz, K. Singer, and F. Schmidt-Kaler, *Concept of deterministic single ion doping with sub-nm spatial resolution*, Appl. Phys. A **83**, 321 (2006).

[Mit05] M. Mitic, S. E. Andresen, C. Yang, T. Hopf, V. Chan, E. Gauja, F. E. Hudson, T. M. Buehler, R. Brenner, A. J. Ferguson, C. I. Pakes, S. M. Hearne, G. Tamanyan, D. J. Reilly, A. R. Hamilton, D. N. Jamieson, A. S. Dzurak, and R. G. Clark, *Single atom Si nanoelectronics using controlled single-ion implantation*, Microelectron. Eng. **78-79**, 279 (2005).

[Moo09] J. H. Moore, C. C. Davis, M. A. Coplan, and S. C. Greer, *Building scientific apparatus*, Cambridge University Press, 2009.

[Mül36] E. W. Müller, *Versuche zur Theorie der Elektronenemission unter der Einwirkung hoher Feldstärke*, Phys. Z. **37**, 838 (1936).

[Mül51] E. W. Müller, *Das Feldionenmikroskop*, Z. Phys. **131**, 136 (1951).

[Mül56] E. W. Müller and K. Bahadur, *Field Ionization of Gases at a Metal Surface and the Resolution of the Field Ion Microscope*, Phys. Rev. **102**, 624 (1956).

[Mül16] M. Müller, V. Kravtsov, A. Paarmann, M. B. Raschke, and R. Ernstorfer, *Nanofocused Plasmon-Driven Sub-10 fs Electron Point Source*, ACS Photonics **3**, 611 (2016).

[Mur14] D. Murphy, R. Speirs, D. Sheludko, C. Putkunz, A. McCulloch, B. Sparkes, and R. Scholten, *Detailed observation of space–charge dynamics using ultracold ion bunches*, Nat. Commun. **5** (2014).

[Mur15] D. Murphy, R. E. Scholten, and B. M. Sparkes, *Increasing the Brightness of Cold Ion Beams by Suppressing Disorder-Induced Heating with Rydberg Blockade*, Phys. Rev. Lett. **115**, 214802 (2015).

[Mye08] A. H. Myerson, D. J. Szwer, S. C. Webster, D. T. C. Allcock, M. J. Curtis, G. Imreh, J. A. Sherman, D. N. Stacey, A. M. Steane, and D. M. Lucas, *High-Fidelity Readout of Trapped-Ion Qubits*, Phys. Rev. Lett. **100**, 200502 (2008).

[Neu78] W. Neuhauser, M. Hohenstatt, P. Toschek, and H. Dehmelt, *Optical-Sideband Cooling of Visible Atom Cloud Confined in Parabolic Well*, Phys. Rev. Lett. **41**, 233 (1978).

[Neu10] P. Neumann, R. Kolesov, B. Naydenov, J. Beck, F. Rempp, M. Steiner, V. Jacques, G. Balasubramanian, M. Markham, D. Twitchen, et al., *Quantum register based on coupled electron spins in a room-temperature solid*, Nat. Phys. **6**, 249 (2010).

[Orl75] J. H. Orloff, *Study of a field-ionization source for microprobe applications*, J. Vac. Sci. Technol. **12**, 1209 (1975).

[Ost13] C. Osterkamp, J. Scharpf, S. Pezzagna, J. Meijer, T. Diemant, R. J. Behm, B. Naydenov, and F. Jelezko, *Increasing the creation yield of shallow single defects in diamond by surface plasma treatment*, Appl. Phys. Lett. **103**, 193118 (2013).

[Pau53] W. Paul and H. Steinwedel, *Notizen: Ein neues Massenspektrometer ohne Magnetfeld*, Z. Naturforsch., A **8**, 448 (1953).

[Pau58] W. Paul, O. Osberghaus, and E. Fischer, *Ein Ionenkäfig*, Forschungsberichte des Wirtschafts- und Verkehrsministeriums Nordrhein-Westfalen **415** (1958).

[Pau90] W. Paul, *Electromagnetic traps for charged and neutral particles*, Rev. Mod. Phys. **62**, 531 (1990).

[Per04a] A. Persaud, F. I. Allen, F. Gicquel, S. J. Park, J. A. Liddle, T. Schenkel, T. Ivanov, K. Ivanova, I. W. Rangelow, and J. Bokor, *Single ion implantation with scanning probe alignment*, J. Vac. Sci. Technol., B **22**, 2992 (2004).

[Per04b] A. Persaud, S. J. Park, J. A. Liddle, I. W. Rangelow, J. Bokor, R. Keller, F. I. Allen, D. H. Schneider, and T. Schenkel, *Quantum Computer Development with Single Ion Implantation*, Quantum Inf. Process. **3**, 233 (2004).

[Pez07] L. Pezzé, A. Smerzi, G. Khoury, J. F. Hodelin, and D. Bouwmeester, *Phase Detection at the Quantum Limit with Multiphoton Mach-Zehnder Interferometry*, Phys. Rev. Lett. **99**, 223602 (2007).

[Pez10] S. Pezzagna, B. Naydenov, F. Jelezko, J. Wrachtrup, and J. Meijer, *Creation efficiency of nitrogen-vacancy centres in diamond*, New J. Phys. **12**, 065017 (2010).

[Pla12] J. J. Pla, K. Y. Tan, J. P. Dehollain, W. H. Lim, J. J. Morton, D. N. Jamieson, A. S. Dzurak, and A. Morello, *A single-atom electron spin qubit in silicon*, Nature **489**, 541 (2012).

[Pra95] S. Prawer and R. Kalish, *Ion-beam-induced transformation of diamond*, Phys. Rev. B **51**, 15711 (1995).

[Rei09] M. P. Reijnders, P. A. van Kruisbergen, G. Taban, S. B. van der Geer, P. H. A. Mutsaers, E. J. D. Vredenbregt, and O. J. Luiten, *Low-Energy-Spread Ion Bunches from a Trapped Atomic Gas*, Phys. Rev. Lett. **102**, 034802 (2009).

[Rei10] M. P. Reijnders, N. Debernardi, S. B. van der Geer, P. H. A. Mutsaers, E. J. D. Vredenbregt, and O. J. Luiten, *Phase-Space Manipulation of Ultracold Ion Bunches with Time-Dependent Fields*, Phys. Rev. Lett. **105**, 034802 (2010).

[RM12] J. Riedrich-Möller, L. Kipfstuhl, C. Hepp, E. Neu, C. Pauly, F. Mücklich, A. Baur, M. Wandt, S. Wolff, M. Fischer, S. Gsell, M. Schreck, and C. Becher, *One-and two-dimensional photonic crystal microcavities in single crystal diamond*, Nat. Nanotechnol. **7**, 69 (2012).

[Roo00] C. F. Roos, *Controlling the quantum state of trapped ions*, Dissertation, Universität Innsbruck (2000).

[Rop07] C. Ropers, D. R. Solli, C. P. Schulz, C. Lienau, and T. Elsaesser, *Localized Multiphoton Emission of Femtosecond Electron Pulses from Metal Nanotips*, Phys. Rev. Lett. **98**, 043907 (2007).

[Ros08] T. Rosenband, D. Hume, P. Schmidt, C. Chou, A. Brusch, L. Lorini, W. Oskay, R. Drullinger, T. Fortier, J. Stalnaker, et al., *Frequency ratio of Al+ and Hg+ single-ion optical clocks; metrology at the 17th decimal place*, Science **319**, 1808 (2008).

[Sag12] J. M. Sage, A. J. Kerman, and J. Chiaverini, *Loading of a surface-electrode ion trap from a remote, precooled source*, Phys. Rev. A **86**, 013417 (2012).

[San99] G. Santarelli, P. Laurent, P. Lemonde, A. Clairon, A. G. Mann, S. Chang, A. N. Luiten, and C. Salomon, *Quantum Projection Noise in an Atomic Fountain: A High Stability Cesium Frequency Standard*, Phys. Rev. Lett. **82**, 4619 (1999).

[Sch36] O. Scherzer, *über einige Fehler von Elektronenlinsen*, Z. Phys. A: Hadrons Nucl. **101**, 593 (1936).

[Sch02] G. Schönhense and H. Spiecker, *Correction of chromatic and spherical aberration in electron microscopy utilizing the time structure of pulsed excitation sources*, J. Vac. Sci. Technol., B **20**, 2526 (2002).

[Sch09a] W. Schnitzler, N. M. Linke, R. Fickler, J. Meijer, F. Schmidt-Kaler, and K. Singer, *Deterministic Ultracold Ion Source Targeting the Heisenberg Limit*, Phys. Rev. Lett. **102**, 070501 (2009).

[Sch09b] S. A. Schulz, *Scalable Microchip Ion Traps for Quantum Computation*, Dissertation, Universität Ulm (2009).

[Sch10a] W. Schnitzler, *Deterministic ultracold ion source targeting the Heisenberg limit*, Dissertation, Universität Ulm (2010).

[Sch10b] W. Schnitzler, G. Jacob, R. Fickler, F. Schmidt-Kaler, and K. Singer, *Focusing a deterministic single-ion beam*, New J. Phys. **12**, 065023 (2010).

[Sch11] W. P. Schleich, *Quantum optics in phase space*, John Wiley & Sons, 2011.

[She07] L. Shen and Y. J. Liu, *An adaptive fast multipole boundary element method for three-dimensional potential problems*, Comput. Mech. **39**, 681 (2007).

[Shi05] T. Shinada, S. Okamoto, T. Kobayashi, and I. Ohdomari, *Enhancing semiconductor device performance using ordered dopant arrays*, Nature **437**, 1128 (2005).

[Sin02] K. Singer, S. Jochim, M. Mudrich, A. Mosk, and M. Weidemüller, *Low-cost mechanical shutter for light beams*, Rev. Sci. Instrum. **73**, 4402 (2002).

[Sin10] K. Singer, U. Poschinger, M. Murphy, P. Ivanov, F. Ziesel, T. Calarco, and F. Schmidt-Kaler, *Colloquium: Trapped ions as quantum bits: Essential numerical tools*, Rev. Mod. Phys. **82**, 2609 (2010).

[Ste86] S. Stenholm, *The semiclassical theory of laser cooling*, Rev. Mod. Phys. **58**, 699 (1986).

[Ste10] A. V. Steele, B. Knuffman, J. J. McClelland, and J. Orloff, *Focused chromium ion beam*, J. Vac. Sci. Technol., B **28**, C6F1 (2010).

[Tab10] G. Taban, M. P. Reijnders, B. Fleskens, S. B. van der Geer, O. J. Luiten, and E. J. D. Vredenbregt, *Ultracold electron source for single-shot diffraction studies*, Europhys. Lett. **91**, 46004 (2010).

[Tre16] C. Tresp, C. Zimmer, I. Mirgorodskiy, H. Gorniaczyk, A. Paris-Mandoki, and S. Hofferberth, *Single-photon absorber based on strongly interacting Rydberg atoms*, arXiv preprint arXiv:1605.04456 (2016).

[Twe14] K. A. Twedt, L. Chen, and J. J. McClelland, *Scanning ion microscopy with low energy lithium ions*, Ultramicroscopy **142**, 24 (2014).

[Ulm13] S. Ulm, J. Roßnagel, G. Jacob, C. Degünther, S. Dawkins, U. Poschinger, R. Nigmatullin, A. Retzker, M. Plenio, F. Schmidt-Kaler, et al., *Observation of the Kibble–Zurek scaling law for defect formation in ion crystals*, Nat. Commun. **4** (2013).

[Vel15] M. Veldhorst, C. Yang, J. Hwang, W. Huang, J. Dehollain, J. Muhonen, S. Simmons, A. Laucht, F. Hudson, K. Itoh, A. Morello, and A. Dzurak, *A two-qubit logic gate in silicon*, Nature **526**, 410 (2015).

[VH10] A. Van Helden, S. Dupré, and R. van Gent, *The Origins of the Telescope*, Geschiedenis Van De Wetenschap in Nederland, KNAW Press, 2010.

[Vit16] M. Viteau, M. Reveillard, L. Kime, B. Rasser, P. Sudraud, Y. Bruneau, G. Khalili, P. Pillet, D. Comparat, I. Guerri, A. Fioretti, D. Ciampini, M. Allegrini, and F. Fuso, *Ion microscopy based on laser-cooled cesium atoms*, Ultramicroscopy **164**, 70 (2016).

[Wal12] A. Walther, F. Ziesel, T. Ruster, S. T. Dawkins, K. Ott, M. Hettrich, K. Singer, F. Schmidt-Kaler, and U. Poschinger, *Controlling Fast Transport of Cold Trapped Ions*, Phys. Rev. Lett. **109**, 080501 (2012).

[War06] B. Ward, J. A. Notte, and N. Economou, *Helium ion microscope: A new tool for nanoscale microscopy and metrology*, J. Vac. Sci. Technol., B **24**, 2871 (2006).

[Wei11] S. Weidlich, *Nachweis der Implantation einzelner Ionen in Festkörper*, Diplomarbeit, Johannes Gutenberg-Universität Mainz (2011).

[Wie15] H. Wiedemann, *Particle accelerator physics*, Springer, 2015.

[Wil97] J. C. Williamson, J. Cao, H. Ihee, H. Frey, and A. H. Zewail, *Clocking transient chemical changes by ultrafast electron diffraction*, Nature **386**, 159 (1997).

[Win75] D. J. Wineland and H. G. Dehmelt, *Proposed* $10^{14}\ \Delta\nu < \nu$ *Laser Fluorescence Spectroscopy on* Tl^{+} *Mono-Ion Oscillator III*, Bulletin of the American Physical Society **20**, 637 (1975).

[Win78] D. J. Wineland, R. E. Drullinger, and F. L. Walls, *Radiation-pressure cooling of bound resonant absorbers*, Phys. Rev. Lett. **40**, 1639 (1978).

[Win13] D. J. Wineland, *Nobel Lecture: Superposition, entanglement, and raising Schrödinger's cat**, Rev. Mod. Phys. **85**, 1103 (2013).

[Wol12] S. Wolf, *Verfahren zur deterministischen, hochauflösenden Implantation von Farbzentren*, Diplomarbeit, Johannes Gutenberg-Universität Mainz (2012).

[Wol16] S. Wolf, J. Wechs, J. von Zanthier, and F. Schmidt-Kaler, *Visibility of Young's Interference Fringes: Scattered Light from Small Ion Crystals*, Phys. Rev. Lett. **116**, 183002 (2016).

[Wüb12] J. B. Wübbena, S. Amairi, O. Mandel, and P. O. Schmidt, *Sympathetic cooling of mixed-species two-ion crystals for precision spectroscopy*, Phys. Rev. A **85**, 043412 (2012).

[Zie12] F. Ziesel, *Quantum State Manipulation and Dynamics in Micro Ion Traps*, Dissertation, Universität Ulm (2012).

[Zor88] P. Zorabedian and W. Trutna, *Interference-filter-tuned, alignment-stabilized, semiconductor external-cavity laser*, Opt. Lett. **13**, 826 (1988).

Danksagung

Curriculum Vitae